

Structure Functions

Tony Doyle

Dept. of Physics and Astronomy
University of Glasgow, G12 8QQ, UK.
E-mail: A.Doyle@physics.gla.ac.uk

Diffraction and Low- Q^2 Physics Including Two-Photon Physics

Martin Erdmann

Universität Karlsruhe
Engesserstr. 7, D-76128 Karlsruhe
E-mail: Martin.Erdmann@desy.de

Structure Functions

Tony Doyle

Dept. of Physics and Astronomy, University of Glasgow, G12 8QQ, UK.
E-mail: A.Doyle@physics.gla.ac.uk

Abstract

The latest structure function results, as presented at the ICHEP98 conference, are reviewed. A brief introduction to the formalism and the status of global analyses of parton distributions is given. The review focuses on three experimental areas: fixed-target results and their constraints on the parton densities at high x ; spin structure and spin parton densities as well as the status of the associated sum rules; HERA results on the dynamics of F_2 at low (x, Q^2) , charm and F_L as well as the measurement and interpretation of the high- Q^2 neutral and charged current cross-sections.

1 Introduction - Formalism and Road Maps

The differential cross-section $l(k)N(p) \rightarrow l(k')X(p')$ for a lepton (e, μ) with four-momentum k scattering off a nucleon with four-momentum p can be expressed as

$$\frac{d^2\sigma(l^\pm N)}{dx dQ^2} = \frac{2\pi\alpha^2}{xQ^4} [Y_+ F_2(x, Q^2) \mp Y_- x F_3(x, Q^2) - y^2 F_L(x, Q^2)]$$

where Q^2 is the four-momentum transfer squared, $x = Q^2/2p \cdot q$ is the Bjorken scaling variable, $y = p \cdot q/p \cdot k$ is the inelasticity variable and $Y_\pm = 1 \pm (1 - y)^2$. The contribution from F_2 dominates the cross-section. The contribution from F_L is a QCD correction which is important only at large y and that from $x F_3$ is negligible for $Q^2 \ll M_Z^2$. To investigate sensitivity to F_L at large y or $x F_3$ at large Q^2 , the reduced cross-section $\tilde{\sigma} \equiv \frac{xQ^4}{2\pi\alpha^2} \frac{1}{Y_+} \frac{d^2\sigma}{dx dQ^2}$ is adopted. In the Quark Parton Model (or in the DIS scheme of NLO QCD) and for $Q^2 \ll M_Z^2$ F_2/x is the charge-weighted sum of the quark densities

$$F_2(x, Q^2) = x \sum_i e_i^2 \cdot \Sigma(x, Q^2)$$

where $\Sigma(x, Q^2) = \sum_i [q_i(x, Q^2) + \bar{q}_i(x, Q^2)]$ is the *singlet* summed quark and anti-quark distributions. Similarly, the charged current cross-section $e^+(e^-)N \rightarrow \nu(\bar{\nu})X$ at HERA can be expressed as

$$\frac{d^2\sigma^{CC}(l^\pm N)}{dx dQ^2} = \frac{G_F^2}{4\pi x} \left(\frac{M_W^2}{Q^2 + M_W^2} \right)^2 [Y_+ F_2^{CC}(x, Q^2) \mp Y_- x F_3^{CC}(x, Q^2)].$$

For fixed-target $\nu(\bar{\nu})N \rightarrow \mu^+(\mu^-)X$ experiments, $Q^2 \ll M_W^2$, and in the QPM

$$xF_3^{CC}(x, Q^2) = x \sum_i e_i^2 \cdot q_{NS}(x, Q^2)$$

where $q_{NS}(x, Q^2) = \sum_i [q_i(x, Q^2) - \bar{q}_i(x, Q^2)]$ is the *non-singlet* difference of these distributions.

In Fig. 1, the kinematic plane covered by the $F_2(x, Q^2)$ measurements is shown, including the new preliminary datasets from H1 and ZEUS which are seen to extend to: low y ($y_{\text{HERA}} \sim 0.005$) providing overlap with the fixed-target experiments; very low x ($x \lesssim 10^{-5}$) at low Q^2 exploring the transition region from soft to hard physics; high y ($y \rightarrow 0.82$) giving sensitivity to F_L ; high $x \rightarrow 0.65$ probing sensitivity to electroweak effects in F_2 and xF_3 as well as constraining the valence quarks at large Q^2 . The fixed-target experiments NMC, BCDMS, E665 and SLAC experiments have provided final measurements at higher x and lower Q^2 . New information was presented at ICHEP98 from CCFR, E866 and the Tevatron which also constrain the medium-high x partons.

Theoretically, the directions in (x, Q^2) can be mapped out according to the dominant dynamical effects, as illustrated in Fig. 2. Given a phenomenological input as a function of x , the parton distributions are evolved to different physical scales (Q^2) via the DGLAP evolution equations. The alternative BFKL approach is to attempt to calculate the x dependence directly from pQCD, where the running of the effective coupling constant is neglected to leading order. BFKL predicts an $x^{-\lambda}$ dependence of F_2 at small x . The BFKL equation has recently been calculated to NLO [1]. These corrections are numerically very large in the experimentally accessible low (x, Q^2) range, resulting in $\lambda_{LO} \sim 0.5$ being reduced to $\lambda_{NLO} \sim 0.1$. The understanding of the NLO corrections to the BFKL equation is therefore an active area of study [2]. In the DLLA ('double leading log approximation'), non-leading $\ln(Q^2) \ln(1/x)$ terms can also be evaluated, but a method which reliably maps the complete region of (x, Q^2) in terms of pQCD is still not known. The region of high parton density may be reached at very low x , where these approaches are not strictly valid. The expectation from the GLR equation [3] is that the region where the partons overlap is accessible at slightly higher x for decreasing Q^2 . However, Q^2 should also be sufficiently large that higher twist and non-perturbative effects parameterised in terms of Regge exchanges can be neglected.

In the DGLAP approach, the non-singlet contribution evolves as

$$\frac{\partial q_{NS}(x, Q^2)}{\partial t} = \frac{\alpha_s(Q^2)}{2\pi} P_{qq}^{NS} \otimes q_{NS}(x', Q^2)$$

where $t = \ln(Q^2/\Lambda^2)$ and the P_{ij} 's represent the NLO DGLAP splitting probabilities for radiating a parton with momentum fraction x from a parton with higher momentum x' . Quantities such as xF_3 provide a measure of $\alpha_s(Q^2)$ which is insensitive to the a priori unknown gluon distribution. Similarly, the singlet quark and gluon densities are coupled via

$$\frac{\partial}{\partial t} \begin{pmatrix} \Sigma(x, Q^2) \\ g(x, Q^2) \end{pmatrix} = \frac{\alpha_s(Q^2)}{2\pi} \begin{bmatrix} P_{qq} & P_{qg} \\ P_{gq} & P_{gg} \end{bmatrix} \otimes \begin{pmatrix} \Sigma(x', Q^2) \\ g(x', Q^2) \end{pmatrix}$$

and quantities such as F_2 provide input for $\Sigma(x, Q^2)$ as well as coupled knowledge of $\alpha_s(Q^2)$ and the gluon, $g(x, Q^2)$.

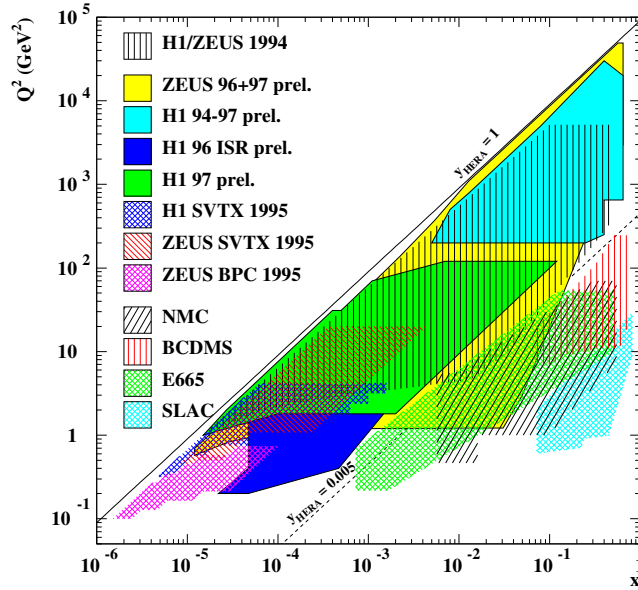


Figure 1: Measured regions of F_2 in the (x, Q^2) kinematic plane. The nominal acceptance region of the HERA measurements corresponds to $y_{\text{HERA}} > 0.005$. The fixed-target experimental data occupies the region of high x at low Q^2 .

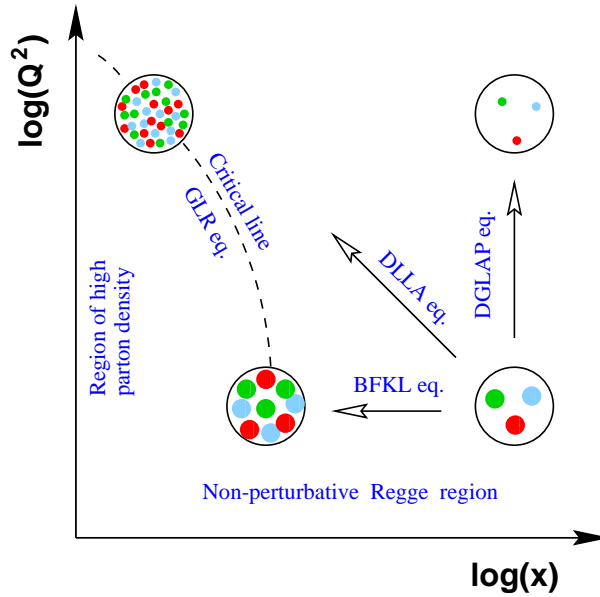


Figure 2: Schematic representation of parton densities and the theoretical evolution directions in the (x, Q^2) kinematic plane.

At the starting scale, Q_0^2 , the light valence quarks (q_v) and the sea of quark and anti-quarks (\bar{q}) as well as the gluon (g) are attributed a given functional form. For example in the MRST parameterisations

$$f_i(x, Q_0^2) = A_i x^{\delta_i} (1-x)^{\eta_i} (1 + \epsilon_i \sqrt{x} + \gamma_i x)$$

where some parameters are set to 0 or fixed by sum rules and differences of u and d quarks may additionally be constrained. The heavy quark (sea) contributions are calculated explicitly

at NLO and their uncertainty is typically determined by the range allowed for the effective mass of the heavy quark. The measured structure functions are then described by the convolutions of the light quark densities with the appropriate NLO matrix elements.

The outlined procedure defines the structure of a nucleon in terms of its constituent quarks and gluons. However, guided by the new datasets and analyses which were presented to this conference, it should be noted that the following assumptions are made:

- $\alpha_s(Q^2) \ln(Q^2)$ (DGLAP) terms are large compared to $\alpha_s(Q^2) \ln(1/x)$ (BFKL) terms in the perturbative splitting functions; ¹
- higher-twist (HT) contributions (suppressed by factors of $1/Q^2$) are negligibly small; ²
- Nuclear binding effects are treated as small corrections or ignored in analyses of deuteron data. ³

In Table 1, the experimental datasets considered in the MRST analysis are listed along with the underlying physics process and the parton behaviour which is being probed. The experiments denoted by † correspond to final measurements reported at ICHEP98. Those denoted by ★ correspond to new preliminary measurements reported at this conference. The latest global fits of MRST [6], GRV98 [7] and CTEQ4 [8] are used here to compare with the data.

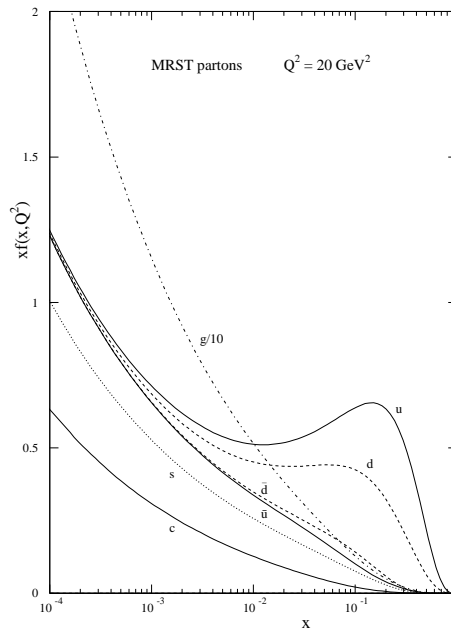


Figure 3: MRST parton distributions $x f(x, Q^2)$ at $Q^2 = 20 \text{ GeV}^2$.

¹ The study of inclusive quantities such as F_2 at small x are presently unable to distinguish these BFKL terms. The status of forward jet production searches which enhance sensitivity to these effects is reviewed by J. Huston [4].

² Progress in determining the size of these higher twist and other hadronisation power corrections via infra-red renormalons is reviewed by Y. Dokshitzer [5].

³ A discussion of diffractive final states in D.I.S including nuclear effects is included in the review by M. Erdmann.

Table 1: Processes studied in global parton distribution fits. \star indicates new preliminary data presented at ICHEP98, included in this review. \dagger indicates final data presented at ICHEP98. \ast indicates data used in the MRST fits. (Courtesy of A. Martin.)

Process/ Experiment	Leading order subprocess	Parton behaviour probed
DIS ($\mu N \rightarrow \mu X$) $F_2^{\mu p}, F_2^{\mu d}, F_2^{\mu n}/F_2^{\mu p}$ (SLAC, BCDMS, NMC, E665)*	$\gamma^* q \rightarrow q$	Four structure functions \rightarrow $u + \bar{u}$ $d + \bar{d}$ $\bar{u} + \bar{d}$ s (assumed = \bar{s}), but only $\int xg(x, Q_0^2)dx \simeq 0.35$ and $\int(\bar{d} - \bar{u})dx \simeq 0.1$
DIS ($\nu N \rightarrow \mu X$) $F_2^{\nu N}, xF_3^{\nu N}$ (CCFR)*	$W^* q \rightarrow q'$	
DIS (small x) F_2^{ep} (H1, ZEUS)*	$\gamma^*(Z^*)q \rightarrow q$	λ ($x\bar{q} \sim x^{-\lambda_s}, xg \sim x^{-\lambda_g}$)
DIS (F_L) NMC, HERA	$\gamma^* g \rightarrow q\bar{q}$	g
$\ell N \rightarrow c\bar{c}X$ F_2^c (EMC; H1, ZEUS)*	$\gamma^* c \rightarrow c$	c ($x \gtrsim 0.01; x \lesssim 0.01$)
$\nu N \rightarrow \mu^+ \mu^- X$ (CCFR)*	$W^* s \rightarrow c$ $\hookrightarrow \mu^+$	$s \approx \frac{1}{4}(\bar{u} + \bar{d})$
$pN \rightarrow \gamma X$ (WA70*, UA6, E706, ...)	$qg \rightarrow \gamma q$	g at $x \simeq 2p_T/\sqrt{s} \rightarrow$ $x \approx 0.2 - 0.6$
$pN \rightarrow \mu^+ \mu^- X$ (E605, E772)*	$q\bar{q} \rightarrow \gamma^*$	$\bar{q} = \dots(1-x)^{n_s}$
$pp, pn \rightarrow \mu^+ \mu^- X$ (E866, NA51)*	$u\bar{u}, d\bar{d} \rightarrow \gamma^*$ $u\bar{d}, d\bar{u} \rightarrow \gamma^*$	$\bar{u} - \bar{d}$ ($0.04 \lesssim x \lesssim 0.3$)
$ep, en \rightarrow e\pi X$ (HERMES)	$\gamma^* q \rightarrow q$ with $q = u, d, \bar{u}, \bar{d}$	$\bar{u} - \bar{d}$ ($0.04 \lesssim x \lesssim 0.2$)
$p\bar{p} \rightarrow WX(ZX)$ (UA1, UA2; CDF, D0) $\rightarrow \ell^\pm$ asym (CDF)*	$ud \rightarrow W$	u, d at $x \simeq M_W/\sqrt{s} \rightarrow$ $x \approx 0.13; 0.05$ slope of u/d at $x \approx 0.05 - 0.1$
$p\bar{p} \rightarrow t\bar{t}X$ (CDF, D0)	$q\bar{q}, gg \rightarrow t\bar{t}$	q, g at $x \gtrsim 2m_t/\sqrt{s} \simeq 0.2$
$p\bar{p} \rightarrow \text{jet} + X$ (CDF, D0)	$gg, qg, qq \rightarrow 2j$	q, g at $x \simeq 2E_T/\sqrt{s} \rightarrow$ $x \approx 0.05 - 0.5$

The output MRST parton distributions evolved to $Q^2 = 20 \text{ GeV}^2$ are shown in Fig. 3. At

this Q^2 , the expected fractions of the total momentum carried by the valence quarks is 25% (u_v) and 10% (d_v). 6% ($2\bar{u}$), 8% ($2\bar{d}$), 5% ($2s$) and 2% ($2c$) is carried by the $q\bar{q}$ symmetric sea and 44% (g) is carried by the gluons.

Incorporating new datasets and theoretical understanding improves the precision with which individual parton densities are known. In particular, uncertainties in d/u at high x , \bar{d}/\bar{u} at intermediate x , s at all x values, g at low x and c at low x , are discussed in the context of the presentations made at ICHEP98.

2 Fixed-Target Results

2.1 Determination of α_s

Gross-Llewellyn Smith (GLS) Sum Rule: The GLS sum rule expresses the fact that there are three valence quarks in the nucleon, subject to QCD corrections

$$\int_0^1 xF_3(x, Q^2) \frac{dx}{x} = 3\left(1 - \frac{\alpha_s}{\pi} - a_2\left(\frac{\alpha_s}{\pi}\right)^2 - a_3\left(\frac{\alpha_s}{\pi}\right)^3\right) - \frac{\Delta HT}{Q^2}.$$

This is a fundamental prediction of QCD which, as a non-singlet quantity, is independent of the gluon distribution. The sum rule has been calculated to $\mathcal{O}(\alpha_s^3)$ and estimated to $\mathcal{O}(\alpha_s^4)$ [9, 10]. The CCFR collaboration have now published their final results [11], incorporating earlier neutrino measurements (WA25, WA59, SKAT, FNAL-E180 and BEBC-Gargamelle) to determine the GLS sum rule. In Fig. 4, the sum rule is proportional to the area under the data in four regions of Q^2 . The analysis of the world data enables $\alpha_s(3 \text{ GeV}^2)$ to be determined at NNLO ($\mathcal{O}(\alpha_s^3)$) accuracy and evolved to M_Z^2 as

$$\alpha_s(M_Z^2) = 0.114_{-0.006}^{+0.005}(\text{stat.})_{-0.009}^{+0.007}(\text{sys.})_{-0.005}^{+0.004}(\text{theory}).$$

The largest contribution to the systematic error is the uncertainty on the ratio of the total neutrino and anti-neutrino cross-sections, $\sigma_{\bar{\nu}}/\sigma_{\nu} = 0.499 \pm 0.007$ which determines the overall normalisation of xF_3 . This uncertainty will be improved with the NuTeV tagged ν - $\bar{\nu}$ beamline. The nuclear target corrections to the GLS sum rule are predicted to be small [12]. The largest theory uncertainty is that associated with the higher twist contribution, $\Delta HT = 0.15 \pm 0.15 \text{ GeV}^2$. Here, a renormalon approach, where chains of vacuum polarisation bubbles on a gluon propagator lead to a prediction of the higher twist contribution in the perturbative expansion, predicts a small correction, $\Delta HT < 0.02 \text{ GeV}^2$. Other models predict significantly larger HT corrections and the uncertainty encompasses this range. The renormalon approach is now rather successful in describing a range of power corrections to hadronic final state variables [5] and leads to a central value of $\alpha_s(M_Z^2) = 0.118$. The most recent analysis of the xF_3 data determines the same central value with a similar theoretical uncertainty [13].

Scaling Violations at Large x : The most accurate method to determine $\alpha_s(M_Z^2)$ from the CCFR data remains the measurement of the scaling violations of the structure functions, F_2 and xF_3 , using a NLO QCD fit [14]. The scaling violation slopes $d(\log F_2)/d \log Q^2$ and

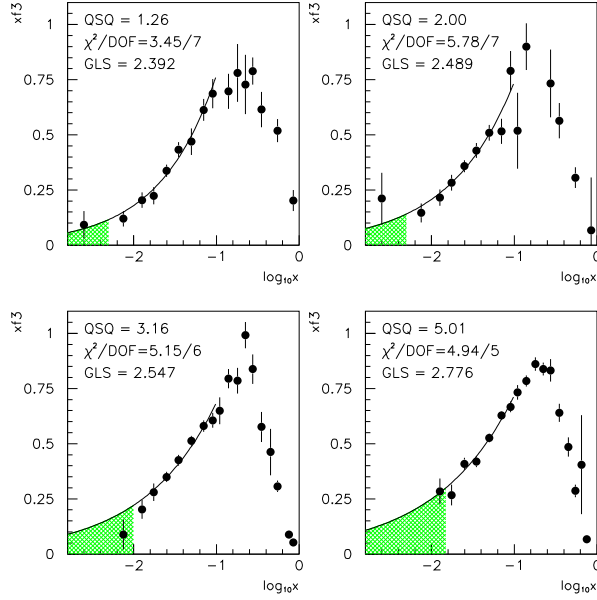


Figure 4: CCFR analysis of xF_3 versus $\log_{10}(x)$ for four ranges of Q^2 . The curve indicates a power law (Ax^B) fit applied for $x < 0.1$ used to determine the integral in the unmeasured shaded region.

$d(\log xF_3)/d\log Q^2$ are shown in Fig. 5. From F_2 , the high- x gluon is also constrained to be

$$xg(x, Q_0^2 = 5 \text{ GeV}^2) = (2.22 \pm 0.34) \times (1 - x)^{4.65 \pm 0.68}$$

in agreement with global analyses using prompt photon data. From the combined results on F_2 and xF_3

$$\alpha_s(M_Z^2) = 0.119 \pm 0.002(\text{exp.}) \pm 0.001(\text{HT}) \pm 0.004(\text{scale})$$

which represents one of the most precise determinations of this quantity. This improved measurement is higher than the earlier CCFR value due to the use of a new energy calibration. It is also higher than the SLAC/BCDMS analysis value of $\alpha_s(M_Z^2) = 0.113 \pm 0.003(\text{exp.}) \pm 0.004(\text{theory})$ [15]. Here it is noted that there is a small but statistically significant discrepancy between the SLAC and BCDMS data (see the $x \geq 0.45$ F_2^p points in Fig. 6), which can be resolved if the correlated systematics of the BCDMS data at low y are taken into account. The quoted central value of the combined analysis, however, does not take these systematics into account [17]. There is therefore little evidence for any discrepancy with respect to the world average value $\alpha_s^{PDG}(M_Z^2) = 0.119 \pm 0.002$ [16].

Improved statistics will enable the NuTeV collaboration to determine α_s decoupled from the gluon using the xF_3 data alone. Further progress in the F_2 analysis requires the calculation of NNLO terms in order to reduce the renormalisation and factorisation scale uncertainties. In this way the overall uncertainty on $\alpha_s(M_Z^2)$ can be reduced to ± 0.002 . In this area, there is still an outstanding 20% discrepancy between the CCFR F_2^ν and NMC F_2^μ data in the region of $x \sim 10^{-2}$ which is discussed in the context of the strange quark sea and the ZEUS preliminary data later. However, this effect is negligible in the determination of α_s , which depends mainly upon the high- x data as seen in Fig. 5.

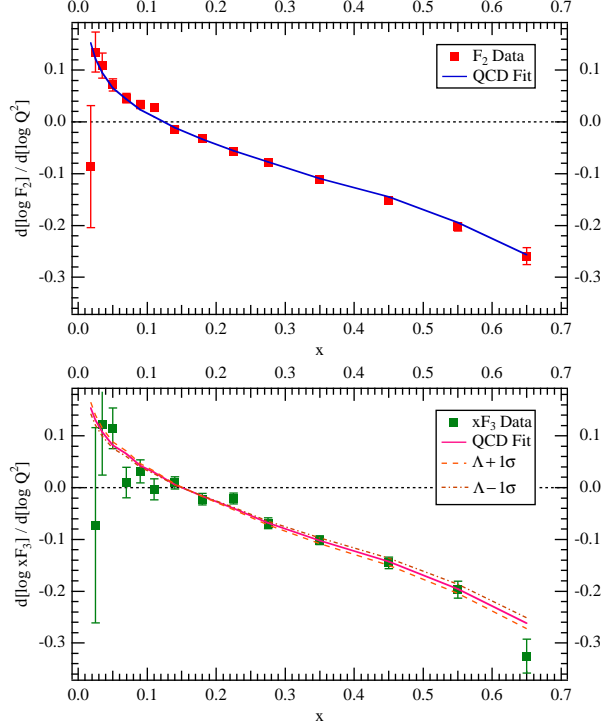


Figure 5: CCFR results on the scaling violations of F_2 (upper plot) and xF_3 (lower plot) compared to a NLO QCD fit.

2.2 Nucleon Structure

d/u at large x: Valence parton distributions at high x received attention at this conference provoked by new data and corrections of the d/u ratio from an analysis by U. Yang and A. Bodek [18]. Extractions of F_2^n from NMC and SLAC deuteron data have previously accounted for Fermi motion but not nuclear binding effects. A physically appealing model by Frankfurt and Strikman [19] assumes that binding effects in the deuteron and heavier nuclear targets scale with the nuclear density. This nuclear binding correction is about 4% at $x = 0.7$ for fixed-target deuteron experiments, which is parameterised as an additional term $\delta(d/u) = (0.10 \pm 0.01)x(1 + x)$ added to the MRS(R2) PDF. This is sufficient to increase the d distribution significantly at high $Q^2 = 10^4 \text{ GeV}^2$ by about 40% at $x = 0.5$, due to DGLAP evolution of the partons. The modification gives an improved fit to the NMC deuteron data. It is compelling in that this simple modification now improves the description of high- x CDHSW $\nu p/\bar{\nu} p$ data (not shown) as well as the new data on the W asymmetry from CDF (probing intermediate $x \simeq M_W/\sqrt{s} \simeq 0.05$ values) and the charged current cross-sections from ZEUS (see later), data which are free from nuclear binding effects.

The world F_2^p and F_2^d fixed-target data at high x is plotted in Fig. 6. Here the NLO pQCD calculation incorporates target mass (TM) effects determined using Georgi-Politzer scaling where the scaling variable x is replaced by $\xi = 2x/(1 + \sqrt{1 + 4M^2x^2/Q^2})$ as well as the correction for nuclear binding effects for the deuteron data. The description of the low Q^2 data is significantly improved ($\chi^2/DoF = 1577/1045$) if higher twist (HT) corrections are incorporated as indicated by the fit denoted NLO(pQCD+TM+HT) [18]. A good description is

also obtained for the very high x SLAC DIS data (not shown) up to $x = 0.9$, although there is some residual Q^2 dependence in the resonance region ($0.9 < x < 1$). The renormalon approach [20] therefore successfully predicts the x dependence of the higher twist terms although the normalisation constant is half of the previously estimated value. This renormalon approach also successfully describes the Q^2 dependence of $R = \sigma_L/\sigma_T$ (not shown). In a NNLO fit this higher twist contribution tends to zero which suggests that the non-singlet higher twist contribution (relevant for xF_3) is also small, as discussed in relation to the GLS sum rule. In addition, new measurements of R , covering the range of $0.015 < x < 0.55$ from CCFR were presented which are in agreement with those from EMC, BCDMS and SLAC and extend the kinematic range up to $Q^2 \sim 100 \text{ GeV}^2$ [21].

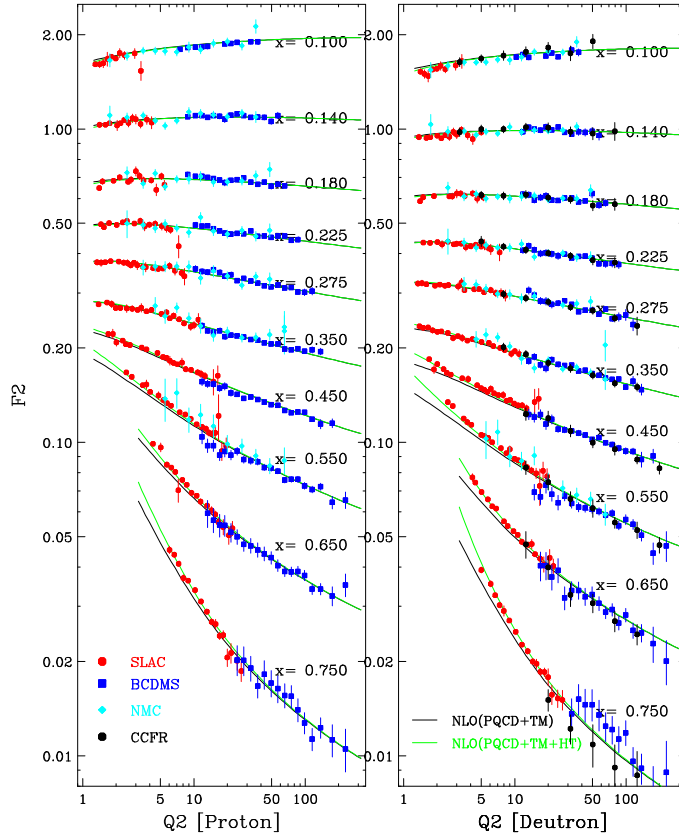


Figure 6: Comparison of high- x F_2^p and F_2^d data versus Q^2 fitted with and without higher twist (HT) corrections. The error bars correspond to statistical and systematic errors added in quadrature.

As can be seen in Fig. 3, the u quarks in the proton carry more momentum on average than the d quarks. (The \bar{d} quarks carry only slightly more momentum than the \bar{u} quarks at high x .) W^+ and W^- production in $\bar{p}p$ collisions is primarily due to the annihilation processes $u(p)\bar{d}(\bar{p}) \rightarrow W^+$ and $\bar{u}(\bar{p})d(p) \rightarrow W^-$. On average the W^+ 's are therefore produced relatively more forward than the W^- 's. CDF [22] measure the lepton asymmetry from the W decays,

$$A(y_l) = \frac{d\sigma^+/dy_l - d\sigma^-/dy_l}{d\sigma^+/dy_l + d\sigma^-/dy_l},$$

where $d\sigma^\pm/dy_l$ are the cross-sections for W^\pm decay leptons as a function of lepton rapidity relative to the proton beam direction. The W decay to leptons tends to reduce the asymmetry at forward $|y_l|$ but in a well-defined manner (assuming the W decays proceed via a SM V-A interaction). In Fig. 7, the final results from runs Ia and Ib are shown compared to various PDF's using the DYRAD NLO calculations. The best agreement with the data is obtained using the modified MRS(R2) or the MRST PDF (not shown), which incorporates this data as input, indicating that the ratio of d/u is larger than previously thought.

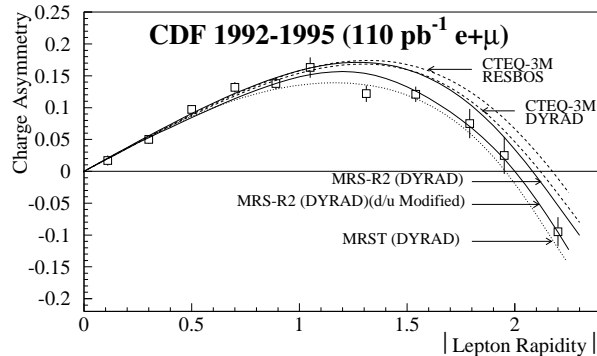


Figure 7: CDF lepton charge asymmetry from W decays as a function of lepton rapidity. The error bars correspond to statistical and systematic errors added in quadrature.

\bar{d}/\bar{u} at intermediate x : The structure function measurements constrain the sum of \bar{d} and \bar{u} but not the difference. The classic method to constrain this difference is via the Gottfried sum rule where

$$S_G = \int_0^1 F_2^p - F_2^n \frac{dx}{x} = \frac{1}{3} \int_0^1 (d_v - u_v) dx - \frac{2}{3} \int_0^1 (\bar{d} - \bar{u}) dx.$$

The NMC result for $0.004 < x < 0.8$ extrapolated over all x gives $S_G = 0.235 \pm 0.026$, significantly below $1/3$ [23]. It should be noted however that the deuterium data used to derive F_2^n are not corrected for the effects noted above. This correction is estimated to be -0.013 i.e. 50% of the uncertainty [24].

At this conference, the E866 data were reported [25], which provide a significant constraint on the ratio of \bar{d}/\bar{u} via the measurement of Drell-Yan dimuons with mass $M_{\mu^+\mu^-} \geq 4.5$ GeV from 800 GeV protons on proton and deuterium targets as shown in Fig. 8. Here, the ratio of $\sigma^{pd}/2\sigma^{pp}$ is measured as a function of the reconstructed momentum fraction of the target quark in the range $0.036 < x_2 < 0.312$. The MRST calculations incorporate a direct parameterisation of $\bar{d} - \bar{u}$ in order to fit the data. Earlier PDF's such as MRS(R2) clearly overestimate this asymmetry but a $\bar{d} = \bar{u}$ sea is still ruled out.

The E866 data require an overall decrease of the sea compared to the MRS(R2) parameterisation. This is seen in the lower part of Fig. 9 where the E866 data are plotted as the sea contribution to $F_2^p(x) - F_2^n(x)$, which contributes negatively to S_G , evolved to the NMC Q^2 values. The NMC data are plotted in the upper plot, compared to the valence as well as the summed contribution for the MRST and MRS(R2) partons. Although the valence and sea distributions differ, these distributions give similar results for the total $F_2^p(x) - F_2^n(x)$. However, it

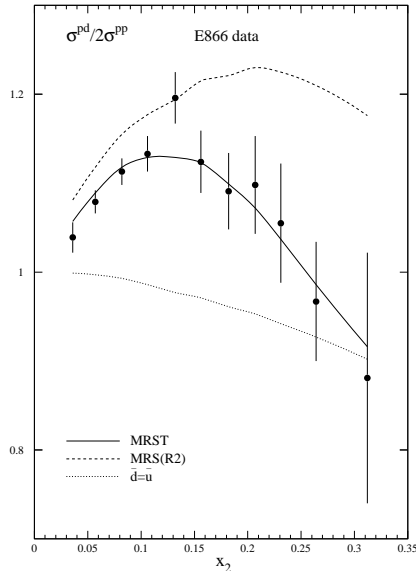


Figure 8: E866 ratio of $\sigma^{pp}/2\sigma^{pd}$ versus x_2 , the momentum fraction of the target quark, compared to the NLO calculations discussed in the text.

is clear that the agreement of the NMC data with either parameterisation is poor at intermediate x , which would require additional changes to the valence quark distributions. The MRST NLO fits determine $S_G = 0.266$, above the NMC measured value discussed earlier. This discrepancy is induced in part by the inclusion of the E866 data in the fit.

A further constraint is provided via the HERMES semi-inclusive measurement of the ratio of the differences between charged pion production for (unpolarised) proton and neutron (${}^3\text{He}$) targets

$$r(x, z) = \frac{N_p^{\pi^-}(x, z) - N_n^{\pi^-}(x, z)}{N_p^{\pi^+}(x, z) - N_n^{\pi^+}(x, z)},$$

also reported at this conference [27]. The ratio is observed to scale as a function of the fragmentation scaling variable z and the data are used to constrain $(\bar{d} - \bar{u})/(u - d)$ at leading order as a function of x , as shown in Fig. 10a. Using the PDF's to constrain the valence quarks, the $\bar{d} - \bar{u}$ distribution obtained from the E866 and (lower Q^2) HERMES data are shown to be in agreement in Fig. 10b.

Generically, the Pauli exclusion principle, suppresses production of sea $u\bar{u}$ quarks at large x due to the additional u_v quark. Hence the excess of \bar{d} over \bar{u} is a direct consequence of the excess of u_v over d_v . The currently favoured dynamical approach is to include non-perturbative effects from virtual mesons directly from $|n\pi^+ \rangle$ Fock states in a virtual pion model or to derive the sea from the valence quarks coupling to Goldstone bosons (e.g. π^+ from $u \rightarrow d\pi^+$) in a chiral model [26]. In conclusion, the latest data indicate that the ratio of \bar{d}/\bar{u} is less than previously thought, a decrease which is correlated with the increase of d/u .

s quark contribution: The strange contribution to the quark sea is determined using opposite-sign dimuon events in νFe scattering from CCFR where one muon comes from the lepton vertex

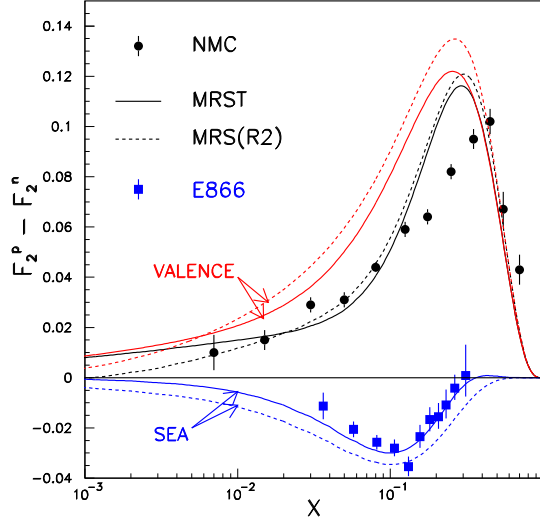


Figure 9: NMC $F_2^p - F_2^n$ versus x compared to LO predictions discussed in the text. For each prediction, the top (bottom) curve is the valence (sea) contribution and the middle curve is the sum. The E866 results for the sea quark contribution to $F_2^p - F_2^n$ are indicated as the negative contribution.

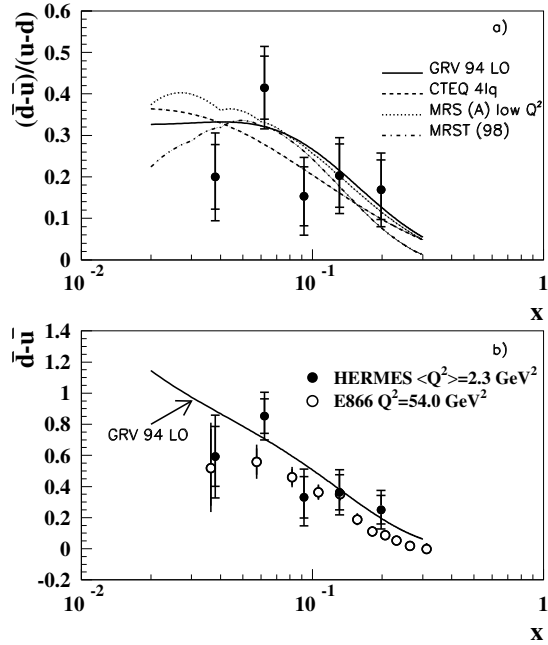


Figure 10: a) $(\bar{d} - \bar{u})(u - d)$ extracted directly from HERMES data (\bullet) compared to various parameterisations of the proton. b) HERMES data converted to $\bar{d} - \bar{u}$ in order to compare with E866 (\circ) data.

and the other results from the semi-leptonic decay of a charmed hadron. The ratio of s to u and d quarks integrated over x in an NLO analysis was determined to be $0.477^{+0.063}_{-0.053}$ [29]. This large uncertainty requires, for example, that NuTeV tag ν and $\bar{\nu}$ and take the difference of these cross-sections in order to reduce the uncertainty on $\sin^2\theta_W$, also reviewed at this conference [30]. A second potential method to constrain the strange quark contribution is by comparing $F_2^{\nu N}$ and F_2^{lN} . The analysis of this data was discussed by C. Boros [28]. To leading order the muon (NMC) and neutrino (CCFR) structure functions are related by the “5/18ths rule”

$$F_2^{lN} = \frac{5}{18} \left[1 - \frac{3}{5} \frac{xs(x) + x\bar{s}(x)}{xq(x) + x\bar{q}(x)} \right] F_2^{\nu N}$$

where the ($s\bar{s}$ symmetric) strange sea enters as a correction. However, the CCFR data corrected using the dimuon result to constrain the strange sea lies significantly ($\simeq 20\%$) above the NMC data for all values of Q^2 at $x < 0.1$. Here nuclear shadowing corrections, estimated independently for νFe (CCFR) and μD (NMC) data, indicate that part of the discrepancy between the two experiments at low x may be accounted for in this way [28]. However, there remains a significant discrepancy: the strange quark sea and the relation between $F_2^{\nu N}$ and F_2^{lN} data for $x < 0.1$ is therefore an active area of theoretical and experimental investigation.

3 Spin Structure Functions

Major progress has been made in the last two years in the measurement and QCD analysis of spin structure functions. The second generation CERN and SLAC experiments have been augmented by the HERMES experiment at DESY and these experiments now provide detailed information on the proton, neutron and deuteron spin structure. Here, we discuss measurements of the longitudinal asymmetry

$$A_{\parallel} = \frac{\sigma^{\downarrow\uparrow} - \sigma^{\uparrow\uparrow}}{\sigma^{\downarrow\uparrow} + \sigma^{\uparrow\uparrow}}$$

where $\sigma^{\uparrow\uparrow}$ ($\sigma^{\downarrow\uparrow}$) is the cross-section when the lepton and nucleon spins are parallel (antiparallel) to each other. This asymmetry takes into account the beam and target polarisations as well as the dilution factor, the fraction of polarisable nucleons in the target. The asymmetry can then be related to the virtual-photon nucleon asymmetries A_1 and A_2

$$A_{\parallel} = D(A_1 + \eta A_2)$$

where D is the depolarisation factor depending upon $R = \sigma_L/\sigma_T$ and $\eta = \eta(x, Q^2)$ is a kinematic factor. The spin structure function

$$g_1 = \frac{F_2}{2x(1+R)} (A_1 + \gamma A_2)$$

where γ is a further kinematic factor and g_1 is then calculated using the known F_2 and R values. The A_1 term dominates and to a reasonable approximation the extracted structure function is proportional to the measured asymmetry

$$g_1 \simeq \frac{F_2}{2x(1+R)} \cdot A_1 \simeq F_1 \cdot \frac{A_{\parallel}}{D}.$$

In the Quark Parton Model

$$g_1(x, Q^2) = \frac{1}{2} \sum_i e_i^2 \cdot \Delta\Sigma(x, Q^2)$$

where $\Delta\Sigma = \sum_i [(q_i^\uparrow - q_i^\downarrow) + (\bar{q}_i^\uparrow - \bar{q}_i^\downarrow)]$ is the singlet summed quark and anti-quark distributions where q^\uparrow (q^\downarrow) is the quark distribution with the spins parallel (antiparallel) to the nucleon spin. In the QPM g_1 is therefore the charge-weighted vector sum of the quark polarisations in the nucleon. Similarly the non-singlet quark distribution $\Delta_{q_{NS}} = \sum_i \frac{e_i^2 - \langle e^2 \rangle}{\langle e^2 \rangle} [(q_i^\uparrow - q_i^\downarrow) + (\bar{q}_i^\uparrow - \bar{q}_i^\downarrow)]$, where $\langle e^2 \rangle = 2/9$ for 3 light flavours is defined such that this contribution evolves separately from the gluon (Δg) and singlet ($\Delta\Sigma$) contributions when QCD corrections are taken into account. The DGLAP formalism outlined earlier can therefore be applied and $\Delta_{q_{NS}}$ constrained by g_1 via QCD corrections.

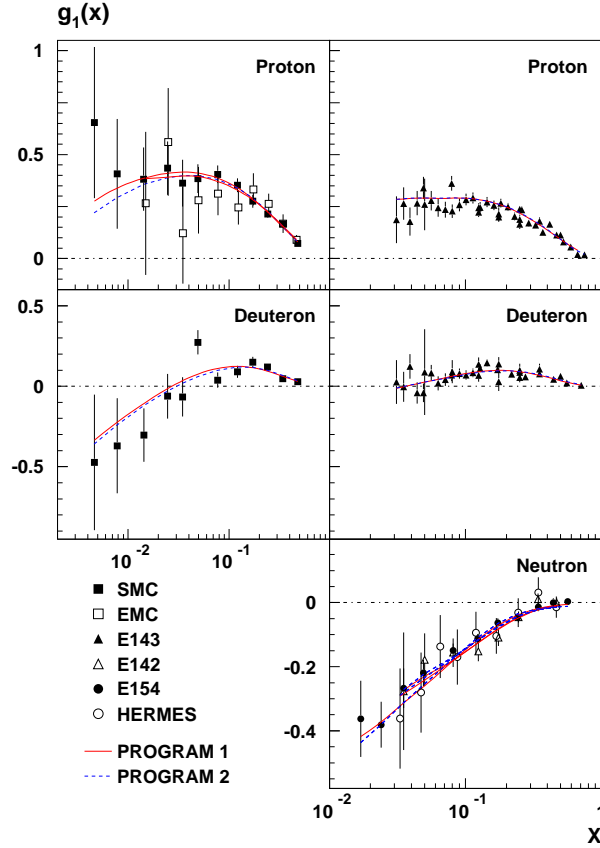


Figure 11: Published world data on $g_1(x)$ from CERN experiments ($0.003 < x < 0.6$, $1 < Q^2 < 100 \text{ GeV}^2$) in the left column and SLAC and DESY experiments ($0.014 < x < 0.7$, $1 < Q^2 < 20 \text{ GeV}^2$) in the right column with statistical errors only. Results from two ($\overline{\text{MS}}$ scheme) NLO QCD fitting programs discussed in the text are superimposed.

The corresponding integrals $\Gamma_1 = \int_0^1 g_1(x, Q^2) dx$ determine the total spin carried by the quarks at the measured Q^2 . In the QPM, below charm threshold

$$\Gamma_1^p = \frac{1}{2} \left(\frac{4}{9} \Delta u + \frac{1}{9} \Delta d + \frac{1}{9} \Delta s \right)$$

and, by isospin symmetry

$$\Gamma_1^n = \frac{1}{2} \left(\frac{1}{9} \Delta u + \frac{4}{9} \Delta d + \frac{1}{9} \Delta s \right)$$

Beyond the QPM, the total spin of the nucleon can be written as the sum of the contributions from its constituents

$$\frac{1}{2} = \frac{1}{2} \Delta \Sigma + \Delta g + L_q + L_g$$

where the Δ 's correspond to the intrinsic spins and the L 's correspond to the angular momentum of the quarks and gluons. The proton spin puzzle is that only a fraction of the total spin is due to quarks. This puzzle remains, but first steps have now been taken to constrain the gluon contribution via the scaling violations of $g_1(x)$ and the valence and sea quark contributions via semi-inclusive measurements.

The world data on $g_1(x)$ for the proton, deuteron and neutron are summarised in Fig. 11 for the CERN, SLAC and DESY experiments [31]. Comparison of the lower and higher Q^2 data indicates that the scaling violations are relatively small over the well-measured range of $1 < Q^2 \lesssim 10 \text{ GeV}^2$. The data are taken using a variety of targets (e.g. H(p), D(d) and $^3\text{He}(n)$) for HERMES; NH₃(p), ND₃(d), $^6\text{Li}(d)$ and $^3\text{He}(n)$ for the SLAC experiments; and, NH₃(p), butanol(p) and deuterated-butanol(d) for SMC) and widely varying experimental techniques.

There is no evidence for a rise of g_1^p at the smallest values of $x \sim 10^{-2}$ explored by SMC and E155. Indeed the QCD fit prediction is that g_1^p becomes negative for $x \lesssim 10^{-3}$ due to the relatively large positively polarised gluon at higher x driving the polarised gluon negative at small x [32]. Clearly this will be of interest in the light of the HERA unpolarised results and of significance in the extrapolations required for the determination of the sum rules. SMC presented data on the virtual-photon proton asymmetry, A_1^p at low $\langle Q^2 \rangle = 0.01 \text{ GeV}^2$ which extend to very low $x = 10^{-4}$, as shown in Fig. 12 [34]. The low x data were obtained with a dedicated low- Q^2 trigger, requiring an observed hadron in each event which rejects radiative and other events with low depolarisation factors. At these very low Q^2 values the data indicate that extreme QCD behaviour of $g_1^p \propto 1/x \ln^2 x$ (full line) proposed in [35] is ruled out. However the less extreme QCD behaviours $g_1^p \propto \ln x$ or $2 + \ln x$ indicated by the dotted lines give reasonable descriptions of the data. Clearly higher Q^2 data are desirable in order to test the pQCD models, but the data do constrain the Regge behaviour.

The values of g_1^n in Fig. 11 fall monotonically with decreasing x . The precision of this data is now approaching that of the proton data, which is important in the context of the Bjorken sum rule discussed below. All data are observed to be in good agreement, where the systematic errors (not shown) are typically smaller than the statistical errors. In addition, E155 presented new preliminary data on g_1^p and g_1^n (not shown) at $Q^2 = 5 \text{ GeV}^2$ which are in good agreement with these published datasets [33]. These data have very small statistical errors and extend the x range compared to the E143 data. This improved precision also requires that nuclear effects due to the assumed superposition of D and ^4He states in the ^6Li target data are understood, but possible uncertainties can be tested by comparison with data from different targets and other experiments.

SMC have performed a NLO QCD fit [31] to extract the singlet ($x \cdot \Delta \Sigma$) and gluon ($x \cdot \Delta g$) as well as the proton ($x \cdot \Delta q_{NS}^p$) and neutron ($x \cdot \Delta q_{NS}^n$) non-singlet polarised parton distributions

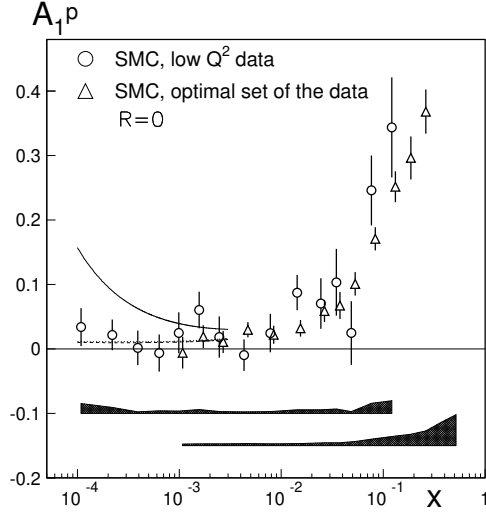


Figure 12: SMC virtual-photon proton asymmetry, A_1^p , for $\langle Q^2 \rangle = 0.01 \text{ GeV}^2$ data as a function of x compared to the behaviours discussed in the text. The systematic errors for the low (x, Q^2) and the reference set of data are indicated by the shaded bands.

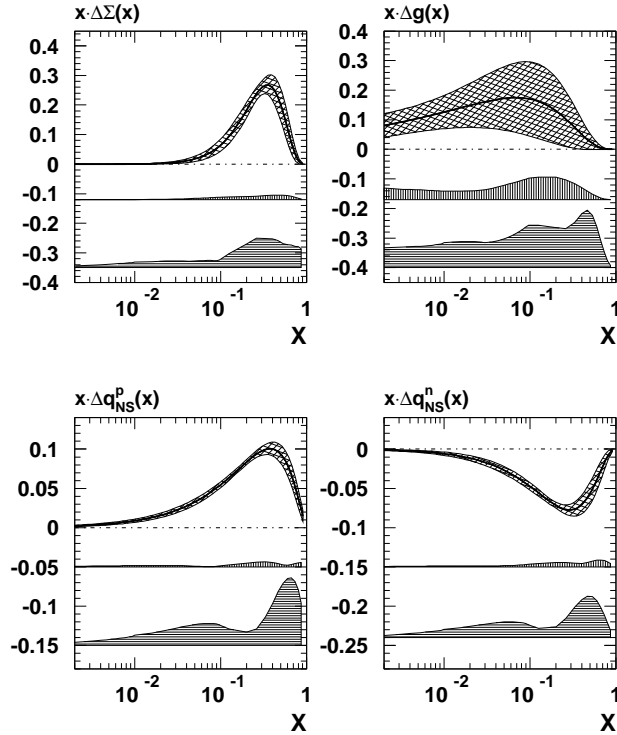


Figure 13: SMC QCD analysis of world g_1 data: singlet, gluon, proton and neutron non-singlet polarised parton distributions in AB scheme at $Q_0^2 = 1 \text{ GeV}^2$. The fits with the statistical uncertainty are indicated by the cross hatched upper bands. The (small) experimental systematic uncertainties are indicated by the central bands and the (larger) theoretical uncertainties by the lower bands.

shown in Fig. 13. Here, the deuteron spin structure function g_1^d is assumed to be related to the

proton and neutron structure functions by

$$g_1^p + g_1^n = \frac{2g_1^d}{1 - \frac{3}{2}\omega_D}$$

where $\omega_D = 0.05 \pm 0.01$ is the D-wave state probability in the deuteron.

The results of the fits from two NLO QCD programs are shown by the full and dashed lines in Fig. 11 at the measured Q^2 of each of the datasets. The comparison indicates that a good fit is obtained to the world data with $\chi^2/Dof = 127.4/(133 - 8)$, considering statistical errors only. The parton densities are parameterised and determined in analogy to the unpolarised case via the NLO DGLAP splitting kernels. Results are quoted in the Adler-Bardeen (AB) scheme, a modified version of the more conventional $\overline{\text{MS}}$ scheme, defined such that $\Delta\Sigma_{\text{AB}}$ is independent of Q^2 . These renormalisation/factorisation schemes are related via

$$\begin{aligned} a_0(Q^2) &= \Delta\Sigma_{\overline{\text{MS}}}(Q^2) \\ &= \Delta\Sigma_{\text{AB}} - n_f \frac{\alpha_s(Q^2)}{2\pi} \Delta g_{\text{AB}}(Q^2) \end{aligned}$$

where $a_0(Q^2)$ is the singlet axial-current matrix element and the Δ 's correspond to the parton densities integrated over x . This scheme dependence is large and sufficient to create a negative $\Delta\Sigma(x)$ at small x and a smaller $\Delta g(x)$ in $\overline{\text{MS}}$ scheme [31]. However, the physical structure functions and their integrals, such as $a_0(Q^2)$ are unaffected by this definition. In Fig. 13, the singlet contribution is seen to be well constrained by g_1^p . This remains true when account is taken of the theoretical uncertainties which include the variation of the renormalisation and factorisation scale by factors of two, varying $\alpha_s = 0.118 \pm 0.003$ within the given limits and changes to the starting scale and the functional forms of the parameters. Similarly the non-singlet contributions are reasonably well constrained and the rise of Δq_{NS}^p is mirrored by the fall of Δq_{NS}^n . However, Δg is rather poorly constrained especially when taking into account the theoretical uncertainties. Integrating over x at $Q_o^2 = 1 \text{ GeV}^2$

$$\Delta g = 0.99_{-0.31}^{+1.17}(\text{stat.})_{-0.22}^{+0.42}(\text{sys.})_{-0.45}^{+1.43}(\text{theory})$$

in AB scheme compared to $\Delta g = 0.25_{-0.22}^{+0.29}(\text{stat.})$ in $\overline{\text{MS}}$ scheme. Consistent results are obtained in either scheme for the singlet contribution expressed in terms of the axial-current matrix element

$$a_0(Q_o^2 = 1 \text{ GeV}^2) = 0.23 \pm 0.07(\text{stat.}) \pm 0.19(\text{sys.})$$

which compares to the QPM expectation $\simeq 0.58$ and corresponds to about one third of the nucleon spin being carried by quarks.

In the latest analysis by J. Ellis and M. Karliner [36], the world average value of the singlet matrix element in $\overline{\text{MS}}$ scheme is given by

$$\Delta\Sigma = 0.27 \pm 0.05.$$

This approach utilises the $\mathcal{O}(\alpha_s^3)$ calculations and $\mathcal{O}(\alpha_s^4)$ estimates discussed below in relation to the Bjorken sum rule. Here, the consistency of the data taken at different Q^2 values improves as successive higher-order QCD corrections are taken into account.

Bjorken Sum Rule: The Bjorken sum rule is a fundamental prediction of QCD determined by the difference of the spins carried by the u and the d quarks

$$\Gamma_1^p - \Gamma_1^n = \int_0^1 (g_1^p - g_1^n) dx = \frac{1}{6} \left| \frac{g_A}{g_V} \right| \cdot C_1^{NS}(Q^2)$$

where g_A and g_V are the axial-vector and vector weak coupling constants of neutron β -decay and $C_1^{NS}(Q^2)$ is the non-singlet perturbative QCD correction which has been calculated up to $\mathcal{O}(\alpha_s^3)$ and estimated up to $\mathcal{O}(\alpha_s^4)$ using the same approach as for the GLS sum rule [9, 10]. Here, higher twist contributions to the difference of the structure functions are assumed to be negligibly small.

In the SMC NLO fits discussed above, the sum rule is imposed as an input with $|\frac{g_A}{g_V}|$ fixed rather precisely from β -decay experiments. However, the NLO fits provide two methods to check the Bjorken sum rule. First, the input can be relaxed and $|\frac{g_A}{g_V}|$ fitted as an additional parameter in the global fit yielding

$$\Gamma_1^p - \Gamma_1^n = 0.174 \pm 0.005(stat.)_{-0.009}^{+0.011}(sys.)_{-0.006}^{+0.021}(theory)$$

at $Q^2 = 5 \text{ GeV}^2$, which is in agreement with the theoretically expected value of 0.181 ± 0.003 . Second, the non-singlet contributions $g_1^p - g_1^n$ can be evolved to a common Q^2 in order to determine the sum rule more directly and with a minimum number of parameters. This yields a consistent value of $0.181_{-0.021}^{+0.026}(total)$ when evaluated at $\mathcal{O}(\alpha_s^2)$. This second method is potentially more precise, but awaits the high statistics data on g_1^p from E155 combined with the existing data on g_1^n from E154.

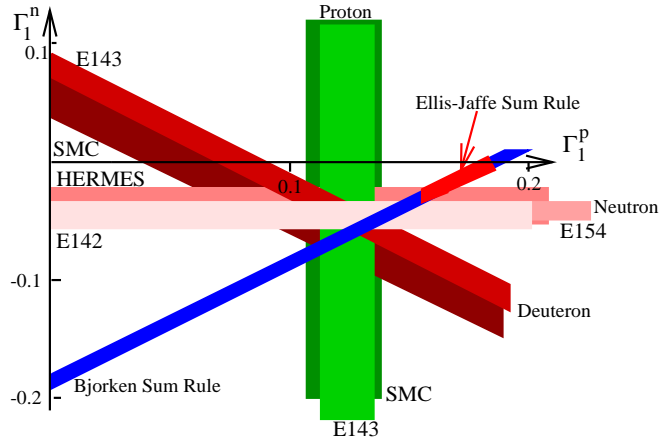


Figure 14: Spin sum rules Γ_1^p versus Γ_1^n . Proton (E143 and SMC) and neutron (E142, E154 and HERMES) data are indicated by the vertical and horizontal bands, respectively. Deuteron (E143 and SMC) data are indicated by the falling diagonal bands. The theoretical expectation from the Bjorken sum rule ($= \Gamma_1^p - \Gamma_1^n$) is indicated by the rising diagonal band while the Ellis-Jaffe sum rule is the area on this band indicated by the arrow.

Ellis-Jaffe Sum Rule: Assuming that strange quarks do not contribute to the nucleon spin and $SU(3)_f$ symmetry, Ellis and Jaffe derived independent sum rules for the proton and neutron

$$\Gamma_1^p = \frac{1}{2} \left(\frac{4}{9} \Delta u + \frac{1}{9} \Delta d \right) \simeq 0.17$$

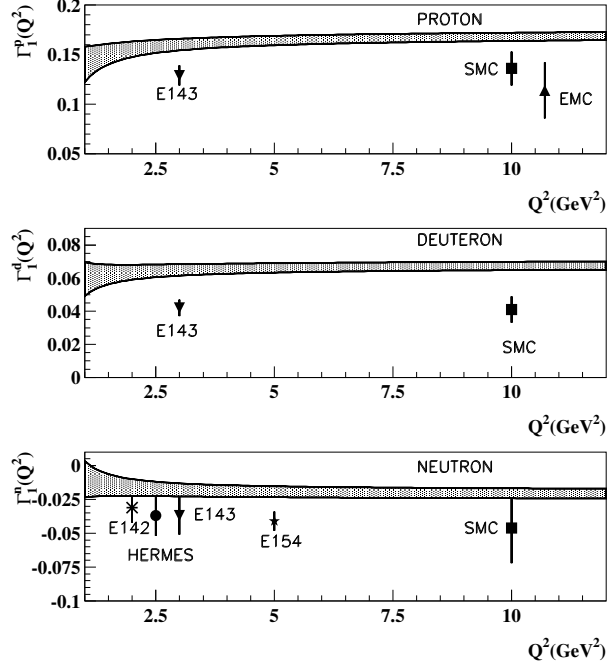


Figure 15: Spin integrals, Γ_1 proton, deuteron and neutron data versus Q^2 compared to the Ellis-Jaffe sum rule ($\Delta s = 0$ and $SU(3)_f$ symmetry) expectation indicated by the shaded band.

$$\Gamma_1^n = \frac{1}{2} \left(\frac{1}{9} \Delta u + \frac{4}{9} \Delta d \right) \simeq -0.02$$

in the high- Q^2 limit and modified by singlet and non-singlet QCD corrections. In Fig. 14 the world data on the Bjorken and Ellis-Jaffe sum rules are depicted graphically. As noted in relation to the SMC analysis, the data are in agreement and consistent with the Bjorken sum rule with a precision of around 10%. The origin of the spin puzzle was the EMC measurement of Γ_1^p . In Fig. 15, the world data on Γ_1^p , Γ_1^d and Γ_1^n all indicate that the Ellis-Jaffe sum rule is broken at the 2-3 σ level. The strange sea quarks and/or the gluon therefore carry a significant fraction of the spin. It is currently impossible to distinguish an $SU(3)_f$ symmetric sea or a $\Delta s = 0$ (large gluon) solution in the NLO QCD fits [37]. A natural assumption would be that $SU(3)_f$ symmetry is violated at the same level as in the unpolarised structure functions and the rest of the spin can be attributed to a large gluon polarisation, but this requires further experimental input.

Semi-inclusive Asymmetries: SMC [38] and HERMES [39] have recently produced data tagging the charge of final state hadrons. The asymmetry $A_{||}^h(x, z)$ is defined in analogy to the inclusive case where the distribution of charged hadrons with momentum fraction z is statistically correlated with the struck quark flavour in a flavour tagging analysis. In Fig. 16 the extracted spin contributions Δu_v , Δd_v and $\Delta \bar{q}$ (introduced for $x < 0.3$) from SMC and HERMES are observed to be in agreement. Slightly different assumptions are made with respect to the strange quark sea where SMC assume an $SU(3)_f$ symmetric sea and HERMES assume this symmetry is violated at the same level as in the unpolarised structure functions. However these effects are negligible for the predominantly pion final states in this LO QCD analysis. Both experiments

observe Δu_v is positive and Δd_v is negative. The SMC results integrated over x are

$$\begin{aligned}\Delta u_v &= +0.77 \pm 0.10(stat.) \pm 0.08(sys.) \\ \Delta d_v &= -0.52 \pm 0.14(stat.) \pm 0.09(sys.) \\ \Delta \bar{q} &= +0.01 \pm 0.04(stat.) \pm 0.03(sys.)\end{aligned}$$

in agreement with the expectations from the NLO QCD fits. The polarised sea is compatible with zero although there are indications from the HERMES data that this contributes positively.

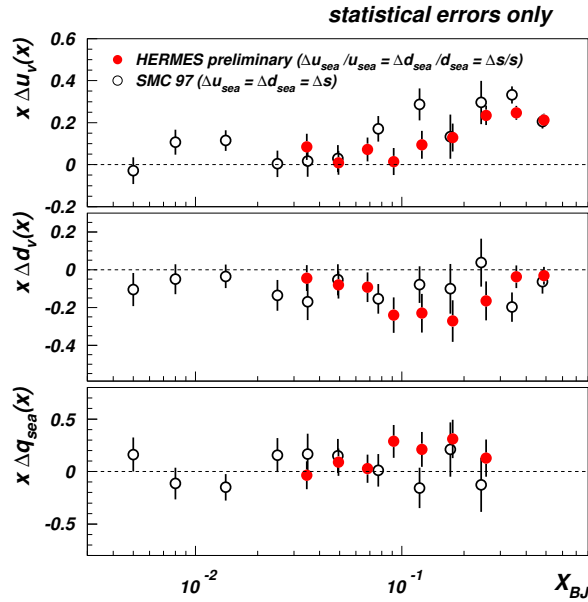


Figure 16: Data from SMC and HERMES for the valence (Δu_v and Δd_v) and sea ($\Delta \bar{q}$) spin densities versus x extracted from semi-inclusive asymmetry measurements. The dominant statistical errors only are shown.

Outlook: The analysis of polarised structure function data enables first measurements of the scaling violations to be performed. These provide a test of QCD and indicate that the gluon polarisation is positive. Similarly, the semi-inclusive measurements give first constraints on the sea. The structure function data from E155 and semi-inclusive data from HERMES will soon provide further input. These data are, however, insufficient to determine the various spin parton distributions within the nucleon. By analogy with Table 1, we can therefore consider a future programme of spin structure measurements which will enable the partonic spin structure to be unravelled, as shown in Table 2. In the next few years HERMES, COMPASS and the RHIC experiments will focus on the determination of the gluon. It is also possible that the polarised proton technology developed at RHIC could be utilised at HERA in order to explore polarised structure functions at low (x, Q^2). With a high luminosity HERA machine the data would also extend to high Q^2 where neutral current and charged current events would provide detailed information on this spin structure.

Table 2: Processes studied in global spin parton distribution fits. The first group of datasets correspond to current experiments. The second group correspond to near-future (year 2000) experiments. The third group correspond to potential year 2005 experiments at HERA. (Courtesy of T. Gehrmann.)

Process/ Experiment	Leading order subprocess	Parton behaviour probed
DIS ($\ell N \rightarrow \ell X$) $g_1^{\ell p}, g_1^{\ell d}, g_1^{\ell n}$ (SLAC, EMC/SMC, HERMES) $\ell p, \ell n \rightarrow \ell \pi X$ (SMC, HERMES)	$\gamma^* q \rightarrow q$ $\gamma^* q \rightarrow q$ with $q = u, d, \bar{u}, \bar{d}$	Two structure functions \rightarrow $\sum_q e_q^2 (\Delta q + \Delta \bar{q})$ $\Delta A_3 = \Delta u + \Delta \bar{u} - \Delta d - \Delta \bar{d}$ $\Delta u_v, \Delta d_v, \Delta \bar{q}$
$\ell N \rightarrow c \bar{c} X$ (COMPASS, HERMES) $\ell N \rightarrow h^+ h^- X$ (COMPASS) $pp \rightarrow (\gamma^*, W^\pm, Z^0) X$ (RHIC) $pp \rightarrow \text{jets } X$ (RHIC) $pp \rightarrow \gamma X$ (RHIC)	$\gamma g \rightarrow c \bar{c}$ $\gamma g \rightarrow q \bar{q}$ $\gamma q \rightarrow qg$ $q \bar{q} \rightarrow \gamma^*, W^\pm, Z^0$ $q \bar{q}, qq, qg, gg \rightarrow 2j$ $qg \rightarrow q\gamma$ $q \bar{q} \rightarrow g\gamma$	Δg ($x \approx 0.15, 0.3$) Δg ($x \approx 0.1$) $\Delta u, \Delta \bar{u}, \Delta d, \Delta \bar{d}$ ($x \gtrsim 0.06$) Δg (?) ($x \gtrsim 0.03$) Δg ($x \gtrsim 0.03$)
DIS ($e^\pm p \rightarrow \nu X$) g_1^\pm, g_5^\pm (HERA) DIS (small x) g_1^{ep} (HERA) $\ell N \rightarrow \ell \text{jets } X$ (HERA) $pp \rightarrow \ell^+ \ell^- X$ (HERA- \vec{N})	$W^* q \rightarrow q'$ $\gamma^* q \rightarrow q$ $\gamma^* g \rightarrow q \bar{q}$ $\gamma^* q \rightarrow qg$ $q \bar{q} \rightarrow \gamma^*$	Two structure functions \rightarrow $\Delta u - \Delta \bar{d} - \Delta \bar{s}$ $\Delta d + \Delta s - \Delta \bar{u}$ $\alpha_{q,g}$ ($\Delta \bar{q} \sim x^{\alpha_q}, \Delta g \sim x^{\alpha_g}$) Δg ($x \gtrsim 0.0015$) $\Delta \bar{q}$ ($x \gtrsim 0.15$)

4 HERA Results

The HERA ep collider has improved its performance in successive years, providing large e^+p datasets from 1994-97 running. During this period 27.5 GeV positrons collided with 820 GeV protons resulting in data samples of 37pb^{-1} and 46pb^{-1} for H1 and ZEUS, respectively. As a measure of the progress which has been made in the study of the scaling violations of F_2 ,

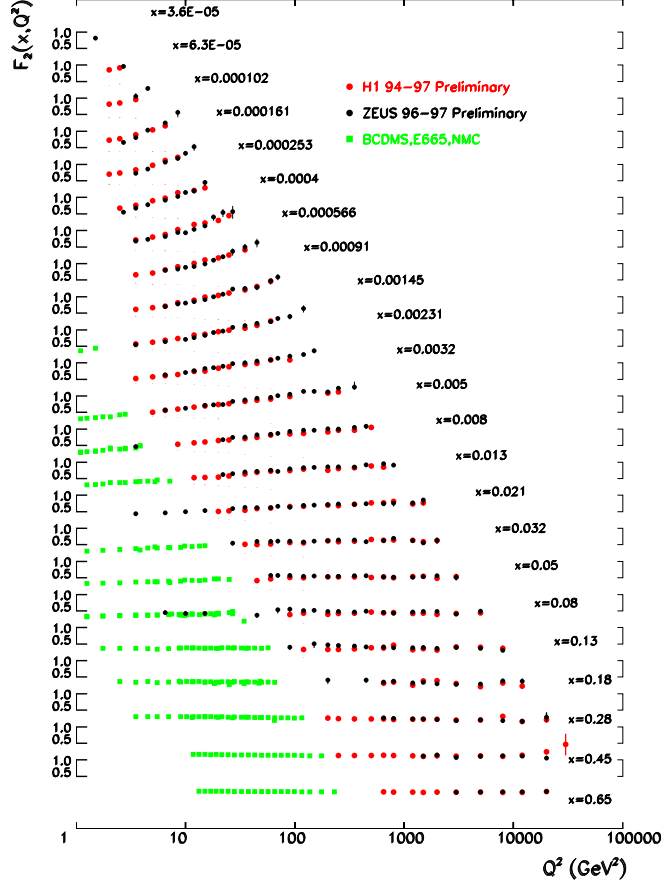


Figure 17: Scaling violations of F_2 versus Q^2 for various x ranges from the latest H1 and ZEUS preliminary data compared to fixed-target experiments. (The quoted x values correspond to the ZEUS measurements or the nearest x values from other experiments).

Fig. 17 illustrates how the latest HERA data, presented for the first time at ICHEP98, extend the reach in Q^2 beyond 10,000 GeV^2 with x extending up to 0.65. At high Q^2 values, the effects of Z^0 exchange are significant and the value of F_2^{em} is quoted where

$$F_2 = F_2^{em} + \frac{Q^2}{Q^2 + M_Z^2} F_2^{int} + \left(\frac{Q^2}{Q^2 + M_Z^2} \right)^2 F_2^{wk}$$

where F_2^{em} , F_2^{int} and F_2^{wk} are the contributions due to photon exchange, γZ interference and Z exchange, respectively. The data also extend to very low x below 10^{-5} : here it should be noted that the precision of the low- $x \lesssim 0.03$ data is now comparable to that of the fixed-target data at higher x . There is a region of overlap where the HERA and fixed-target experiments can be compared. In particular, the analysis of the ZEUS results at low y may resolve the CCFR-NMC discrepancy discussed earlier in the context of the “5/18ths rule”. However, this comparison (not shown) is currently inconclusive, with the ZEUS data lying between the NMC and CCFR data.

4.1 Low- Q^2 Results

Transition Region: The rise of F_2 with decreasing x or, equivalently, the rise of $\sigma_{\gamma^*p}^{tot}$ with increasing W has stimulated significant experimental and theoretical developments in the understanding of QCD at high energies. One challenge is to explore how and where the transition occurs from soft to hard physics and interpret low- Q^2 data. Measurements have been performed using dedicated low-angle taggers (e.g. the ZEUS BPC) and shifted vertex (SVX) data [40] as well as QED Initial State Radiation (ISR) data [41] in order to map out this region. In Fig. 18, a compilation of the latest measurements available from HERA and E665 indicates that the different experiments and techniques agree with a precision of around 5% from the most recent data. The significant rise of F_2 is apparent for $Q^2 \gtrsim 1 \text{ GeV}^2$, a behaviour which is described by the ZEUS NLO (pQCD) fit. This behaviour is not reproduced in the DL (Donnachie-Landshoff Regge) fit. The ZEUS collaboration has performed both types of fits to the F_2 data exploring

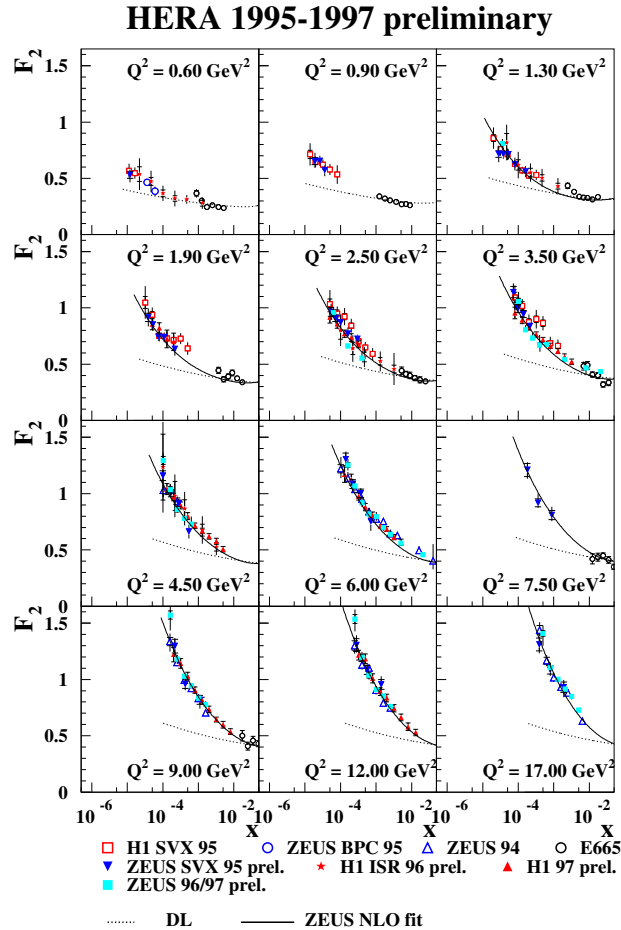


Figure 18: HERA F_2 data for various Q^2 intervals as a function of x exploring the transition region. The data are compared to the Donnachie-Landshoff Regge model (lower dotted line) and the ZEUS NLO QCD fit (full line) discussed in the text.

this transition region [40]. In order to determine the relationship between low- Q^2 ZEUS BPC data measured in the range $0.1 < Q^2 < 0.65 \text{ GeV}^2$ and $Q^2 = 0 \text{ GeV}^2$ data, a Generalised Vector Meson Dominance (GVMD) approach can be taken. GVMD relates the virtual-photon

cross-section to the real cross-section via

$$\sigma_{\gamma^*p}^{tot} = \sigma_{\gamma p}^{tot} \cdot \frac{M_0^2}{Q^2 + M_0^2}$$

for fixed W and $\sigma_L = 0$. A good description of the data is found with $M_0^2 = 0.53 \pm 0.04 \pm 0.10 \text{ GeV}^2$. Regge theory then determines the W dependence of the data, combined with lower energy photoproduction experiments, as

$$\sigma_{tot}^{\gamma p}(W^2) = A_R(W^2)^{\alpha_R-1} + A_P(W^2)^{\alpha_P-1}$$

where the Reggeon intercept α_R is fixed to 0.5 from hadroproduction data and lower energy photoproduction data also constrain A_P , A_R and α_P . From the BPC data alone, the pomeron intercept value is

$$\alpha_P^{BPC} = 1.141 \pm 0.020(stat.) \pm 0.044(sys.)$$

to be compared with the Donnachie-Landshoff value $\alpha_P = 1.08$. In this Q^2 range, the rise of the cross-section is therefore relatively modest. Combining the GVMD and Regge approaches, the resulting ZEUSREGGE fit is used to parameterise the Q^2 and W dependence of the low $Q^2 < 1 \text{ GeV}^2$ data. The ZEUS NLO QCD fit to the ZEUS 94 and ZEUS SVX data, incorporating NMC and BCDMS data, (discussed below) is used to determine the behaviour and the uncertainties on the gluon and singlet quark densities at low x for $Q^2 > 1 \text{ GeV}^2$.

ZEUS 1995

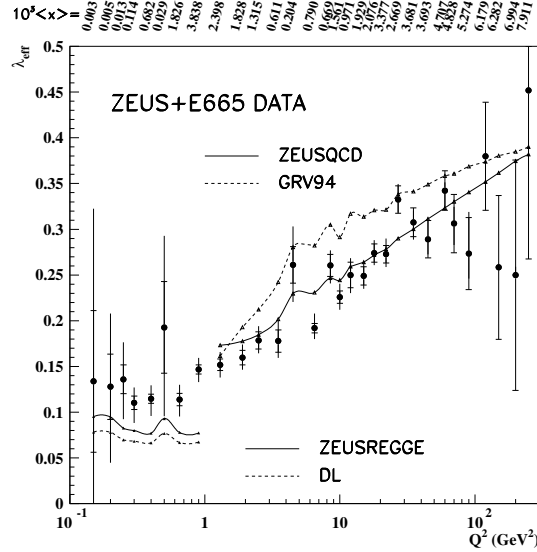


Figure 19: λ_{eff} versus Q^2 and $\langle x \rangle$ from fits to ZEUS and E665 data of the form $F_2 = c \cdot x^{-\lambda_{\text{eff}}} |_{Q^2}$. The data are compared to the QCD and Regge fits discussed in the text.

To quantify the behaviour of F_2 , fits to the E665 and ZEUS data of the form $F_2 = c \cdot x^{-\lambda_{\text{eff}}} |_{Q^2}$ are performed. The parameter $\lambda_{\text{eff}} \simeq \alpha_P - 1$ for $x < 0.01$ is then plotted as a function of Q^2 in Fig. 19. A relatively slow transition from $\lambda_{\text{eff}} \simeq 0.1$ is observed with increasing Q^2 . Also shown are fits to the DL and ZEUSREGGE parameterisations, fitted over the same x range as

ZEUS 1995

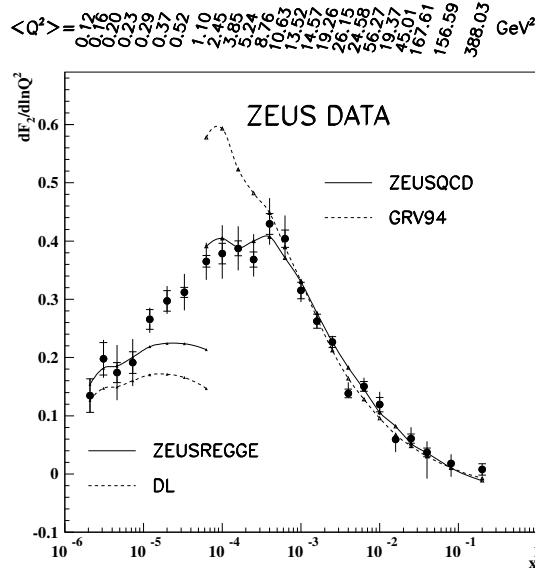


Figure 20: $dF_2/d\ln Q^2$ versus x and $\langle Q^2 \rangle$ from fits to ZEUS data of the form $F_2 = a + b \cdot \ln(Q^2)|_x$. The data are compared to the QCD and Regge fits discussed in the text.

the data, for $Q^2 < 1 \text{ GeV}^2$. These describe the data reasonably but are systematically lower. For $Q^2 > 1 \text{ GeV}^2$, the data are compared to the GRV94 prediction where the starting scale for the evolution of the parton densities is rather low ($\sim 0.3 \text{ GeV}^2$) and pQCD evolution generates the rise at small x : this approach is observed to reasonably describe the data and the description is improved using the GRV98 PDF (not shown) [7]. The rise at small x is also described by the ZEUSQCD fit, where the ZEUS data is used as an input.

This rise of F_2 with decreasing x is intimately coupled to the scaling violations via the gluon density (in leading order $dF_2/d\ln Q^2 \sim xg(x)$ neglecting sea quark contributions). In Fig. 20, fits of the form $F_2 = a + b \cdot \ln(Q^2)|_x$ have been performed to the ZEUS data and the parameterisations discussed above. For $x \sim 2 \cdot 10^{-4}$, corresponding to $\langle Q^2 \rangle \sim 4 \text{ GeV}^2$ there is a qualitative change in behaviour where the scaling violations stabilise and then decrease for lower- x values, a behaviour which is not reproduced by the GRV94 PDF. The question is whether this scaling violation behaviour and the slow onset of the rise of F_2 with decreasing x can be simultaneously understood.

A. Mueller has discussed the scaling violation behaviour in terms of a geometric model where the spatial extent, R_0 , of the $q\bar{q}$ fluctuation of the virtual photon in the γ^*p fixed-target frame is related to the height of the plateau in the scaling violations [42]

$$\left. \frac{dF_2}{d\ln Q^2} \right|_x \simeq \frac{Q^2(\pi R_0^2)}{4\pi\alpha}.$$

For $\left. \frac{dF_2}{d\ln Q^2} \right|_x \simeq 0.4 \text{ GeV}^{-2}$ and $Q^2 \simeq 4 \text{ GeV}^2$, the spatial extent $R_0 \simeq 0.3 \text{ fm}$. This appears to be the scale at which a transition takes place and the partons in the proton start to overlap [3]. However, perturbative QCD is pushed to its limit and it will be important to test that the parton densities extracted from F_2 can be universally applied.

The ZEUS NLO fit to the $Q^2 > 1 \text{ GeV}^2$ data describes the data, demonstrating that there is sufficient flexibility in such an approach to go down to relatively low Q^2 . However, the relatively stable scaling violations observed around $\langle Q^2 \rangle \sim 4 \text{ GeV}^2$ in Fig. 20 yield a gluon contribution which is rapidly diminishing at small- x and which is in fact smaller than the singlet sea quark contribution for small starting scales. For larger Q^2 values the gluon dominates the sea and we have an intuitively appealing picture where gluons radiate sea quarks whereas, in this low- Q^2 region, the sea appears to be driving the gluon at low x . Whether such low- Q^2 partons are universally valid could be tested using e.g. low- Q^2 diffractive vector meson data ([42] and review by M.Erdmann).

An important part of the ZEUS NLO QCD fit is the determination of the uncertainties on the gluon and singlet quark densities. These are given for the gluon distribution in Fig. 21. The overall uncertainty is estimated by combining in quadrature: the experimental systematic uncertainties on the ZEUS as well as the NMC and BCDMS data; the theoretical uncertainties on $\alpha_s(M_Z^2)$ by ± 0.005 , the relative strange quark content by $\pm 50\%$ and the charm mass by $\pm 0.2 \text{ GeV}$; and, the parameterisation uncertainties on the starting scale, by varying $1 < Q_0^2 < 7 \text{ GeV}^2$, as well as using a more flexible form of the input in terms of Chebycheff polynomials and redefining the χ^2 including *stat.* \oplus *sys.* errors. These variations correspond to a precision on the gluon of $\sim 10\%$ at $Q^2 = 20 \text{ GeV}^2$ where the renormalisation and factorisation scales are set to $\mu_R^2 = \mu_F^2 = Q^2$. The role of the scale uncertainties is discussed in [43] with respect to future capabilities to determine $\alpha_s(M_Z^2)$ at HERA. The theoretical and parameterisation uncertainties are amplified at low Q^2 such that the gluon is rather poorly determined from the scaling violations of F_2 in the transition region discussed above.⁴ It is clear, however, that the gluon is significantly suppressed at low Q^2 .

F₂^c Determination: $D^* \rightarrow (K\pi)\pi_s$ measurements in DIS provide a significant test of the gluon density of the proton determined from the scaling violations of F_2 . They also help to constrain theoretical uncertainties in the fits to F_2 where different prescriptions for charm production are adopted. The ZEUS preliminary cross-section $\sigma^{ep \rightarrow D^* X} = 8.55 \pm 0.31_{-0.50}^{+0.30} \text{ nb}$ is measured in the range $1 < Q^2 < 600 \text{ GeV}^2$, $0.02 < y < 0.7$, $1.5 < p_T^{D^*} < 15 \text{ GeV}$, and $|\eta^{D^*}| < 1.5$. In general, the H1 [44] and ZEUS [45] data agree with the Harris-Smith NLO calculations [46] where the fraction $f(c \rightarrow D^{*+}) = 0.222 \pm 0.014 \pm 0.014$ is determined from LEP data [47], the Peterson fragmentation function is characterised by $\epsilon_c = 0.035$ and the renormalisation and factorisation scales are set to $\mu_R^2 = \mu_F^2 = Q^2 + 4m_c^2$. There is, however, a small discrepancy at lower x_{D^*} and higher η^{D^*} , corresponding to the proton direction, where the data lie above the prediction. A similar discrepancy is also observed in the first analysis in the semi-leptonic decay channel [45]. Together these results indicate that the fragmentation of charm in ep processes is worthy of further investigation. At this stage, it is reasonable to extrapolate the measured cross-section to the full $\{\eta, p_T\}$ range⁵ to determine $F_2^c(x, Q^2)$ via the expression

$$\frac{d^2 \sigma_{c\bar{c}X}}{dx dQ^2} = \frac{2\pi\alpha^2}{xQ^4} [Y_+ F_2^c(x, Q^2) - y^2 F_L^c(x, Q^2)]$$

where the F_L^c contribution can be estimated as a QCD correction. In Fig. 22, the HERA $F_2^c(x, Q^2)$ data mirror the rise of F_2 at small x . The data are in agreement with the GRV94

⁴ The gluon can even become negative at low Q^2 (in $\overline{\text{MS}}$ scheme) but the physical quantities, F_2 , F_2^c and F_L remain positive within the quoted errors.

⁵This procedure neglects the possibility of additional contributions outside the measured region due, for example, to intrinsic charm.

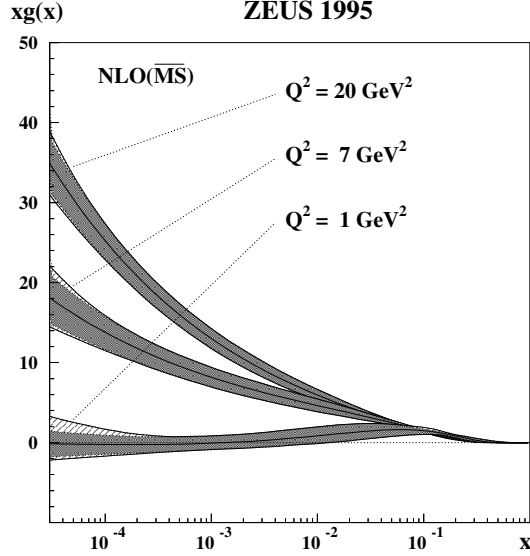


Figure 21: Gluon momentum distribution, $xg(x)$ at $Q^2 = 1, 7$ and 20 GeV^2 in $\overline{\text{MS}}$ scheme including the uncertainties discussed in the text. The shaded band corresponds to the experimental and theoretical uncertainties and the hatched band indicates the parameterisation errors discussed in the text.

PDF, where the band represents an estimated theoretical uncertainty due to the effective charm mass ($m_c = 1.4 \pm 0.2 \text{ GeV}$). This comparison verifies the steep rise of the gluon density at low x with a precision of $\simeq 15 - 20\%$.

F_L Determination: The contribution of F_L enters as a QCD correction to the total DIS cross-section where $F_L = F_2 - 2xF_1$. As such it provides an additional method to calibrate the gluon at low x . H1 [41] have used two methods to extract F_L from the reduced cross-section $\tilde{\sigma} = F_2 - \frac{y^2}{Y_+} \cdot F_L$ at high y . This is the region where the scattered electron energy is low: in the H1 analysis scattered positrons are measured down to $E_{e'} > 3 \text{ GeV}$ and backgrounds reduced by requiring the associated track to have correct charge. F_L is determined as a function of $Q^2 \geq 3 \text{ GeV}^2$ by measuring local derivatives of $\partial\tilde{\sigma}/\partial \log y$ and observing deviations from a straight line at high y . These data are denoted by the stars in Fig. 23. Here, the data are compared to an earlier extrapolation method [48] applied to the same data, which yields consistent results, as well as to the H1 NLO QCD fit to H1, NMC and BCDMS F_2 data. The data are in agreement with the QCD expectations although there is an indication of a relatively large F_L contribution at the highest y (corresponding to lowest x) values. In conclusion, a consistent value for the gluon density at low $x \lesssim 10^{-2}$ may be extracted from the data on F_2 , F_2^c and F_L with a precision of $\sim 10\%$ at $Q^2 = 20 \text{ GeV}^2$.

4.2 High- Q^2 Cross-Sections

The HERA collider provides a unique window to explore ep interactions at the highest energies, extending the range of momentum transfer Q^2 by about two orders of magnitude compared to fixed-target experiments. As the HERA luminosity increases we explore the region of $Q^2 \sim$

HERA 95-97 PRELIMINARY

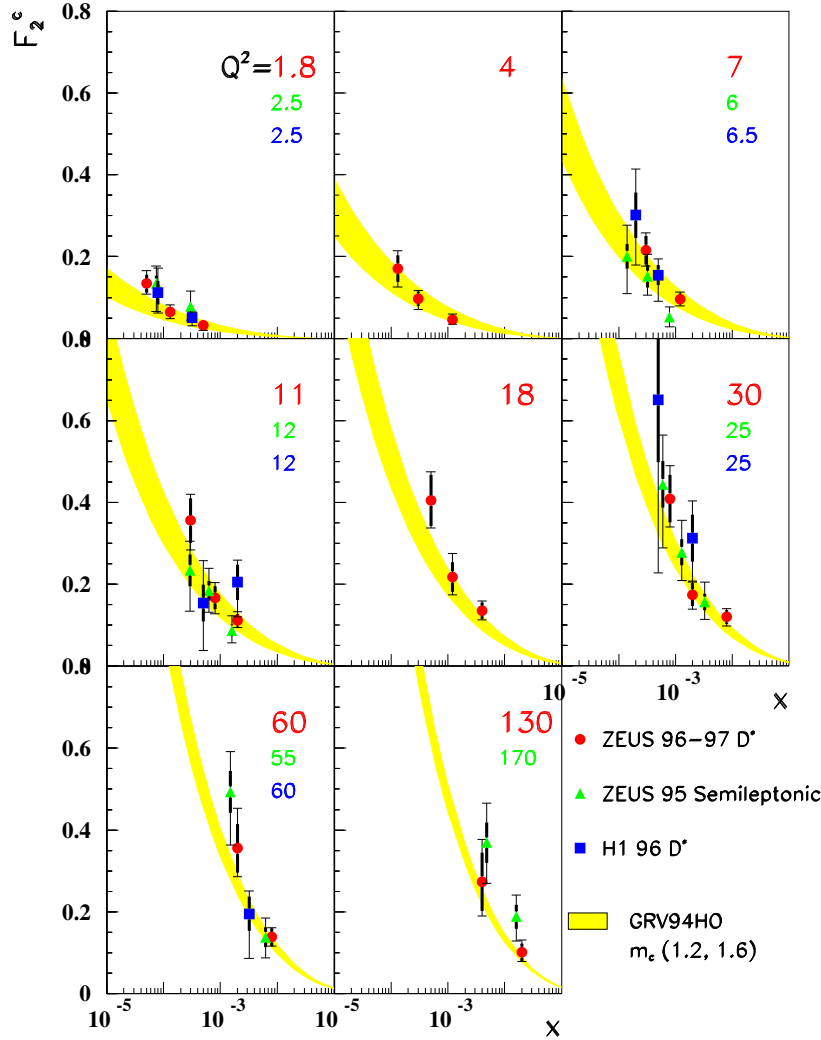


Figure 22: HERA F_2^c data for various Q^2 intervals as a function of x . The data are compared to the Harris-Smith NLO QCD calculation using the GRV94 PDF input discussed in the text.

10^4 GeV^2 , where electroweak effects play a rôle. It is in this unexplored kinematic region that we are sensitive to deviations from the standard model (SM).

In 1997, H1 [49] and ZEUS [50] reported an excess of events compared to the SM predictions from the neutral current (NC) data taken during 1994 to 1996. For the H1 analysis an accumulation of 7 events in a reconstructed e^+q mass window of $200 \pm 12 \text{ GeV}$ was found, compared to an expectation of 0.95 ± 0.18 from 15 pb^{-1} of data. One further event was found from the 1997 data corresponding to a further 22 pb^{-1} , yielding 8 events compared to an expectation of 3.01 ± 0.54 . For the ZEUS analysis the observed rates agreed with expectations except for an excess at the highest Q^2 where two outstanding events with $Q^2 \simeq 40,000 \text{ GeV}^2$ were observed from a luminosity of 20 pb^{-1} . These events still clearly stand out but no new NC outstanding events are observed in the 1997 data, corresponding to a further 26.5 pb^{-1} . Similarly in the charged current (CC) channel, the number of events is higher than expectations but is consistent with the standard model. Attention has therefore focussed on measuring the cross-sections at

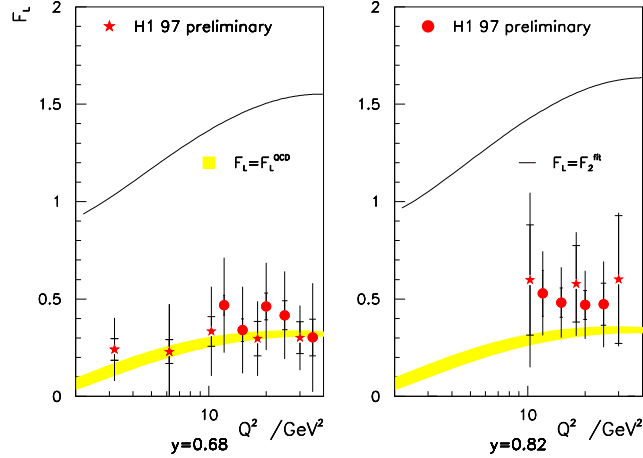


Figure 23: H1 determination of F_L versus Q^2 for $y = 0.68$ and $y = 0.82$ using the derivative method (\star) compared to the published method (\bullet) and the NLO QCD fit expectation (shaded band). The upper limit $F_L = F_2$ is indicated by the full line.

the highest accessible Q^2 values.

The theoretical uncertainty on the cross-sections was determined as discussed w.r.t. the ZEUS low- Q^2 NLO QCD fit using high- x F_2^p and F_2^n data to yield SM cross-section uncertainties of $\simeq 6$ -8% on the NC cross-section and $\simeq 6$ -12% on the CC cross-section at the highest accessible Q^2 values. These cross-sections therefore represent a benchmark for the standard model. The cross-sections, discussed below, are corrected to the electroweak Born level and integrated over the measured range of y for H1 [51] and corrected to the complete y range for ZEUS [52].

Neutral Current Cross-Sections: High- Q^2 neutral current events are easily identified from the high-energy scattered positron. The cross-section is particularly sensitive to the valence u -quark distribution in the proton

$$\frac{d^2\sigma_{e+p}}{dx dQ^2} \simeq \frac{2\pi\alpha^2}{xQ^4} [Y_+ F_2(x, Q^2) - Y_- xF_3(x, Q^2)].$$

Here, F_2 is the generalised structure function, incorporating γ and Z terms, which is sensitive to the singlet sum of the quark distributions ($xq + x\bar{q}$) and xF_3 is the parity-violating (Z -contribution) term which is sensitive to the non-singlet difference of the quark distributions ($xq - x\bar{q}$). The data are now becoming sensitive to electroweak γZ interference effects, which suppress the NC cross-section by $\sim 30\%$ for $Q^2 > 10,000 \text{ GeV}^2$ [51, 52].

In the upper plot of Fig. 24, the H1 cross-section is observed to fall over more than six orders of magnitude. The ratio of the data to the SM, adopting the H1 NLO QCD fit, is shown in the lower plot of Fig. 24 where agreement is observed up to $Q^2 \simeq 30,000 \text{ GeV}^2$. Comparison of the the data uncertainties with those from theory (not shown) indicates that the data will constrain the parton densities of the proton at large x .

Charged Current Cross-Sections: Charged current events are identified by their missing transverse momentum (p_T) due to the escaping neutrino. The cross-section is sensitive to the valence

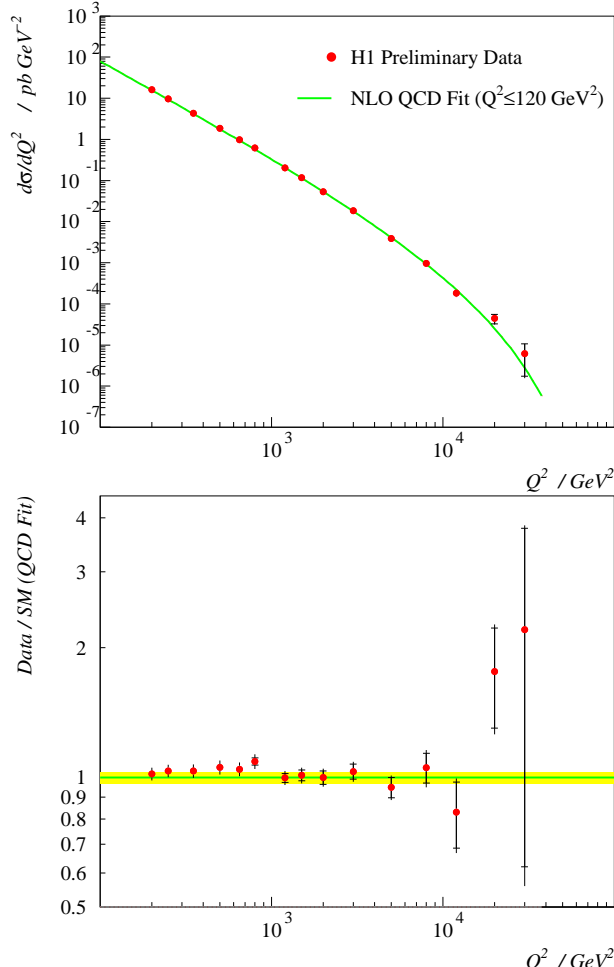


Figure 24: H1 neutral current cross-section $d\sigma^{NC}/dQ^2$ versus Q^2 for $y < 0.9$ and $E_{e'} > 11$ GeV (upper plot) and ratio with respect to the standard model prediction (lower plot). The shaded band represents the luminosity uncertainty of $\pm 2.6\%$.

d -quark distribution in the proton

$$\frac{d^2\sigma_{e+p}}{dx dQ^2} \simeq \frac{G_F^2}{2\pi} \left(\frac{M_W^2}{Q^2 + M_W^2} \right)^2 [\bar{u} + \bar{c} + (1-y)^2(d+s)].$$

In the ZEUS analysis, $d\sigma^{CC}/dQ^2$ was measured for $Q^2 > 400$ GeV² using the Jacquet-Blondel method where $Q_{JB}^2 = p_T^2/(1-y_{JB})$, with an RMS resolution on $Q^2 \simeq 25\%$, reflecting the $35\%/\sqrt{E}$ hadronic energy resolution. The systematic uncertainties, mainly due to the hadronic energy scale uncertainty of $\pm 3\%$, correspond to $\sim 15\%$ uncertainties on the cross-section at lower Q^2 but increase at larger x and Q^2 .

In the upper plot of Fig. 25 the cross-section is observed to fall over more than four orders of magnitude. The ratio of the data to the SM, adopting the CTEQ4D PDF, is shown in the lower plot of Fig. 25 where good agreement is observed up to Q^2 of $\simeq 10,000$ GeV². Comparison of the the data uncertainties with those from theory (shaded band) indicates that the data will help to constrain the d -quark densities at large- x . The cross-section is suppressed relative to NC γ exchange due to the propagator term: this characteristic dependence on Q^2 has been fitted to

ZEUS Preliminary 1994-97

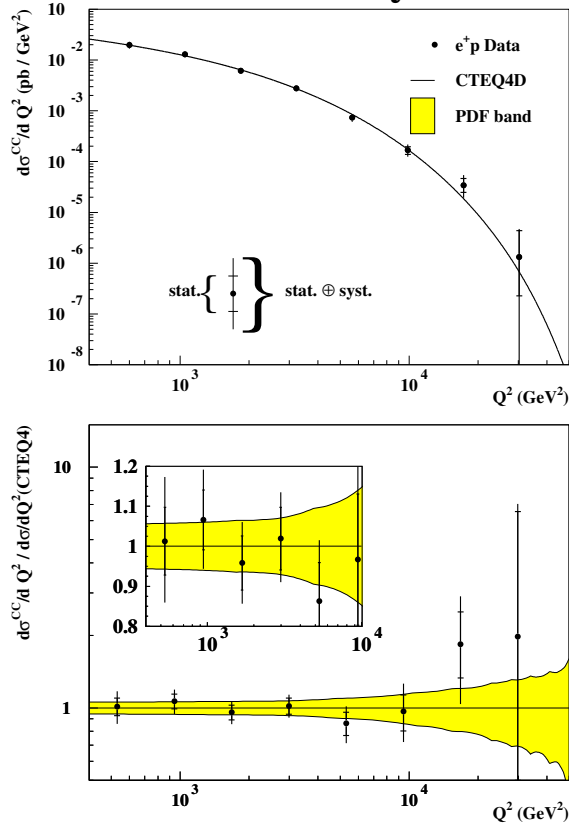


Figure 25: ZEUS charged current cross-section $d\sigma^{CC}/dQ^2$ versus Q^2 for $0 < y < 1$ (upper plot) and ratio with respect to the standard model prediction (lower plot). The shaded band in the ratio plot represents the ZEUS NLO QCD fit uncertainty.

yield a value for the mass of the exchanged (space-like) W -boson of

$$M_W = 78.6_{-2.4}^{+2.5}(\text{stat.})_{-3.0}^{+3.3}(\text{sys.}) \text{ GeV} \quad (\text{ZEUS prelim.})$$

$$M_W = 81.2 \pm 3.3(\text{stat.}) \pm 4.3(\text{sys.}) \text{ GeV} \quad (\text{H1 prelim.})$$

with an additional PDF uncertainty of ± 1.5 GeV estimated in the ZEUS analysis and an uncertainty of ± 3 GeV due to electroweak radiative corrections estimated in the H1 analysis.

Returning to the Bodek-Yang analysis [18], discussed in relation to the fixed-target results, the ZEUS CC cross-section is plotted as function of x for $Q^2 > 400 \text{ GeV}^2$ in Fig. 26. The increase in the ratio of d/u corresponds to an increase of the CC cross-section at high x . The uncertainties on the data are large in this region, but this modification does result in better agreement with the data than the standard PDF's at large x .

A comparison of the H1 and ZEUS NC and CC cross-sections for $Q^2 > 1000 \text{ GeV}^2$ is given in Fig. 27. The NC and CC data are in agreement and both cross-sections agree with the SM prediction over a broad range range of Q^2 . At high $Q^2 > 10,000 \text{ GeV}^2$, the CC cross-section is suppressed relative to the NC cross-section due to the d/u ratio being less than unity. The measurement of the HERA CC/NC ratio of cross-sections will therefore provide a direct determination of this ratio, free from the uncertainties due to nuclear binding effects.

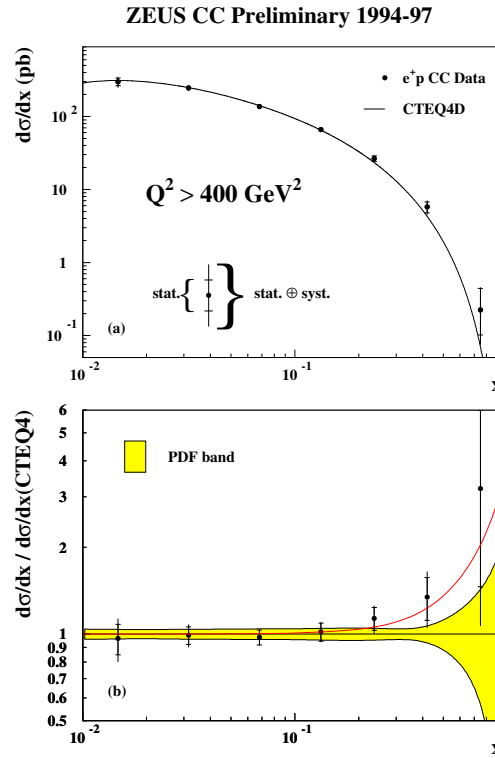


Figure 26: ZEUS charged current cross-section $d\sigma^{CC}/dx$ versus x for $Q^2 > 400 \text{ GeV}^2$ and ratio with respect to the standard model prediction (lower plot). The upper curve in the ratio plot represents the Bodek-Yang d/u modified MRS(R2) parameterisation discussed in the text.

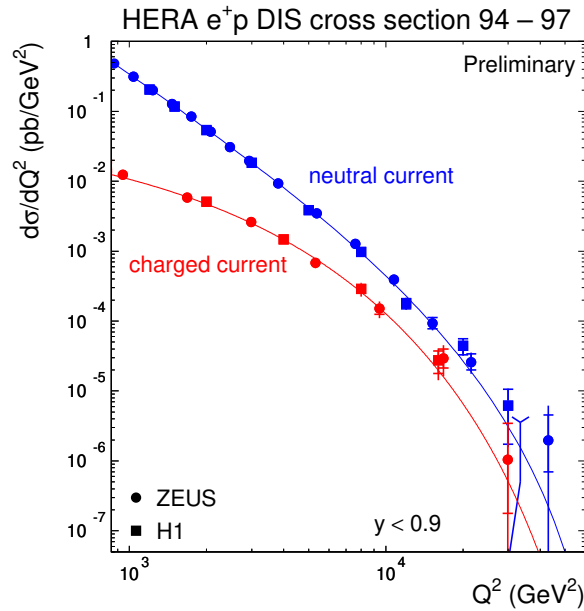


Figure 27: HERA e^+p DIS cross-sections neutral and charged current data for $y < 0.9$ compared to the standard model prediction, adopting the CTEQ4D PDF.

5 Summary and Outlook

There were many highlights in our deepening understanding of nucleon structure presented at the ICHEP98 conference. CCFR have performed final analyses of their structure function data which lead to precise tests of QCD. NuTeV already provide electroweak input and aim to reduce the uncertainty on $\alpha_s(M_Z^2)$ to ± 0.002 . Important developments have been made in the understanding of higher twist effects in terms of renormalon theory. Input from various experiments and a reassessment of the importance of nuclear binding effects in the deuteron lead to the conclusion that the ratio of d/u parton densities increases, whilst the ratio of \bar{d}/\bar{u} decreases compared to earlier determinations.

The second phase of spin experiments are now exploring spin structure via NLO QCD fits. The first observations of scaling violations from combined fits to the world data indicate that the source of the spin puzzle lies with the gluon spin density, Δg , although large uncertainties remain. Semi-inclusive measurements now provide input on the quark composition of the spin.

The first discovery at HERA was the rise of F_2 at low x . Precise data now enable the rise of the associated scaling violations with decreasing x and hence the gluon to be determined. The determinations of F_2^c and F_L enable this gluon distribution to be calibrated. The fall of these scaling violations at low (x, Q^2) enables the region where parton confinement effects take place to be explored at high energies.

The large e^+p data sample enables cross-sections to be measured at very large Q^2 where electroweak effects start to play a rôle. The HERA data are consistent with the Standard Model and place constraints on the parton densities at large x . The outlook is for a similar sample of $\sim 50\text{pb}^{-1}$ of e^-p data in the next two years, prior to the HERA upgrade where luminosities will be increased five-fold. Deep inelastic scattering has historically led to the discovery of the nucleus, quarks and electroweak neutral currents. The discovery potential of current and future experiments is high and the field continues to provide important input to our understanding of sub-nuclear structure.

Diffraction and Low- Q^2 Physics Including Two-Photon Physics

Martin Erdmann

Universität Karlsruhe, Engesserstr. 7, D-76128 Karlsruhe

E-mail: Martin.Erdmann@desy.de

Abstract

Recent experimental results on the partonic structure of the photon and on the color singlet exchange in strong interaction processes are reviewed. At the LEP e^+e^- and HERA ep colliders, complementary and consistent measurements have been achieved on the quark-gluon structure of quasi-real and virtual photons. At the HERA ep and Tevatron $\bar{p}p$ colliders, the quark-gluon configurations of the diffractive exchange is consistently found to have a large gluon component. The rate of diffractive interactions observed by the HERA and Tevatron experiments, however, is largely different and challenges explanation.

1 The Partonic Structure of the Photon

The motivation behind studying the structure of the photon results from the interest in understanding the formation of hadronic matter. Permitted by the Heisenberg uncertainty relation, the photon can fluctuate for some time into a quark–anti-quark state. This fluctuation can be disturbed, e.g., by an electron or proton probe which allows the density of quarks and gluons of the partonic state of the photon to be determined.

At the LEP e^+e^- and HERA ep colliders, photons are emitted by the leptons which gives access to the partonic structure of almost real photons [53] as well as highly virtual photons. The measurements to obtain information on the partonic state of the photons discussed here are

1. the photon structure function from deep inelastic electron–photon scattering (Fig. 28),
2. jet and particle cross sections (e.g. Fig. 29), and
3. the total photon–photon cross section.

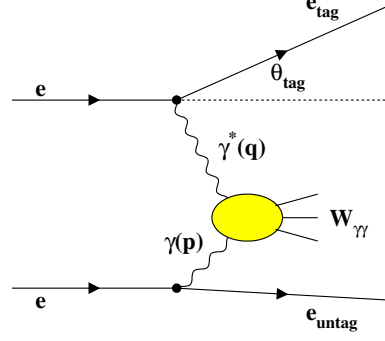


Figure 28: Feynman diagram of deep inelastic electron–photon scattering: the partonic structure of the quasi-real photon from the untagged lepton is probed by the virtual photon from the tagged electron.

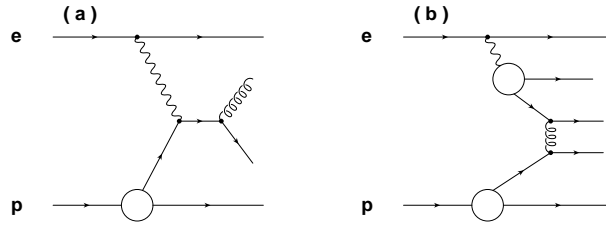


Figure 29: Examples of Feynman diagrams for photoproduction of jets in ep collisions in leading order QCD: a) direct photon–proton process, b) resolved photon–proton process.

1.1 Measurements Related to the Quark Distributions of Quasi-Real Photons

New F_2^γ structure function measurements have been performed in the interesting region of small parton momenta $x \sim 10^{-2}$ by the L3 collaboration [54]. F_2^γ is determined from the measurement of the double differential inclusive cross section

$$\frac{d^2\sigma}{dx dQ^2} = \frac{2\pi\alpha^2}{xQ^4} (1 + (1-y)^2) F_2^\gamma(x, Q^2), \quad (1)$$

where α is the electro-magnetic coupling constant, Q^2 denotes the virtuality of the probing photon and gives the resolution scale of the process, and y is the inelasticity $y = Q^2/(xs_{e\gamma})$. In Fig. 30, the x dependence of F_2^γ is shown in two bins of Q^2 .

A major challenge in this analysis is the determination of x : since the lepton that emitted the target photon remains undetected, the energy of the target has to be determined from the hadronic final state. Using a new improved reconstruction method for x , two results for F_2^γ are presented by the L3 collaboration using two different Monte Carlo generators for the correction of detector effects (Phojet [55], Twogam [56]). These two data sets demonstrate that over a large region in x the structure function result does not depend on the details of simulating the hadronic final state. Only below $x \sim 10^{-2}$ this limitation becomes sizable.

In the same figure, previous results of the OPAL collaboration are shown [57]. Within the errors, good agreement is observed between the two experiments. Also shown are different

parameterizations of the quark density in the photon demonstrating that the data give new information on the quark distributions at low x (LAC [58], GRV [59], SaS [60]). Scaling violations caused by gluon emission off the quark before the scattering process occurs results in a rise of F_2^γ below a small value of x . The data are not yet precise enough to confirm or reject such a rise at $x \sim 10^{-2}$.

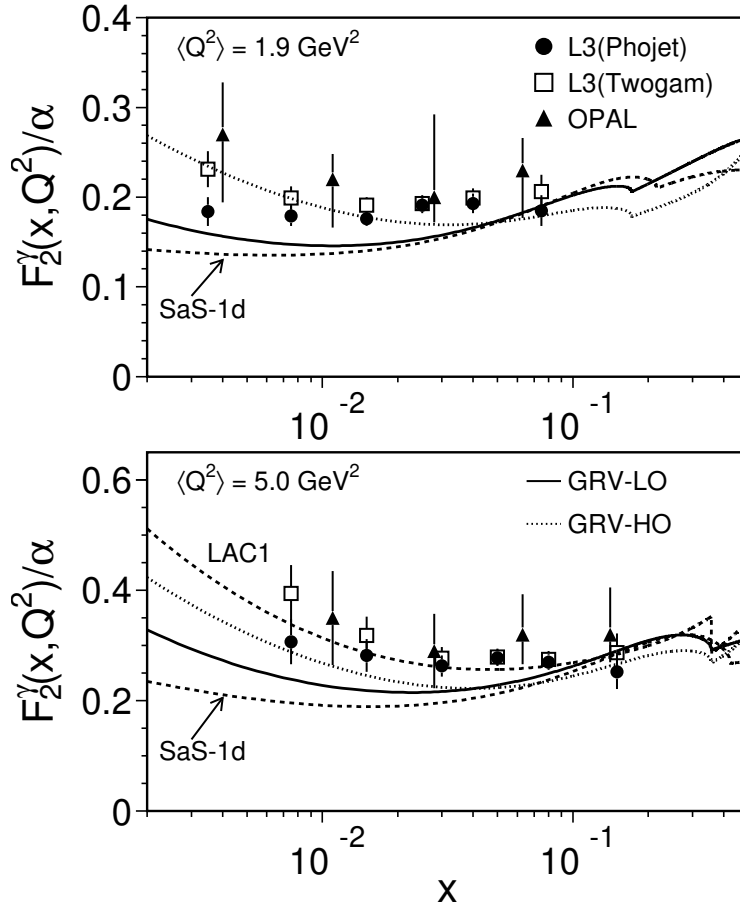


Figure 30: The photon structure function F_2^γ , measured in two-photon collision at LEP, is shown as a function of the parton fractional momentum x in two bins of the virtuality Q^2 of the probing photon. The squared symbols and the circles represent the measurements of the L3 experiment using two different Monte Carlo generators for correcting detector effects. For comparison, previous results of the OPAL experiment are shown (triangle symbols). The curves represent different parameterizations of the parton distributions in the photon.

In the momentum region around $x \sim 0.5$, where the quark and the anti-quark each carry half of the photon energy, results on the structure function F_2^γ exist from many experiments. A compilation of these measurements is shown in Fig. 31 as a function of the resolution scale Q^2 [61]. The data are compatible with an increasing quark density in the photon as Q^2 increases. This Q^2 dependence is very different from that of hadronic structure functions at large x and is expected by perturbative QCD (Fig. 32 and discussion in Section 2.2): the splitting of the photon into a quark-anti-quark pair gives rise to the probability $f_{q/\gamma}$ of finding a quark in the

photon to increase as

$$f_{q/\gamma} \sim \ln \frac{Q^2}{\Lambda_{QCD}^2} \quad (2)$$

in leading order.

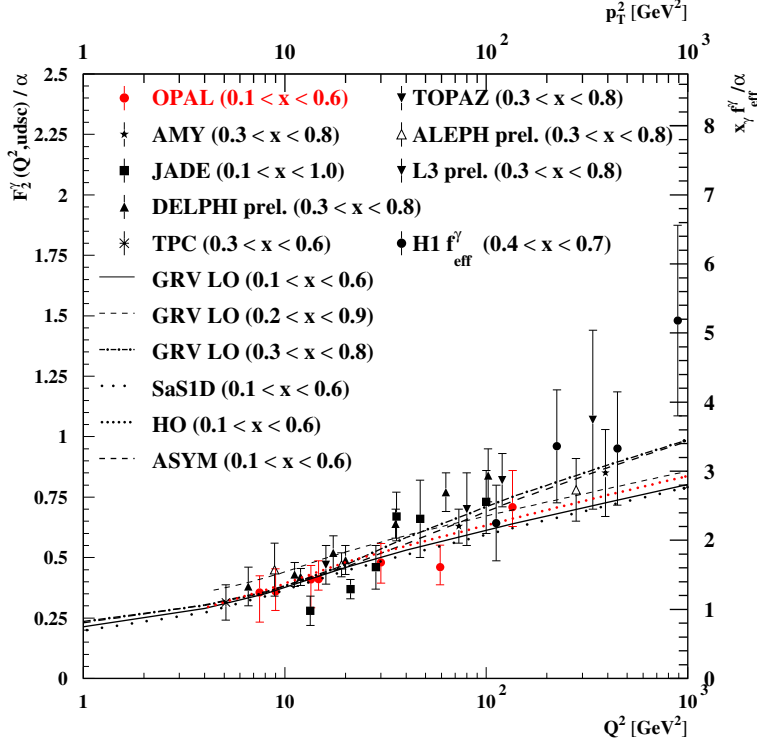


Figure 31: The structure function F_2 of the photon is shown as a function of the virtuality Q^2 of the probing photon for parton fractional momenta around $x \sim 0.5$. Measurements of the photon structure function F_2^γ from e^+e^- data are shown in comparison with an effective parton distribution extracted from photoproduction of di-jets in ep collisions (H1 data). The curves represent different parameterizations of the parton distributions of the photon.

In the same figure an effective parton distribution $x\tilde{f}_\gamma$ of the photon is shown which has been extracted from di-jet measurements in photon–proton collisions by the H1 collaboration [62]. This effective parton distribution combines the quark and the gluon densities of the photon with a weight of color factors [63]:

$$x\tilde{f}_\gamma = x (f_{q/\gamma} + \frac{9}{4} f_{g/\gamma}) . \quad (3)$$

The vertical scale for $x\tilde{f}_\gamma$ on the right side of Fig.31 has been adjusted relative to the F_2^γ scale, since in contrast to the F_2^γ measurements the jet processes are independent of the electric charges of the quarks. The relevant resolution scale is the transverse momentum p_t^2 of the scattered partons which is here taken to have the same resolution power as Q^2 . The results of the di-jet measurements are in good agreement with the F_2^γ data. The jet data probe the partons of the photon at large resolution scales and compete well in precision with the F_2^γ measurements.

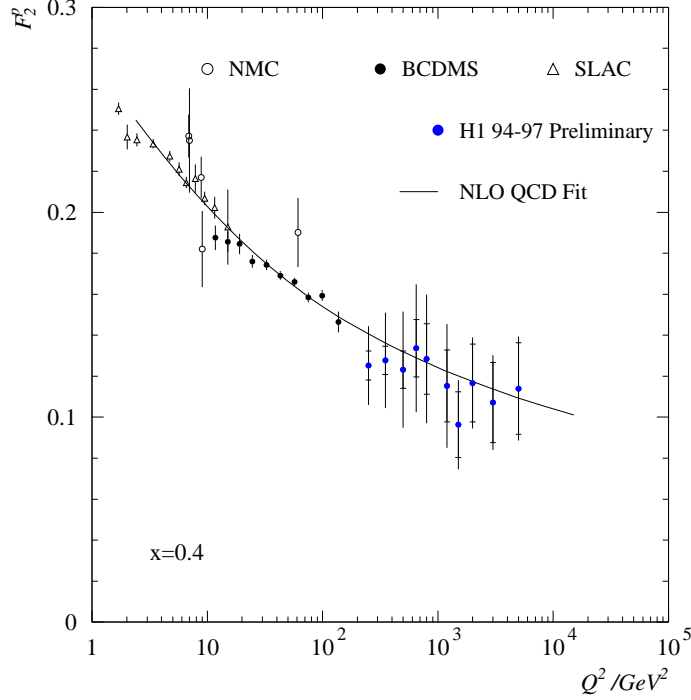


Figure 32: The structure function F_2 of the proton is shown as a function of the virtuality Q^2 of the probing photon for the parton fractional momentum $x = 0.4$ from fixed target data and preliminary H1 data.

The quark density close to the kinematic limit $x \sim 1$ is analysed in photoproduction of two jets. Here the contributions of the direct and resolved photon–proton processes need to be understood (Fig. 29). They differ in their matrix elements and therefore in the distribution of the parton scattering angle θ^* .

In Fig. 33, a new di-jet cross section measurement of the ZEUS collaboration is shown differentially in $|\cos \theta^*|$ for large di-jet masses and correspondingly large x [64]. Also shown are next-to-leading order QCD calculations [65] using two different parton parameterizations of the photon (GRV [59], GS [66]). The direct photon contribution (not shown in the figure) is not sufficient to describe the measured jet cross section either in shape or in the absolute normalization. Contributions of resolved photon processes are required to describe the data which are sufficiently precise to discriminate different parton parameterizations of the photon at large x .

1.2 Measurements Related to the Gluon Distribution of Quasi-Real Photons

New measurements of the inclusive charm production cross section at the large LEP beam energies are shown in Fig. 34 by the L3 collaboration [67]. The cross section has been determined using semi-leptonic charm decays in the electron and muon channels. In the same figure, next-to-leading order QCD calculations [68] using two different charm masses and the GRV parameterization [59] of the parton distributions in the photons are shown. The dominant

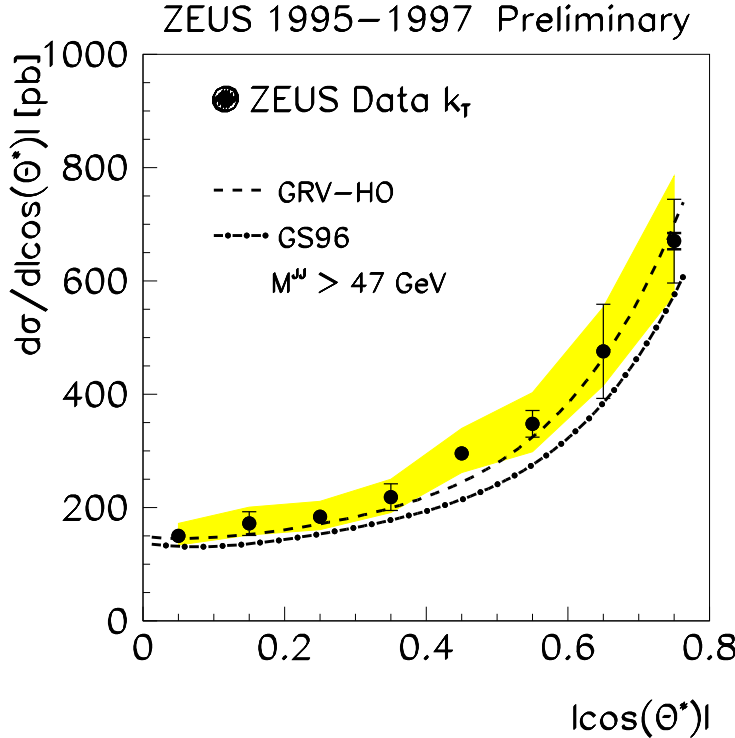


Figure 33: The di-jet cross section in ep collisions involving quasi-real photons is shown differentially in terms of the cosine of the parton scattering angle at large di-jet mass above 47 GeV from ZEUS data. The curves represent next-to-leading QCD calculations using different parton distributions of the photon.

contribution to the cross section results from gluon induced processes with an average gluon momentum as small as $\langle x \rangle \sim 0.03$ [69].

Also di-jet data are used to access the low- x gluon distributions of the photon. In Fig. 35, a new measurement of the di-jet cross section is shown as a function of the parton momentum x by the H1 collaboration [70]. The histograms represent a leading-order QCD calculation [55] showing the contributions of the direct photon-proton interactions and quark and gluon induced processes using the GRV parton parameterizations for the photon and the proton.

Both the charm and di-jet measurements give compatible conclusions on the low- x gluon density of the photon and are precise to the level of 30%.

New information on the gluon distribution of the photon results from di-jet production in photon-photon collisions which has been measured by the OPAL collaboration [71]. In Fig. 36, the cross section is shown differentially in the transverse jet energy E_t^{jet} . At sufficiently large E_t^{jet} the measurement can well be described by a next-to-leading order QCD calculation [72] using the parton distribution function of GRV [59].

In Fig. 37, the di-jet cross sections are shown differentially in the jet rapidity $|\eta^{jet}|$. The data explore different regions of the parton fractional momentum $x > 0.8$, $x < 0.8$ with a precision of $\sim 20\%$. They are compared to leading order QCD calculations (Phojet [55], Pythia [73]) and discriminate different parameterizations of the gluon distributions of the photon (LAC [58], GRV [59], SaS [60]).

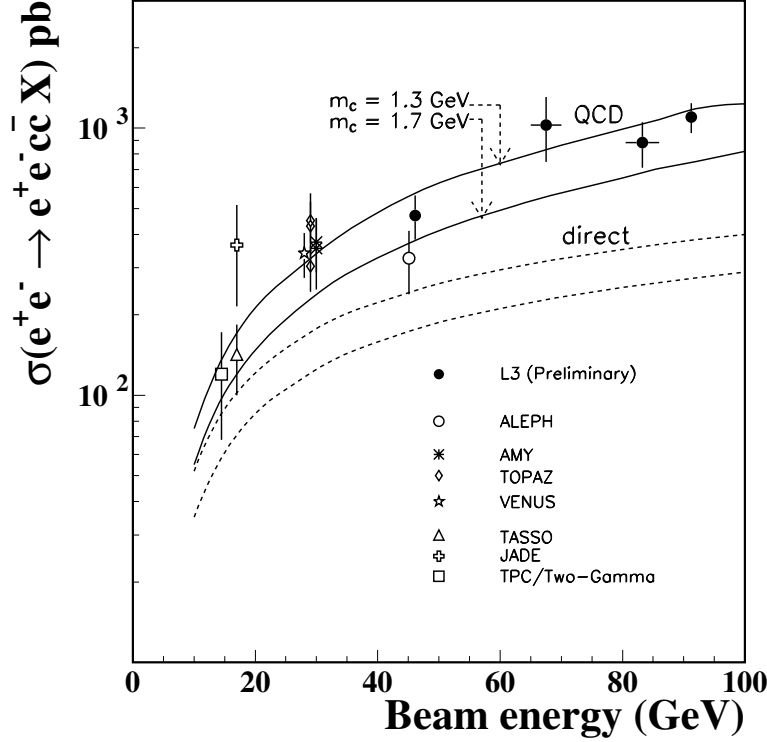


Figure 34: Measurements of the total charm production cross sections from two-photon collisions are shown as a function of the lepton beam energy (L3 experiment). The full curves represent next-to-leading QCD calculations using the GRV parton distribution functions of the photon and different values for the charm mass. The direct photon contribution is shown separately (dashed curves).

1.3 Parton Distributions of Virtual Photons

The fluctuation of a virtual photon into a quark-anti-quark pair is suppressed by the photon virtuality Q^2 . In comparison with real photons one therefore expects a smaller probability of finding the virtual photon in a partonic state. Also, there is less time to develop from the $q\bar{q}$ pair a vector meson bound state such that the hadronic contributions to the virtual photon structure should be small.

In Fig. 38, the first triple-differential di-jet cross section is shown as a function of the photon virtuality Q^2 in two bins of the parton momentum x for a fixed resolution scale $(E_t^{jet})^2 = 50 \text{ GeV}^2$ [74]. The cross section measurement at $x \sim 1$ (Fig. 38b) is well described by a leading order QCD calculation using the direct photon-proton interaction processes only (dashed curve [75]). At $x \sim 0.5$ (Fig. 38a) the absolute cross section is found to be smaller compared to the measurement at $x \sim 1$ as expected from the short fluctuation time of the photon. Here the direct photon contributions are not sufficient to describe the data at small $Q^2 \sim 2 \text{ GeV}^2$: the di-jet process is able to resolve the partonic structure of the virtual photon. As Q^2 approaches the squared transverse energy of the jets of $(E_t^{jet})^2 = 50 \text{ GeV}^2$, the resolution power of the di-jet process becomes insufficient for detecting the fluctuations of the virtual photons.

In analogy to the real photon case, eq. (3), an effective parton distribution for virtual photons $x\tilde{f}_{\gamma^*} = x(f_{q/\gamma^*} + 9/4f_{g/\gamma^*})$ has been extracted from the data and is shown in Fig. 39a in the

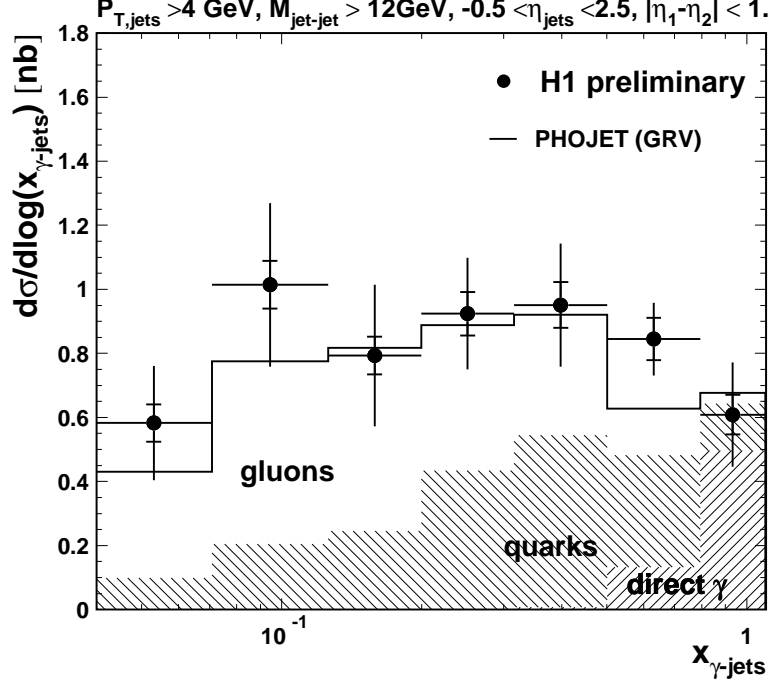


Figure 35: Photoproduction of di-jets in ep collisions is shown as a function of the parton fractional momentum x from H1 data. The cross section measurement is compared to a leading-order QCD calculation showing above the quark and direct photon contributions the gluon component of the photon at small x (the histograms are calculated using the GRV parameterizations of the partons in the photon).

interval $0 \leq Q^2 \leq 80 \text{ GeV}^2$ for $x = 0.6$ and $(E_t^{jet})^2 = 85 \text{ GeV}^2$. The partonic structure of the virtual photon is only slowly suppressed with the photon virtuality Q^2 . Such a dependence is predicted by perturbative QCD: in the region of $\Lambda_{QCD}^2 < Q^2 < (E_t^{jet})^2$ the probability of finding a quark in the virtual photon decreases logarithmically as Q^2 approaches the jet resolution scale:

$$f_{q/\gamma^*} \sim \ln \frac{(E_t^{jet})^2}{Q^2}. \quad (4)$$

The formation of a hadronic bound state from the $q\bar{q}$ pair of the photon can be studied with the production of ρ mesons. In Fig. 39b, the Q^2 dependence of the ρ cross section is shown which exhibits a fast decrease proportional to $(Q^2 + M_\rho^2)^{-n}$ with $n = 2.24 \pm 0.09$ [76]. As expected from the short photon fluctuation time into a quark-anti-quark pair, the probability to develop a hadronic bound state from the quark-anti-quark pair is highly suppressed. At sufficiently large Q^2 , the partonic structure of the virtual photon can therefore be predicted by perturbative QCD. In Fig. 39a, the full curve represents a QCD inspired model of the effective parton distribution of the virtual photon (SaS1d [77]) which is in agreement with the measurement within the experimental errors.

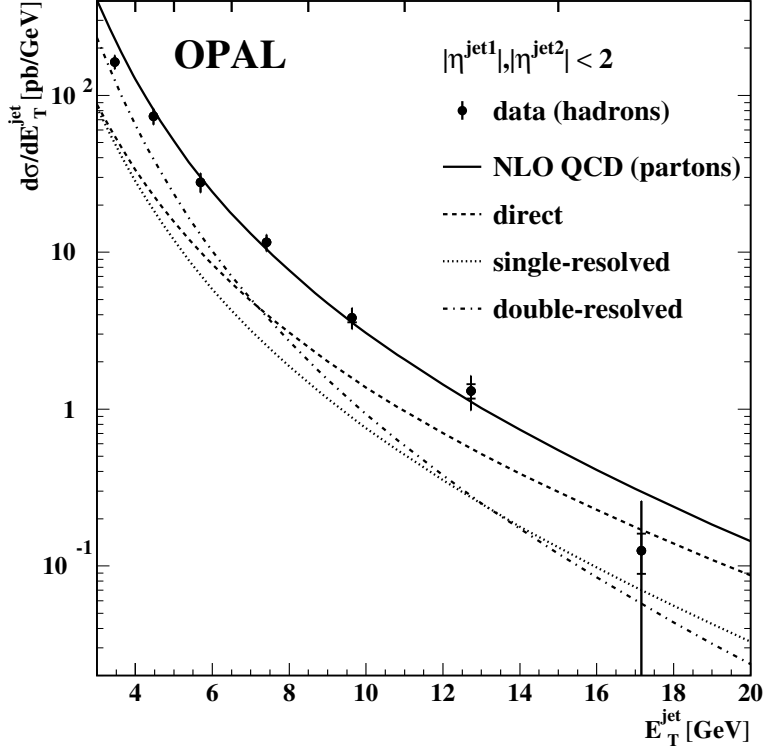


Figure 36: The di-jet cross sections from two-photon processes in e^+e^- collisions is shown as a function of the transverse jet energy from OPAL data. The curves represent next-to-leading QCD calculations of the different photon contributions using the GRV parton distribution functions of the photon. The labels refer to direct photon-photon interactions via quark exchange (direct), processes where one photon interacts directly with a parton of the other photon (single resolved) and processes which involve partons of both photons (double resolved).

1.4 Total Photon-Photon Cross Section

The total photon-photon cross section $\sigma_{\gamma\gamma}$ is dominated by soft scattering processes in which the photons develop a hadronic structure before the interaction occurs. A major challenge of this measurement is the understanding of the different contributions, the elastic, diffractive and non-diffractive processes. The visibility of the first two contributions in the detectors is small and requires reliable Monte Carlo generator calculations.

Progress has recently been made by the L3 experiment which succeeded in collecting a few hundred events of exclusive four pion production which contains contributions of elastic double- ρ production at center of mass energies below 10 GeV (Fig. 40) [78]. These data test the two generator calculations shown (Phojet [55], Pythia [73]).

A new measurement of the total photon-photon cross section is shown in Fig. 41 using the two different Monte Carlo generators (L3 collaboration [78, 79]). The data show a rise above $W \equiv \sqrt{s_{\gamma\gamma}} = 10$ GeV and are compatible within errors with the preliminary measurement of the OPAL collaboration [80]. This observed rise can be described by a power law $s_{\gamma\gamma}^\epsilon$ with $\epsilon = 0.158 \pm 0.006 \pm 0.028$ [78]. The rise has the tendency to be stronger than expected from soft Pomeron exchange which successfully describes all hadron-hadron and photon-proton total cross sections with $\epsilon = 0.095 \pm 0.002$ [81].

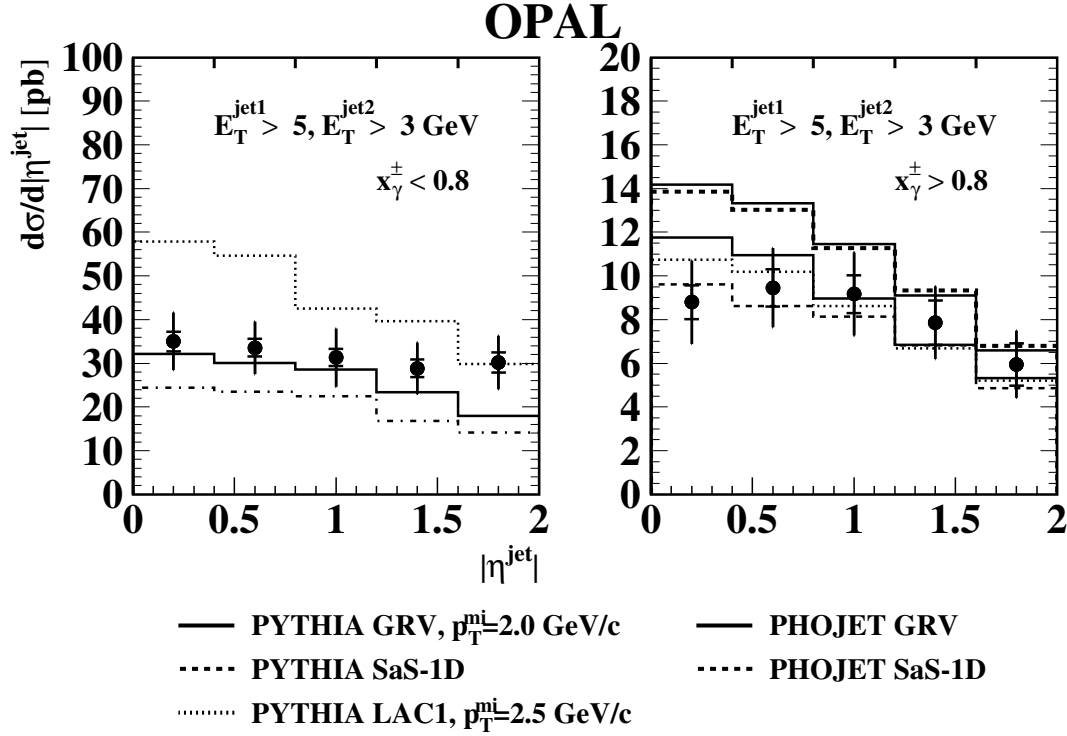


Figure 37: The di-jet cross sections from two-photon processes in e^+e^- collisions is shown differentially in terms of the jet pseudo-rapidity in two bins of the reconstructed parton fractional momentum x of the photon (OPAL experiment). The histograms represent leading order QCD calculations of two Monte Carlo generators using different parton distribution functions for the photon.

1.5 Summary 1: Photon

Improved knowledge on the partonic structure of real photons results from

- new structure function F_2^γ measurements at low parton fractional momenta $x \sim 10^{-2}$,
- di-jet cross section measurements at x values down to $\sim 10^{-2}$ and high $x \rightarrow 1$ in photon-proton and photon-photon interactions, and
- charm production in photon-photon processes at low $x \sim 10^{-2}$.

For the first time the partonic structure of highly virtual photons $Q^2 > 1$ GeV² has been investigated in ep collisions. The fluctuations of the virtual photon into a quark-anti-quark pair is only slowly suppressed with Q^2 and is compatible with a logarithmic decrease as predicted by perturbative QCD.

The understanding of the total photon-photon cross section has improved by the detection of elastic ρ production.

Overall, the results on the photon obtained in e^+e^- and ep collisions complement each other and are well compatible. The precision of the measurements remains a challenge for the next few years in order to be well prepared for the linear collider.

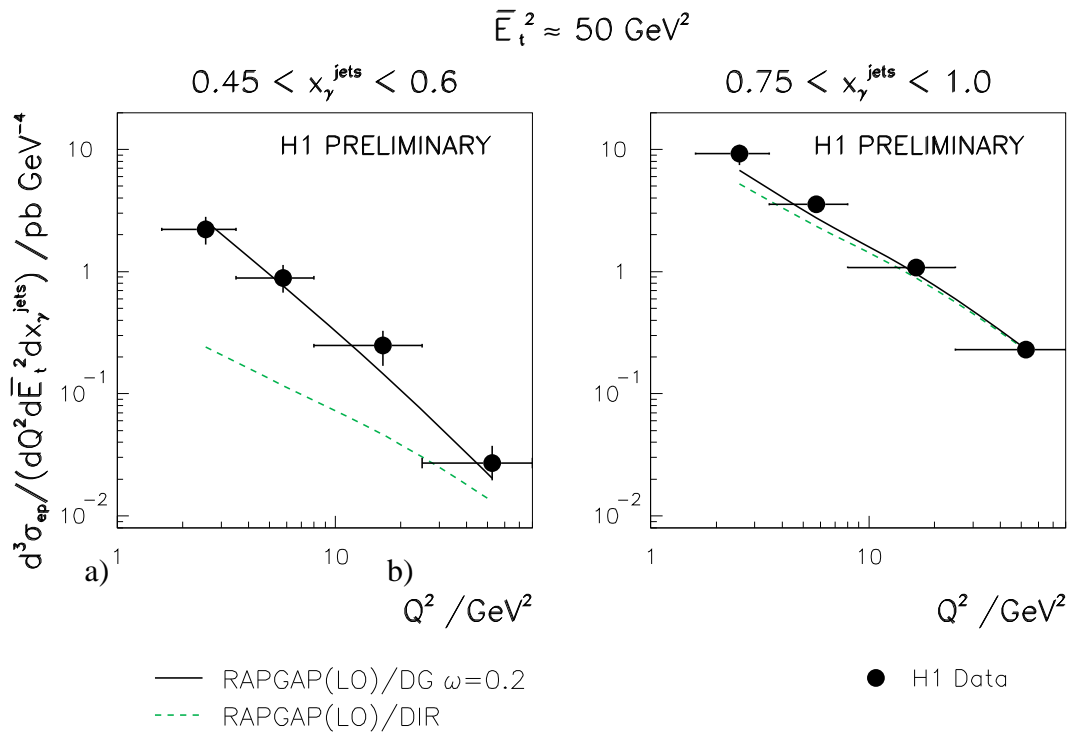


Figure 38: The triple differential di-jet cross section from ep collisions is shown as a function of the photon virtuality Q^2 for two bins of the fractional momentum x of the parton from the photon at fixed transverse jet energy E_t^{jet} (H1 experiment). The full curve is a leading order QCD calculation including the direct photon–proton interactions (dashed curve) and resolved photon processes, the latter reflecting the partonic structure of the virtual photon.

2 Colour Singlet Exchange

A sizable fraction of strong interaction processes includes the exchange of colour singlet objects. At the HERA ep and Tevatron $\bar{p}p$ colliders, these objects are emitted by the hadrons and may involve the exchange of quantum numbers (meson exchange) or may not (diffractive processes).

A handle on the type of the interaction process is given, e.g., by the observation of a fast baryon in the proton beam direction. Detection of energetic neutrons indicate that isospin-1 exchanges are present, in particular charged pion exchange. Protons are sensitive to both isoscalar and isovector exchanges.

Where the leading proton is close to the beam energy, diffractive scattering is expected to be dominant. Partonic scattering processes in such diffractive interactions give access to quark-gluon configurations that are colour neutral but different from the well known hadrons.

The following measurements to obtain information on colour singlet exchange are discussed here:

1. the ep structure function with a tagged baryon (Fig. 42),
2. the ep structure function of diffractive exchange (Figs. 42 ‘ \mathcal{P} ’ and 44),

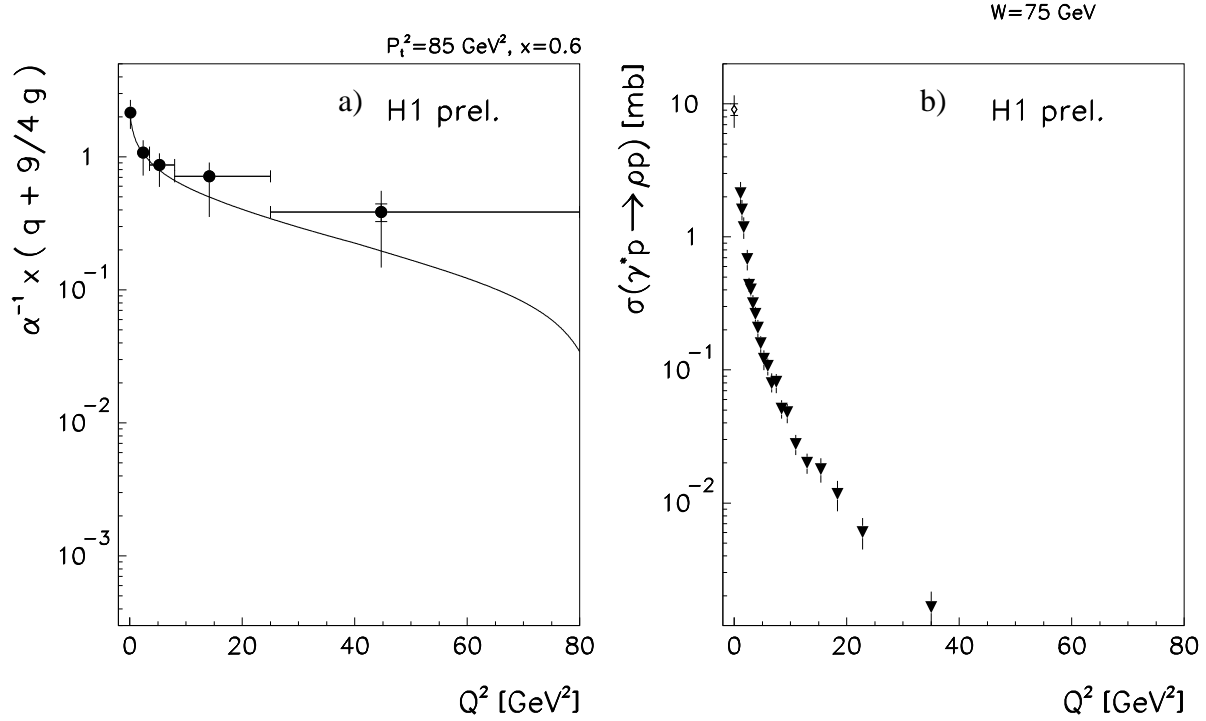


Figure 39: a) The effective parton distribution of virtual photons is shown as a function of the photon virtuality Q^2 for fixed parton fractional momentum $x = 0.6$ and scattered parton squared transverse momentum $p_t^2 = 85 \text{ GeV}^2$ (H1 experiment). The curve represents the SaS1d parameterization of the photon effective parton distribution. b) The ρ meson cross section is shown as a function of the photon virtuality Q^2 for the photon-proton center of mass energy $W = 75 \text{ GeV}$.

3. di-jet and W-boson production in diffractive $\bar{p}p$ scattering (Fig. 49), and
4. vector meson production in ep interactions (Fig. 55).

2.1 Tagged Baryon Production in ep Collisions

The production of protons and neutrons is studied in both the H1 and ZEUS experiments. A hadron calorimeter detects neutrons scattered at zero angle with respect to the proton direction. A series of Roman pot stations between the beam magnets serves as a proton spectrometer.

In Fig. 43, new measurements of the structure function from ep collisions with a tagged baryon $F_2^{\text{LB}(3)}$ are shown as a function of the baryon fractional energy $z = E_{lb}/E_p$ for fixed photon virtuality $Q^2 = 4.4 \text{ GeV}^2$ and parton fractional momentum $x_{Bj} = 10^{-3}$ (H1 collaboration [82]). $F_2^{\text{LB}(3)}$ was determined from cross section measurements which were integrated over the baryon transverse momenta in the range $0 \leq p_t \leq 0.2 \text{ GeV}$:

$$\frac{d^3\sigma}{dx_{Bj}dQ^2dz} = \frac{2\pi\alpha^2}{x_{Bj}Q^4} (1 + (1-y)^2) F_2^{\text{LB}(3)}(x_{Bj}, Q^2, z). \quad (5)$$

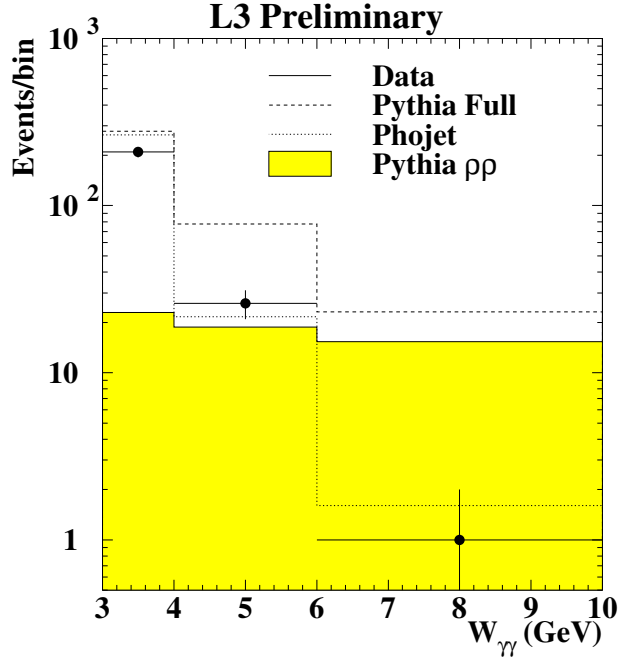


Figure 40: The number of events with exclusive four pion production from two-photon collisions in e^+e^- scattering is shown as a function of the photon–photon center of mass energy $W_{\gamma\gamma} \equiv \sqrt{s_{\gamma\gamma}}$ (L3 experiment). The data are compared with calculations of different Monte Carlo generators, showing the total four-pion production (histograms) and the exclusive production two ρ mesons (shaded histogram) separately.

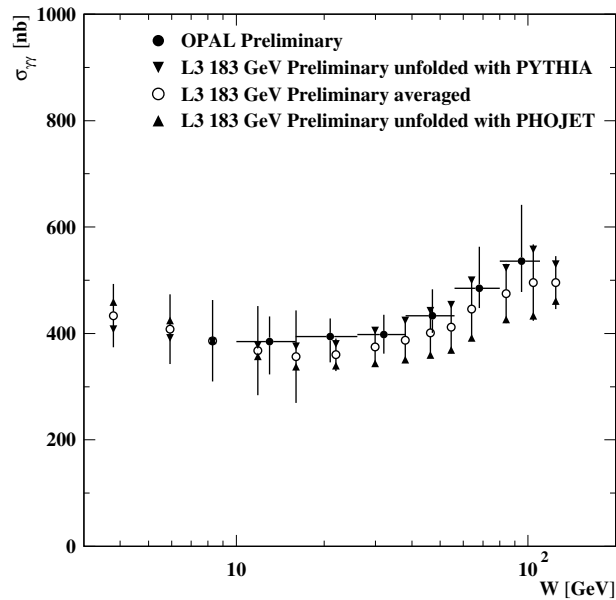


Figure 41: The total photon-photon cross section is shown as a function of the photon–photon center of mass energy $W_{\gamma\gamma} \equiv \sqrt{s_{\gamma\gamma}}$. The preliminary measurements of the L3 and OPAL experiments are compared using two different Monte Carlo generators for the detector corrections.

Here α is the electro-magnetic coupling constant and y denotes the inelasticity $y = Q^2/(x_{Bj}s_{ep})$.

The proton tagged structure function is found to be larger than that of the neutron tagged data. The curves are predictions of model calculations inspired by Regge phenomenology (Fig. 42). In this picture, the proton data cannot be explained by π^0 exchange alone, since from the $\pi^0 p$ and $\pi^+ n$ isospin 1/2 states one would expect the proton measurement to be a factor two below the neutron data. Instead, the proton data can be explained by an admixture of π^0 , Reggeon (f, ω) and Pomeron exchange. The neutron data can be explained by charged pion exchange alone and demonstrate the potential access to the pion structure function [83] in the new kinematic domain at small parton momenta around $x \sim 10^{-3}$.

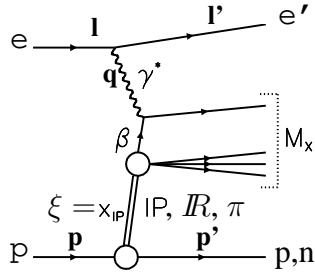


Figure 42: A Feynman diagram of deep inelastic electron–proton scattering with a tagged baryon is shown in the interpretation of colour singlet exchange.

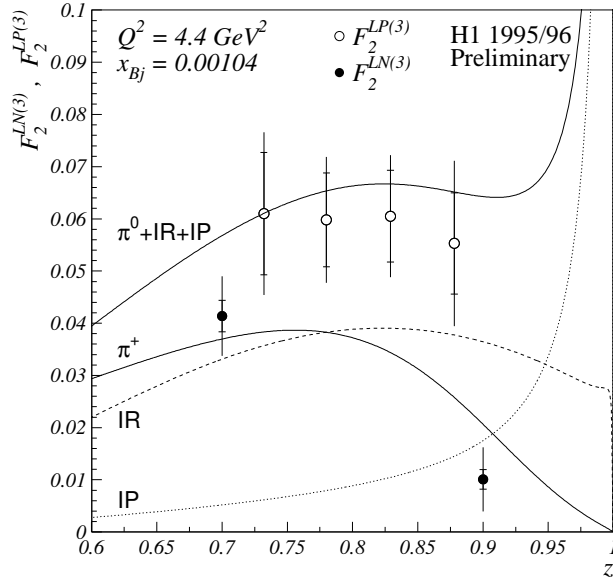


Figure 43: The ep structure functions $F_2^{LB(3)}$ with a tagged proton (open circle) or neutron (full circle) are shown as a function of the baryon fractional energy z at fixed photon virtuality $Q^2 = 4.4 \text{ GeV}^2$ and parton fractional momentum $x_{Bj} = 10^{-3}$ from H1 data. The curves represent the prediction of a Regge model.

Further information on the type of the interaction process comes from a new measurement of tagged baryons with the coincident formation of a large rapidity gap between the systems X and Y (Fig. 44) where Y may or may not be observed in the main detector (ZEUS collaboration

[84]). In Fig. 45, the rate of events with a large rapidity gap is shown as a function of the baryon fractional energy $x_L \equiv z = E_{lb}/E_p$. For $x_L \rightarrow 1$, the tagged proton production (full circle) is dominated by diffractive processes. For $x_L \ll 1$, the minimum gap size chosen for the analysis implies that $M_Y > M_p$. In this kinematic region, the rate of events with a large rapidity gap is small and shows that diffraction is not the main mechanism for the production of the baryons.

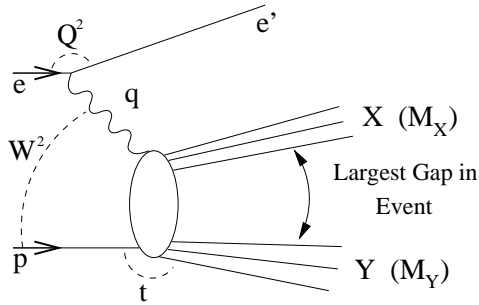


Figure 44: Feynman diagram of deep inelastic electron–proton scattering with a large rapidity gap.

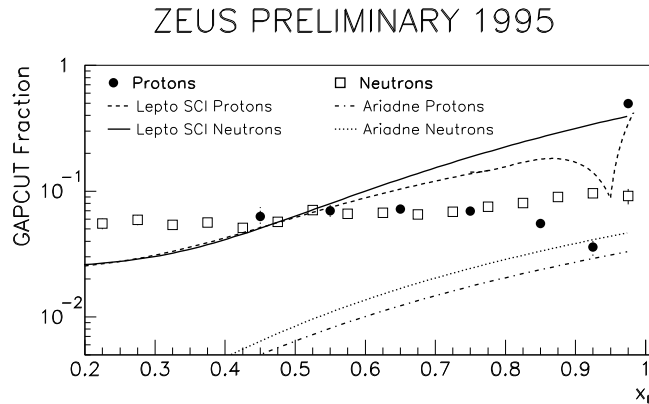


Figure 45: The rate of ep collisions with a tagged proton (full circle) or neutron (open square) with simultaneous formation of a rapidity gap is shown as a function of the baryon fractional energy x_L (ZEUS experiment). The curves show the predictions of different Monte Carlo generator calculations.

2.2 The Partonic Structure of Diffractive Exchange

Evidence for diffractive scattering processes in ep interactions can be obtained from different methods:

- A** tagging of highly energetic protons in the proton spectrometers (Section 2.1),
- B** from analysis of rapidity regions which are free of hadronic activity ('rapidity gap', Fig. 44),
or
- C** from the mass distribution of the hadronic final state which is observed in the main detector.

The ep Structure Function of Diffractive Exchange

The structure function $F_2^{D(4)}$ for diffractive exchange

$$\frac{d^4\sigma}{d\beta dQ^2 d\xi dt} = \frac{2\pi\alpha^2}{\beta Q^4} (1 + (1 - y)^2) F_2^{D(4)}(\beta, Q^2, \xi, t) \quad (6)$$

has been measured by the ZEUS collaboration using the tagged proton method A [85] as a function of the following four variables:

1. the virtuality Q^2 of the exchanged photon.
2. the squared four-momentum transfer $|t| = (p - p')^2$ from the proton side,
3. the momentum fraction $\xi = (Q^2 + M_X^2)/(Q^2 + s_{\gamma^*p})$ ($\xi \equiv x_P$), with M_X being the mass of the diffractive system observed in the main detector, and
4. the fractional momentum $\beta = x_{Bj}/\xi$.

When interpreting this process in terms of the exchange of a colour singlet object (Fig. 42), ξ gives the fractional momentum that this object takes from the proton, and β is the fractional momentum of the quark involved in the electron-quark scattering process. Therefore, this deep inelastic scattering measurement gives access to the partonic structure of diffractive color singlet exchange and provides information on the corresponding t distribution of this process. A new measurement of the t distribution is shown in Fig. 46 (ZEUS collaboration [84]).

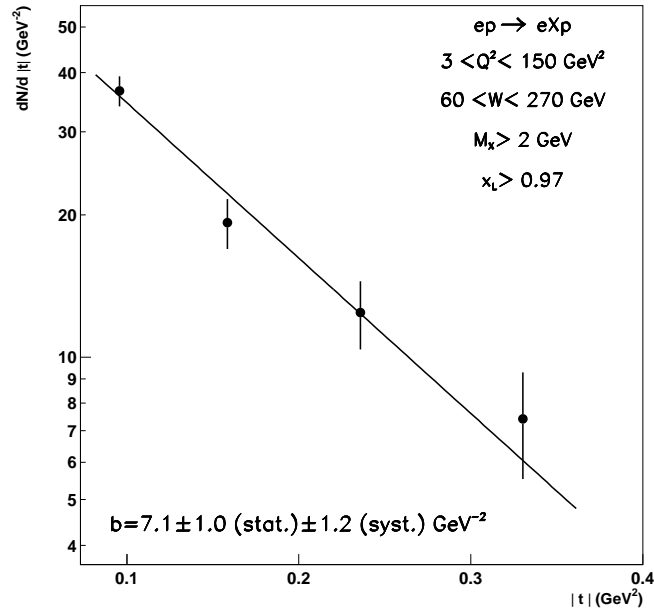


Figure 46: The distribution of the squared four-momentum transfer $|t|$ of diffractive ep processes is shown together with an exponential fit to the data (ZEUS experiment).

The methods B (Fig. 44) and C of measuring the deep inelastic scattering of diffractive exchange have to integrate over some t -range and can here take advantage of the knowledge of

the t distribution of the proton tagged data. The two methods also do not include the detection of proton remnant particles at small masses M_Y of the dissociated proton system and integrate over a small range of this mass (typically 1-4 GeV). Since the acceptance of proton-tagged events is at the percent level, the statistics using methods B,C are much larger by far.

In Fig. 47, a new triple differential structure function measurements $F_2^{D(3)}$ of the ZEUS collaboration (method C [86]) are compared with previous measurements by the H1 collaboration (method B [87]). The data are shown in a small selection of the large phase space covered as a function of the fractional momentum ξ , which the colour singlet object takes from the proton, in two bins of the parton momentum observable β and the photon virtuality Q^2 .

At small ξ , they are consistent in these and surrounding phase space bins with a power law ξ^{-n} and therefore are compatible with factorization of the ξ dependence. The measured value by the ZEUS collaboration [86] is $n - 1 = 0.253 \pm 0.017^{+0.077}_{-0.023}$ and is compatible with the result of the H1 collaboration [87]. The measured value of n is slightly larger than the value expected for soft Pomeron exchange in Regge inspired models ($n - 1 \sim 0.1$).

The β and Q^2 dependence of $F_2^{D(3)}$ at fixed small value of ξ therefore gives the partonic structure of colour singlet exchange. The results of the two collaborations are consistent in most of the 15 phase space regions commonly covered, for example in Fig. 47b, and call in a few of them for homework (Fig. 47a), especially in an understanding of slightly different kinematic regions covered in the squared momentum transfer t and the mass of the diffractive system M_Y .

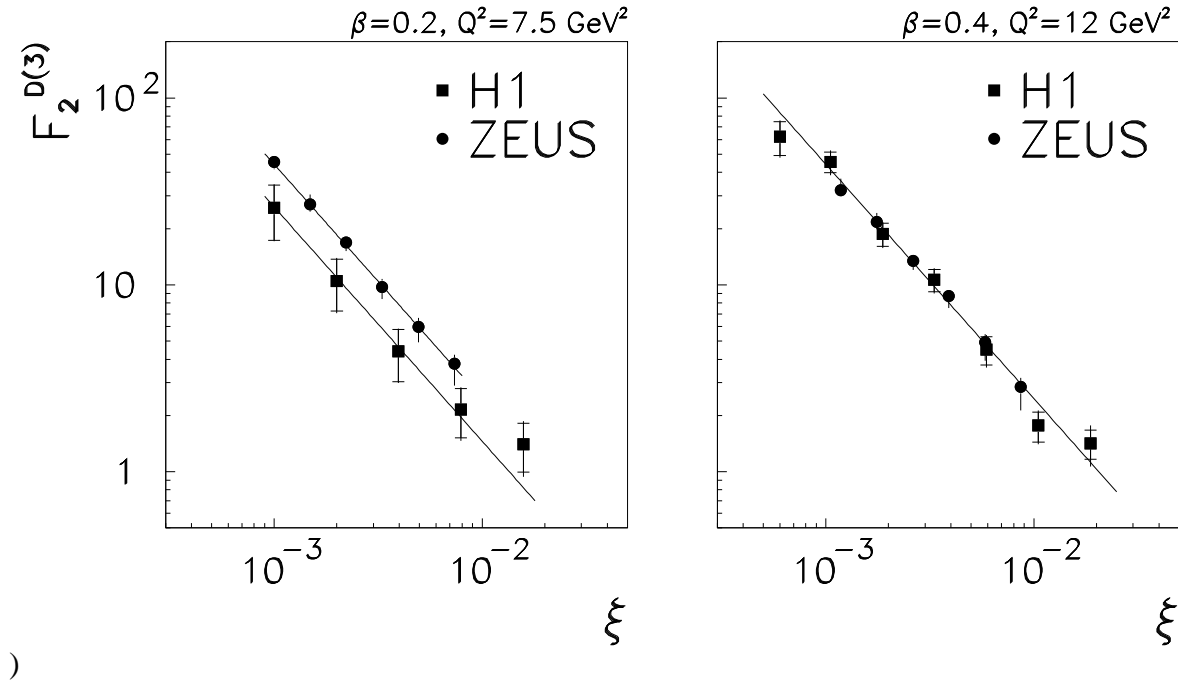


Figure 47: The ep structure function $F_2^{D(3)}$ of diffractive exchange is shown as a function of the fractional energy ξ of the exchanged object in two bins of the photon virtuality Q^2 and the parton fractional momentum β (H1 and ZEUS experiments). The curves have the functional form ξ^{-n} and serve the guidance of the eye.

In Fig. 48, the resolution scale Q^2 dependence of $F_2^{D(3)}$ of colour singlet exchange at large parton momenta $\beta = 0.4$ is shown. This measurement has been newly extended to large Q^2 up to 800 GeV^2 by the H1 collaboration [88]. The data are at relatively large values of $\xi = 0.02$ and can be described by a dominant diffractive exchange (Pomeron exchange) together with meson contributions (Reggeon exchange).

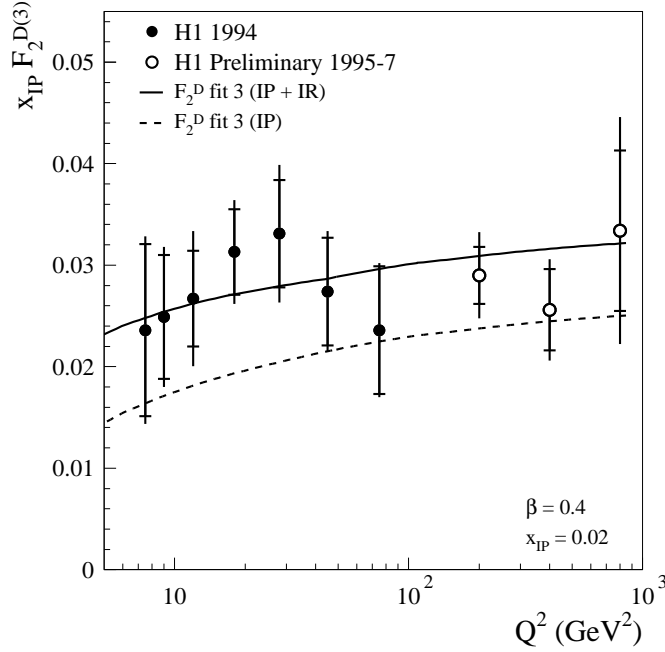


Figure 48: The structure function F_2 of the diffractive exchange is shown as a function of the virtuality Q^2 of the probing photon at the parton fractional momentum $\beta = 0.4$ and at the fractional momentum $\xi = x_{IP} = 0.02$ of the colour singlet object (H1 experiment). The curves are QCD fits to measurements below $Q^2 = 100 \text{ GeV}^2$.

The Q^2 dependence of $F_2^{D(3)}$ is found to be consistent with flat which is very different from the structure function measurements of hadrons, e.g., the proton structure function (Fig. 32 [89]). It is also different from the Q^2 dependence of the photon structure function (Fig. 31). The different distributions can be understood from the QCD evolution equations: the probability f_q of finding a quark in the proton, color singlet exchange, or photon depends logarithmically on Q^2 :

$$\frac{df_q}{d \ln Q^2} = P_{qq} \otimes f_q + P_{qg} \otimes f_g + P_{q\gamma} \quad (7)$$

The $P_{ij} \otimes f_j$ denote the splitting functions convoluted with the parton densities. The first term $P_{qq} \otimes f_q$ represents the contribution of quarks after radiating a gluon. The second term $P_{qg} \otimes f_g$ gives the contributions of gluons that split into a quark–anti-quark pair. The third term $P_{q\gamma}$ adds the quarks resulting from the photon splitting into a quark–anti-quark pair (relevant for photon only).

The proton structure function falls at large $x = 0.4$ with increasing resolution scale Q^2 : the probability of finding a parton in the proton above the average valence quark momentum decreases with increasing resolving power Q^2 (first term of eq. (7)). The logarithmic increase of the photon structure function with Q^2 is caused by the third term of eq. (7) which is to first approximation independent of Q^2 .

The structure function of diffractive exchange differs from those of the proton and the photon: the flat shape makes it distinct from a quark dominated object. The large rate of diffractive exchange excludes an explanation by photon exchange. Instead, a large gluon density in the exchanged diffractive object can explain the observed Q^2 dependence of the structure function which is driven by the second term of eq. (7). Therefore the structure function measurement mainly probes the gluon splitting into a quark–anti-quark pair and reflects the structure of the strong interactions.

This partonic structure of colour singlet exchange has been quantified by extracting gluon and quark distributions from the diffractive data using the structure function measurements alone (H1 Collaboration [87]) or in combination with jet cross section measurements (ZEUS Collaboration [90]).

Different final state observables have been measured in diffractive ep scattering by the H1 and ZEUS Collaborations, e.g., thrust [91, 92], di-jet cross sections [93, 90], energy flow [94, 92], multiplicity [95], and charm production [96, 97]. A large fraction of the measurements have been compared to Monte Carlo generators which simulate diffractive ep scattering processes by the emission of colour singlet objects with the parton distributions as extracted from the fits to $F_2^{D(3)}$ mentioned above. Overall, the data are well described by such simulations which demonstrates a consistently working framework for understanding diffractive parton scattering processes in ep collisions. A deviation of this good description of the data may be seen in the photoproduction of di-jets which is discussed below in the comparison of the rates of diffractive processes at the HERA and Tevatron colliders.

Note that the picture of exchanging a colour singlet object with a partonic structure is not the only one to describe the data: interesting alternative approaches exist which need fewer parameters and describe certain aspects of the data well. Examples are electron scattering off a quark or a gluon of the proton with colour neutralization by the exchange of a second parton that cancels the colour charge, or models that predict the β dependence of $F_2^{D(3)}$, or the concept of fracture functions [98]. For reviews of the different approaches refer to, e.g., [99, 100].

Colour Singlet Exchange at the Tevatron

The methods used by the Tevatron experiments CDF and D0 to select diffractive scattering processes are detection of leading protons (method A) or measurement of rapidity gaps (method B). The observables used to analyse the diffractive exchange are di-jet formation and the production of W-bosons.

Both experiments have observed events involving the exchange of one or - as a new result - two colour singlet objects (Fig. 49a,c [101, 102]). In the latter process, the jets are produced centrally and in each beam direction a large rapidity gap or a tagged proton is observed. In

Fig. 50, the shapes of transverse energy E_t^{jet} distributions of the leading jets in di-jet events are compared for single and double colour singlet exchange and non-diffractive data (CDF Collaboration). The E_t^{jet} range covered and the similarity of these distributions give several interesting observations:

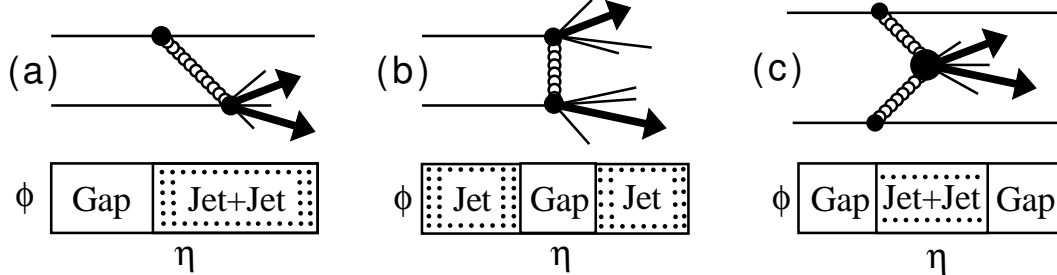


Figure 49: Di-jet production at the Tevatron with a) rapidity gap on one beam side, b) rapidity gap between the jets, or c) central jet production with two rapidity gaps.

The diffractive di-jet production results from the same type of parton-parton scattering processes as the non-diffractive data. In the latter case, the fractional momenta of the partons from the proton are small $x \sim E_t^{jet}/\sqrt{s} \sim 10/1800$ and therefore likely to come from gluon-gluon scattering processes. In the diffractive case with the exchange of one or two colour singlet objects, the center-of-mass energy of the scattering process is much smaller than that of the $\bar{p}p$ beams since these objects carry only a fraction of the beam proton energy. Nevertheless, the jet transverse energy reaches out to $E_t^{jet} \sim 20$ GeV such that almost the full energy of these objects is involved in the hard parton-parton scattering process.

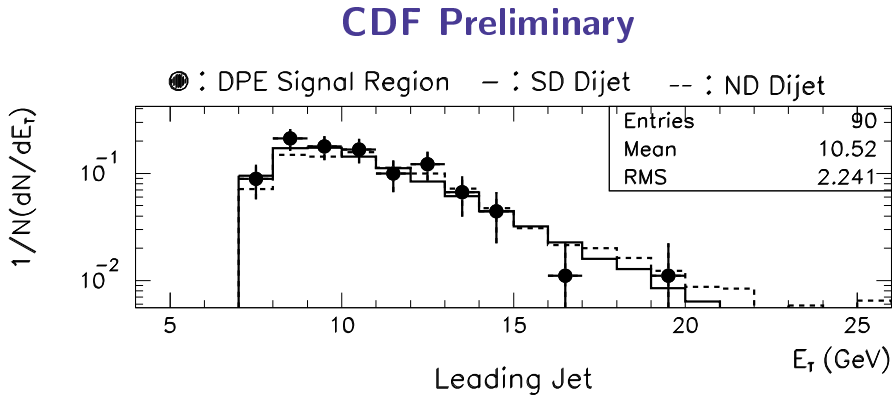


Figure 50: The shape of the transverse energy spectrum of the leading jet is shown from non-diffractive (dashed histogram), single diffractive (full histogram), and double diffractive (full circles) events in $\bar{p}p$ collisions (CDF experiment).

Both Tevatron experiments have observed events with a rapidity gap between two jets (Fig. 49b [101, 103]). In these events, the full energy of the exchanged object is involved in the jet production process and the object is probed at very large squared four-momentum

transfer $|t|$ of the order of $(E_t^{jet})^2$. In Fig. 51, the rate of events with such a colour singlet exchange relative to non-diffractive events is shown from the D0 collaboration. The distribution of the size of the rapidity gap is shown to be within errors independent of the jet transverse energy (Fig. 51b,c). In Fig. 51a, the rate is given as a function of the jet transverse energy which has a tendency to rise with increasing E_t^{jet} .

The data are sufficiently precise to discriminate different models of colour singlet exchange: they exclude the exchange of a photon (dotted curves in Fig. 51) and a calculation using two hard gluons ('BFKL', dashed curves [104]). The data can be consistently described by a model calculating the exchange of one energetic gluon with an additional parton to ensure colour neutrality (full curve [105]).

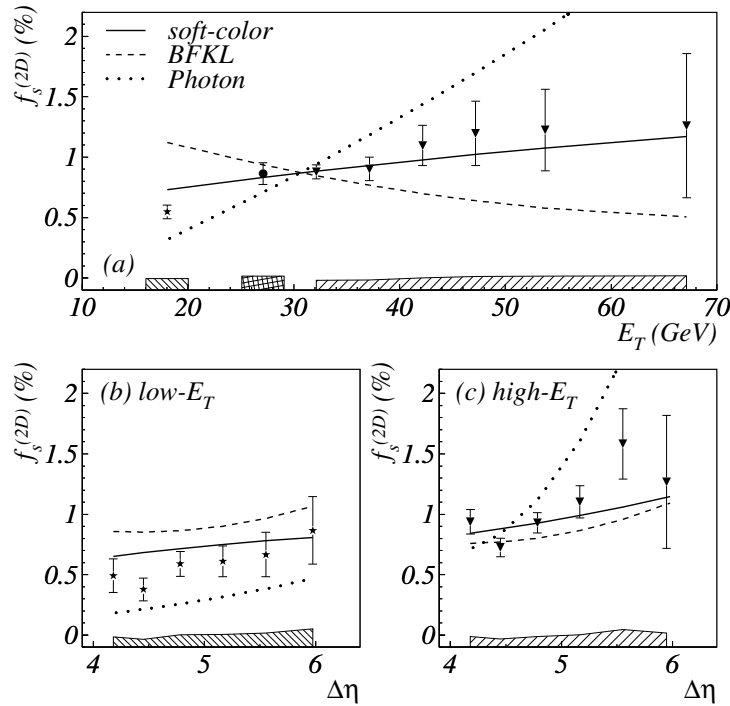


Figure 51: The rate of $\bar{p}p$ events with a rapidity gap between two jets is shown from preliminary D0 data: a) differentially in the transverse jet energy E_t^{jet} , and in b,c) as a function of the gap size $\Delta\eta$ for low and high values of E_t^{jet} . The curves represent the predictions of different model calculations.

The CDF experiment has observed the production of W-bosons in diffractive scattering processes [106]. These events have essentially one lepton and missing transverse energy and can be interpreted as resulting from quark-anti-quark fusion. A comparison of the diffractive W-boson rate with that of the di-jet production is shown in Fig. 52 as a function of the relative gluon contribution in the colour singlet object and is expressed as a momentum sum rule. The gluon contribution is found to be large 0.7 ± 0.2 which is well compatible with previous (shown in the figure) and new fits of the ZEUS collaboration [90] (not shown) and previous results of the H1 collaboration [87].

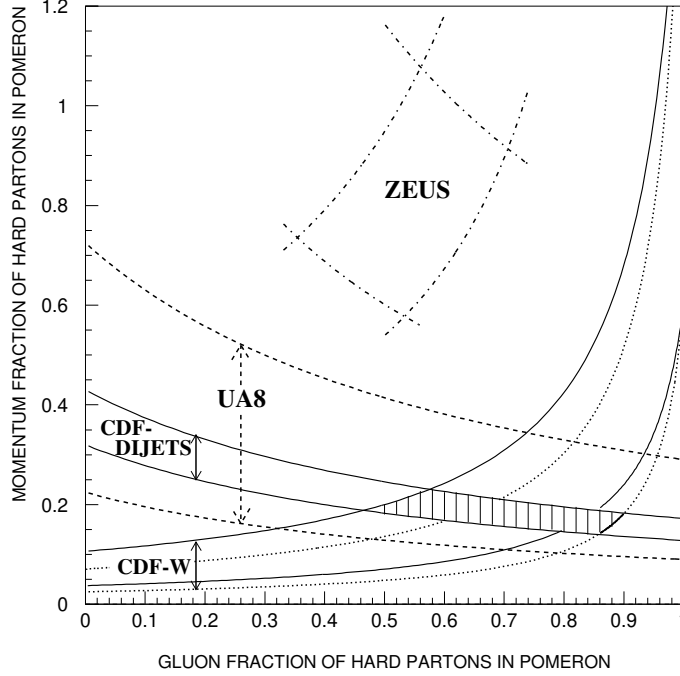


Figure 52: The total momentum fraction carried by the partons of the diffractive exchange object is shown as a function of the relative gluon contribution. The lower bands represent the region allowed from the measurements of diffractive di-jet production in $\bar{p}p$ collisions and W production respectively (CDF experiment). The bands in the upper half of the figure are a comparison of diffractive jet production with diffractive structure function measurements in ep collisions (ZEUS experiment).

Different Rates of Diffractive Processes at the HERA and Tevatron Colliders

While the large gluon component is consistently observed in diffractive processes at HERA and the Tevatron, the rate of such events is found to be largely different: at HERA, the rate of diffractive deep inelastic scattering events is of the order of 10%. In the phase space regions covered so far, the HERA final state data are overall consistently described when compared to calculations that use the parton distributions resulting from the diffractive structure function measurements. Using the same parton distributions for the Tevatron diffractive data, the predicted rate is much larger than the observed rate of the order of 1% [106, 107]. This discrepancy can, e.g., be expressed in terms of a momentum sum rule as shown in Fig. 52. The inconsistency is a puzzle which is under lively discussion.

Instructive measurements have been made, allowing the energy E_{ia} involved in the interaction to be measured relative to the total hadronic center-of-mass energy \sqrt{s} . In Fig. 53, rates of diffractive events are shown as a function of the ratio E_{ia}/\sqrt{s} .

For the Tevatron jet results [101, 102, 103], the jet transverse energy E_t^{jet} at the threshold has been used as a measure of E_{ia} (Fig. 53a-c). The rate of diffractive events appears to decrease as the total center-of-mass energy $\sqrt{s_{\bar{p}p}}$ becomes large relative to the energy involved in the scattering process.

Such dependence can, e.g., be explained by the increased potential of destroying the rapidity gap by beam remnant interactions which may be formulated in a reduced survival probability for the rapidity gap. Different other explanations have been suggested, key words are here absorption corrections, flux renormalization, or other means of factorization breaking [108, 109, 110].

For the HERA data, two measurements are discussed here: in the case of deep inelastic scattering data, the mass M_X of the diffractive system has been taken as a measure of E_{ia} . The data in Fig. 53d are consistent with being flat as a function of $M_X/\sqrt{s_{\gamma^*p}}$ [86] and show no indication of a decreasing survival probability.

In photoproduction of di-jets, the fractional momentum x of the parton from the photon is related to the ratio $E_t^{jet}/\sqrt{s_{\gamma p}}$. In Fig. 54, the di-jet cross section from diffractive scattering processes is shown as a function of x from H1 data [93]. At large $x \sim 1$, where the direct photon contribution dominates, the data are described by the calculations of the POMPYT generator [111] when using the parton distribution functions for the colour singlet exchange as extracted from the $F_2^{D(3)}$ measurements. However, at $x < 0.8$ the data are better described, if an overall reduction factor of $S = 0.6$ is applied to the calculation of the resolved photon–proton interactions. This observation hints for a reduced survival probability of the rapidity gap in resolved photon–proton processes. Owing to the presence of a proton and a photon remnant, these γp processes are similar to that of diffractive processes in $\bar{p}p$ collisions. In the future, more extended and precise measurements of the photoproduction of jets may help in the understanding of the different diffractive rates observed by the HERA and Tevatron experiments.

2.3 Vector Meson Production in ep Collisions

In elastic vector meson production from ep collisions, the full energy of the colour singlet object is involved in the scattering process (Fig. 55). Of special interest are processes with a hard scale such as

1. the mass M_V of a heavy vector meson,
2. the virtuality Q^2 of the photon in a deep inelastic scattering process, or
3. the squared four-momentum transfer t of the colour singlet exchange.

Such processes allow perturbative QCD calculations to be compared with the measurements and therefore give additional information on colour singlet exchange as well as on the proton and the vector meson [112].

In this context, the following measurements of vector meson production in ep collisions at HERA are discussed here:

1. vector meson cross sections and their dependencies on the center-of-mass energy $\sqrt{s_{\gamma p}}$, the photon virtuality Q^2 , and the squared momentum transfer t , and
2. photoproduction of J/ψ mesons from proton and nuclear targets.

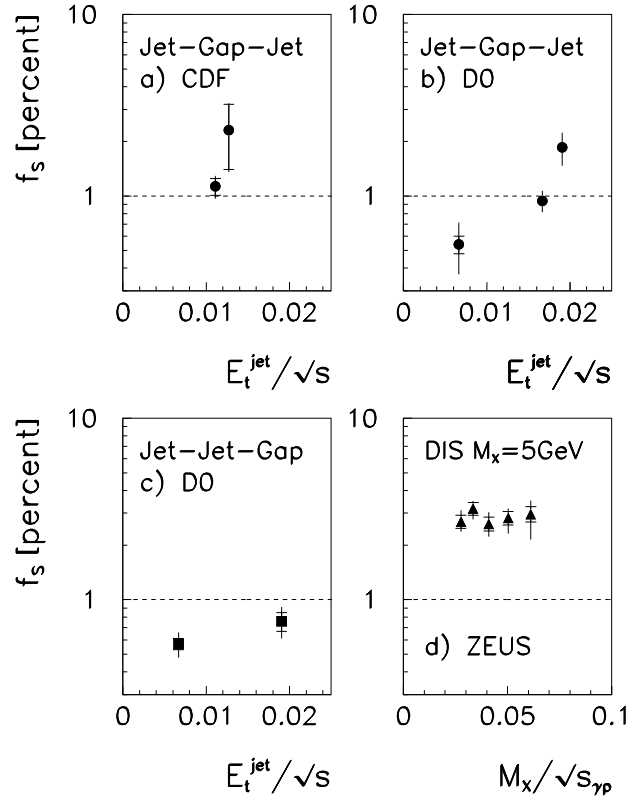


Figure 53: A comparison of the measured rates of diffractive interactions is shown as a function of the energy involved in the interaction relative to the total hadronic center of mass energy: a,b) rapidity gap signature between two jets of transverse energy above E_t^{jet} from $\bar{p}p$ collisions (CDF and D0 experiments), c) diffractive di-jet production in $\bar{p}p$ collisions (D0 data), and d) diffractive structure function in ep collisions where M_X denotes the mass of the diffractive system observed in the main detector (ZEUS experiment).

Measurements Related to the Gluon Distribution of the Proton

In Fig. 56, a compilation of the measurements of the total photoproduction cross section $\sigma_{\gamma p}$ and elastic vector meson cross sections $\sigma_{\gamma p}^V$ up to the production of Υ [113, 114] is shown as a function of the photon-proton center-of-mass energy $W \equiv \sqrt{s_{\gamma p}}$. The measured total cross section is at large center-of-mass energies compatible with a slowly rising distribution as

$$\sigma_{\gamma p} \sim s^\epsilon \quad (8)$$

with $\epsilon \sim 0.095 \pm 0.002$ [81]. The optical theorem relates the total cross section to the imaginary part of the amplitude of forward elastic scattering. Therefore, elastic vector meson cross sections should rise with approximately twice the power:

$$\sigma_{\gamma p}^V \sim s^{2\epsilon} . \quad (9)$$

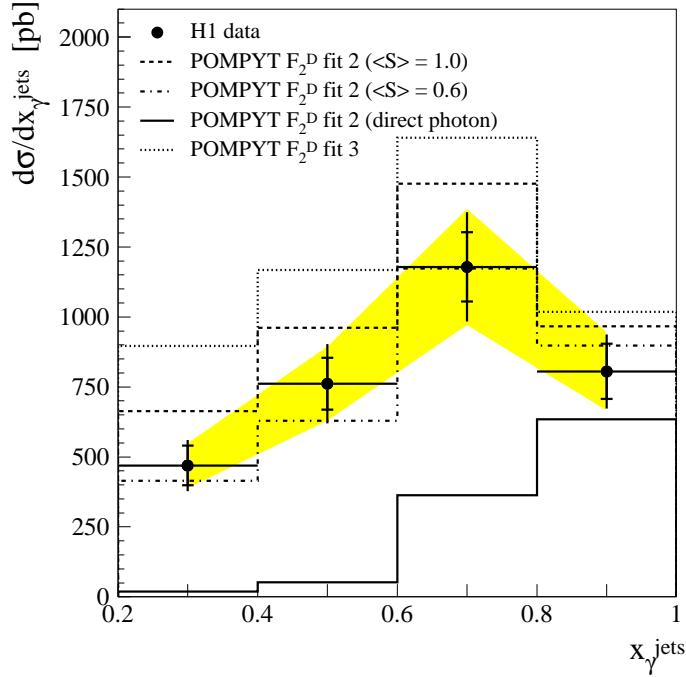


Figure 54: Photoproduction of di-jets in diffractive ep collisions is shown as a function of the fractional momentum x of the parton from the photon (H1 data). The dotted and dashed histograms show Monte Carlo generator calculations using two different parton distribution functions for the colour singlet exchange which were extracted from structure function measurements. The full histogram represents the contribution of direct photon–proton processes in diffractive interactions. In the dash-dotted histogram, a ‘rapidity gap survival factor’ of $S = 0.6$ was applied to the calculation for the generated momenta of the partons from the photon below $x = 0.8$.

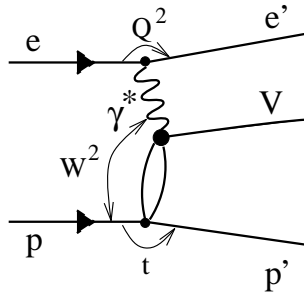


Figure 55: Feynman diagram of vector meson production in electron–proton scattering.

Photoproduction of light vector mesons (ρ , ω , φ) show an increase in the production that is compatible with this prediction. However, photoproduction of the heavy J/ψ mesons exhibit a stronger dependence on the center-of-mass energy with $\epsilon \sim 0.2$.

A steeper energy dependence is also observed for light vector meson production in deep inelastic scattering processes: in Fig. 57a, the energy dependence of new $\sigma_{\gamma p}^V$ measurements by the H1 and ZEUS Collaborations [76, 115, 116, 117] was again expressed in terms of the fit

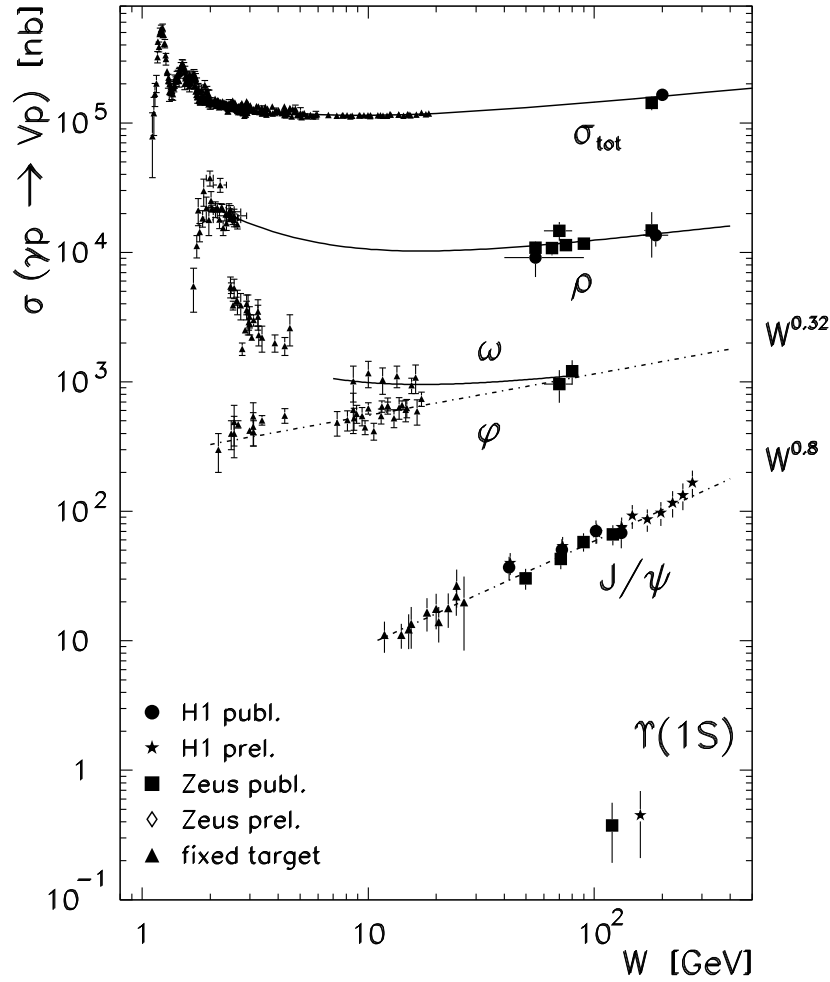


Figure 56: The photon-proton total cross section and vector meson cross sections from fixed target experiments and ep collisions at HERA are shown as a function of the photon-proton center of mass energy $W \equiv \sqrt{s_{\gamma p}}$. The full curves represent the predictions of a Regge model. The dashed curves are functions of the form $W^\delta \equiv (s_{\gamma p})^{2\epsilon}$ to guide the eye.

parameter ϵ using eq. (9) and is shown as a function of the scale. The scale was here chosen to be the sum of the photon virtuality and the vector meson squared mass $Q^2 + M_V^2$. The parameter ϵ is found to increase with increasing scale.

Such energy dependence is similar to that observed in inclusive deep inelastic scattering cross sections (Fig. 57b [120]). At fixed Q^2 and small parton momenta x_{Bj} , the total photon-proton cross section σ_{γ^*p} is directly related to the large gluon density observed in the proton which gives rise to the $(x_{Bj})^{-\lambda}$ dependence of the proton structure function F_2 . Using the relation $x_{Bj}s_{\gamma^*p} \approx Q^2 = \text{const.}$ gives an energy dependence of the cross section as $\sigma_{\gamma^*p} \sim F_2 \sim (x_{Bj})^{-\lambda} \sim (s_{\gamma^*p})^\lambda$. The similar energy dependencies observed in vector meson production (Fig. 57a) and inclusive deep inelastic scattering processes (Fig. 57b) is suggestive of sensitivity of the vector meson data to the gluon distribution of the proton.

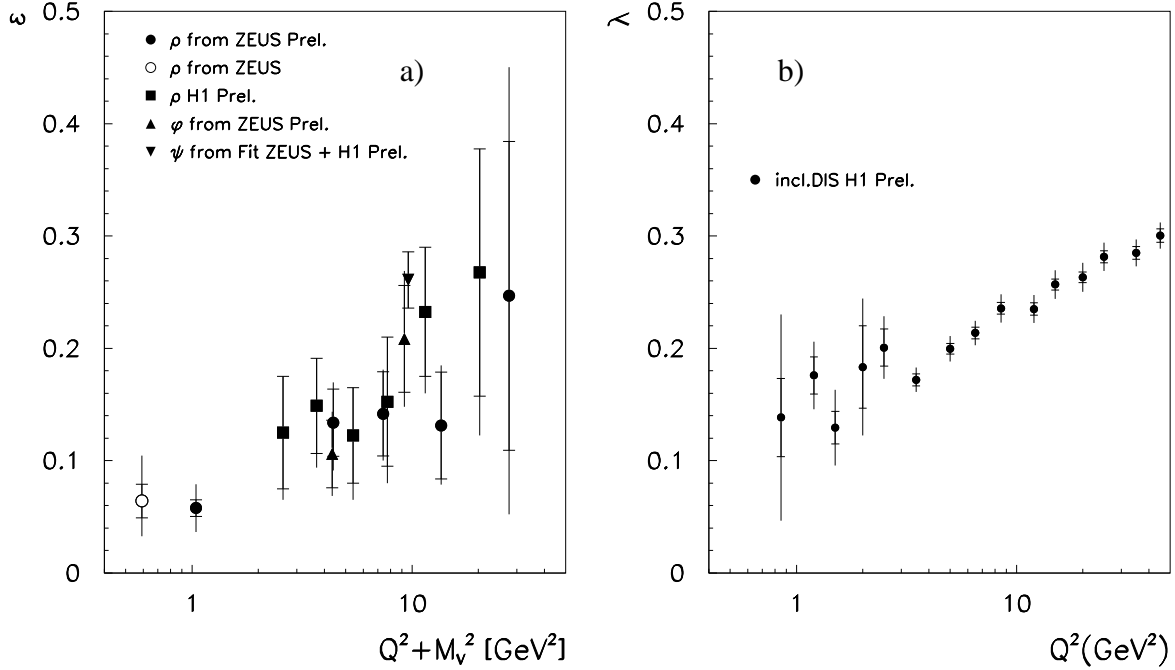


Figure 57: a) The energy dependence of vector meson cross sections $\sigma_{\gamma p}^V \sim (s_{\gamma^*p})^{2\epsilon}$ in ep collisions is shown as a function of the scale taken here to be the sum of the photon virtuality Q^2 and the vector meson squared mass M_V^2 (H1 and ZEUS experiments). b) The energy dependence of inclusive cross section measurements $\sigma_{\gamma^*p} \sim (s_{\gamma^*p})^\lambda$ is shown as a function of the photon virtuality Q^2 from H1 data.

In Fig. 58, the longitudinal component of the ρ meson production cross section is shown as a function of x_{Bj} in four bins of Q^2 [115]. Similarly, the J/ψ production cross section is shown in Fig. 59 as a function of the photon–proton center-of-mass energy $W \equiv \sqrt{s_{\gamma^*p}}$ [117].

The measurements can be described by perturbative QCD calculations which use existing parameterizations of the gluon distributions in the proton (curves [118, 119]). The calculations use the square of the gluon density to account for the colour neutrality of the exchanged object (e.g. Fig. 60). Therefore, the comparisons of the data with the calculations give a highly sensitive measure of the gluons in the proton. A further component of the calculations is the mechanism for formation of the vector meson such that the comparisons to the data will give new information also on this part of the process.

Measurements Related to Quark–Anti-Quark States

In elastic vector meson production, the squared momentum transfer t , which is exchanged between the vector meson and the proton, gives information on the size of the interaction region. Such t distributions can be fitted for small values of t using an exponential distribution $\exp(-bt)$.

In Fig. 61, a compilation of the fitted b parameters is shown for the HERA data for ρ , φ , and J/ψ meson production as a function of the scale (new measurements: [76, 115, 116, 117]).

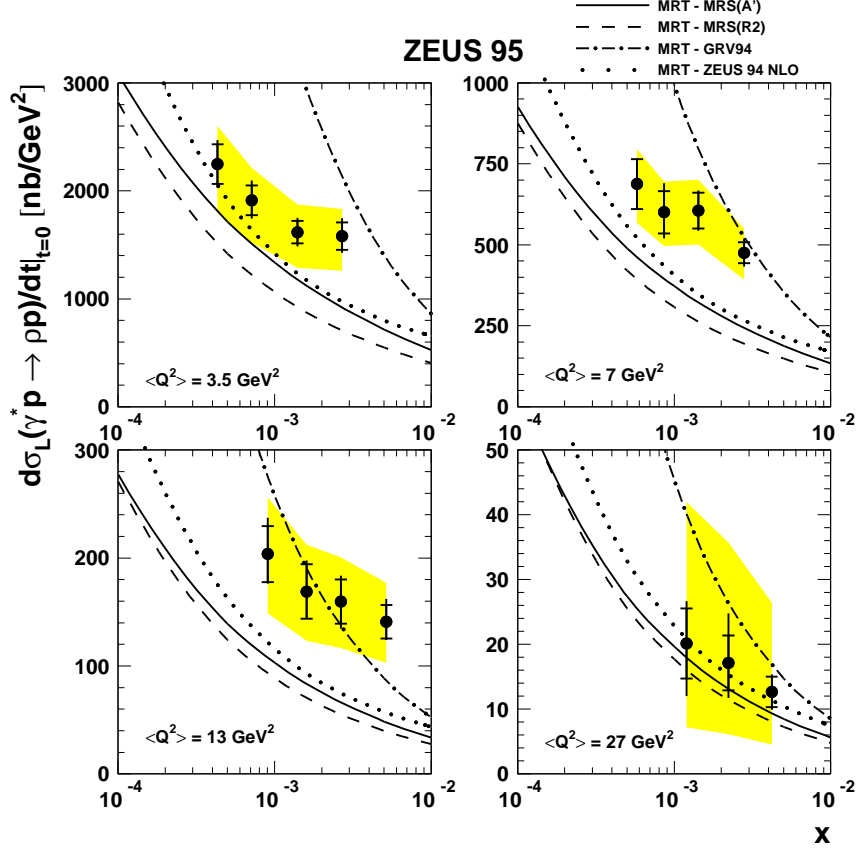


Figure 58: The longitudinal ρ meson cross section from deep inelastic ep scattering is shown as a function of the proton parton fractional momentum x_{Bj} in four bins of the photon virtuality Q^2 (ZEUS experiment). The curves represent the predictions of QCD calculations using different gluon distributions of the proton.

The scale has here again been chosen to be the sum of the photon virtuality Q^2 and the vector meson squared mass M_V^2 . With increasing scale, the data tend to approach a constant value of $b \sim 4 \text{ GeV}^{-2}$ which corresponds to the size of the proton. The size of the $q\bar{q}$ state is therefore small compared to that of the proton and probes the proton at small distances.

The b parameter measured for the photoproduction of J/ψ mesons indicates the small size of the charm–anti-charm object in the interaction with the proton. Further information on this $c\bar{c}$ configuration results from nuclear dependencies of non-diffractive J/ψ meson production in comparison to that of protons [121]:

In Fig. 62, the shapes of proton–nucleus cross sections $pA \rightarrow pX$ [122] are shown as a function of the rapidity change Δy . Here Δy denotes the rapidity difference between the beam proton and the most energetic tagged proton. These distributions can be described by an exponential form $\exp(-\Delta y/\Delta y_0)$. The fitted slopes decrease as the nuclear mass increases, i.e., the protons are on average more decelerated with a heavier target.

It is interesting to compare the deceleration process of the protons with that of J/ψ mesons resulting from non-diffractive photoproduction off nuclei $\gamma A \rightarrow J/\psi X$. Here the rapidity

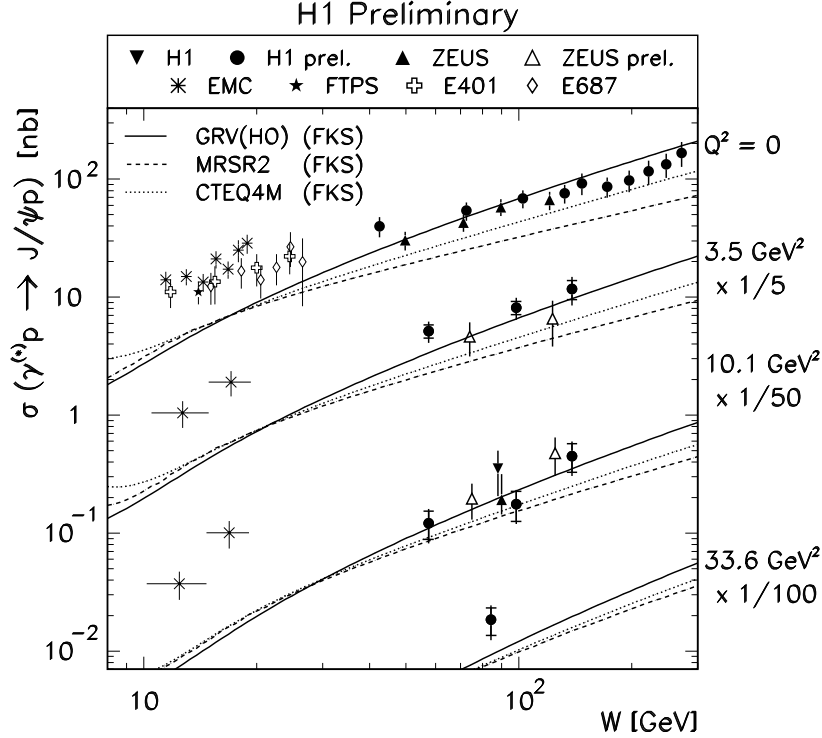


Figure 59: The J/ψ cross section from fixed target experiments and ep collisions at HERA is shown as a function of the photon-proton center of mass energy W in four bins of the photon virtuality Q^2 . The curves represent the predictions of QCD calculations using different gluon distributions of the proton.

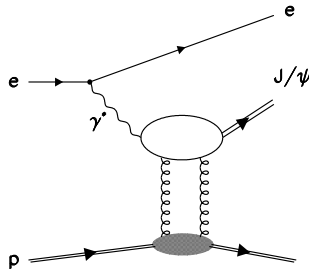


Figure 60: Feynman diagram of J/ψ meson production in electron–proton scattering with two-gluon exchange.

difference between the photon and the J/ψ is used as a measure of the deceleration process (Fig. 62, data of the EMC [123], H1 [124], and ZEUS [125] experiments).

Also these distributions in the rapidity difference can be described by an exponential form. In contrast to the proton data, the slope of the J/ψ production does not decrease with increasing mass of the nucleus which implies that the iron target does not decelerate the $c\bar{c}$ object better than the proton target. The slight increase in the slope with A can be explained, according to Monte Carlo generator studies, by the different center-of-mass energies of the EMC and the HERA experiments.

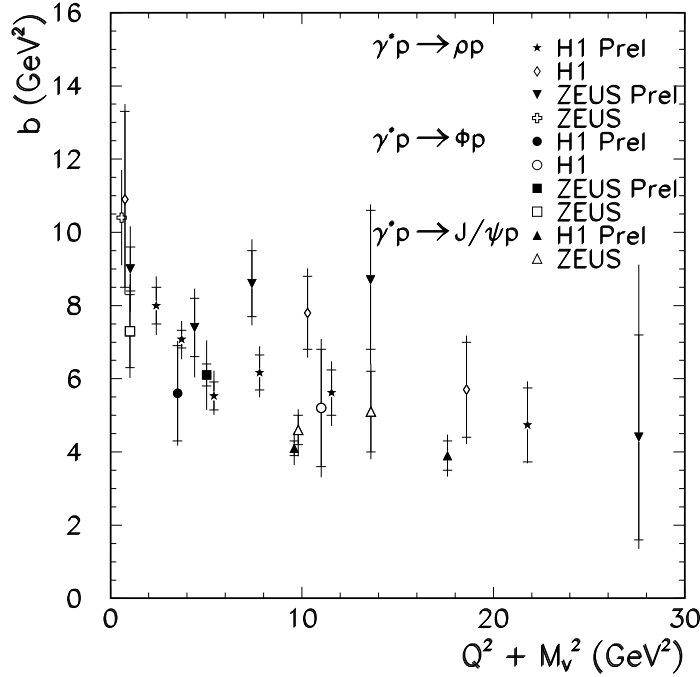


Figure 61: The fitted b parameter of the four-momentum transfer t distribution $\exp(-bt)$ is shown for the production of different vector mesons in ep collisions at HERA as a function of the scale which is here taken to be the sum of the photon virtuality Q^2 and the vector meson squared mass M_V^2 .

The absence of a nuclear deceleration effect for the J/ψ mesons may be interpreted as resulting from nuclear transparency. For a discussion of nuclear transparency effects refer, e.g., to [126]. In this interpretation, the colour charges of the small quark–anti-quark configuration are sufficiently screened to penetrate a nucleus without further interactions.

2.4 Summary 2: Colour Singlet Exchange

The HERA and Tevatron experiments have measured different observables that can be related to the parton distributions of diffractive exchange. Using structure function measurements in ep collisions, di-jet production in ep and $\bar{p}p$ scattering, and W-Boson production in $\bar{p}p$ collisions, they consistently find a large gluon component in this colour singlet state.

The overall rate of diffractive processes observed in ep and $\bar{p}p$ collisions, however, is found to be different and challenges explanation.

Measurements of elastic vector meson production involving a hard scale provide an alternative approach to understanding colour singlet exchange. Comparisons of the data with QCD calculations that rely on two-gluon exchange give new information on the gluon distribution of the proton and on the vector meson states.

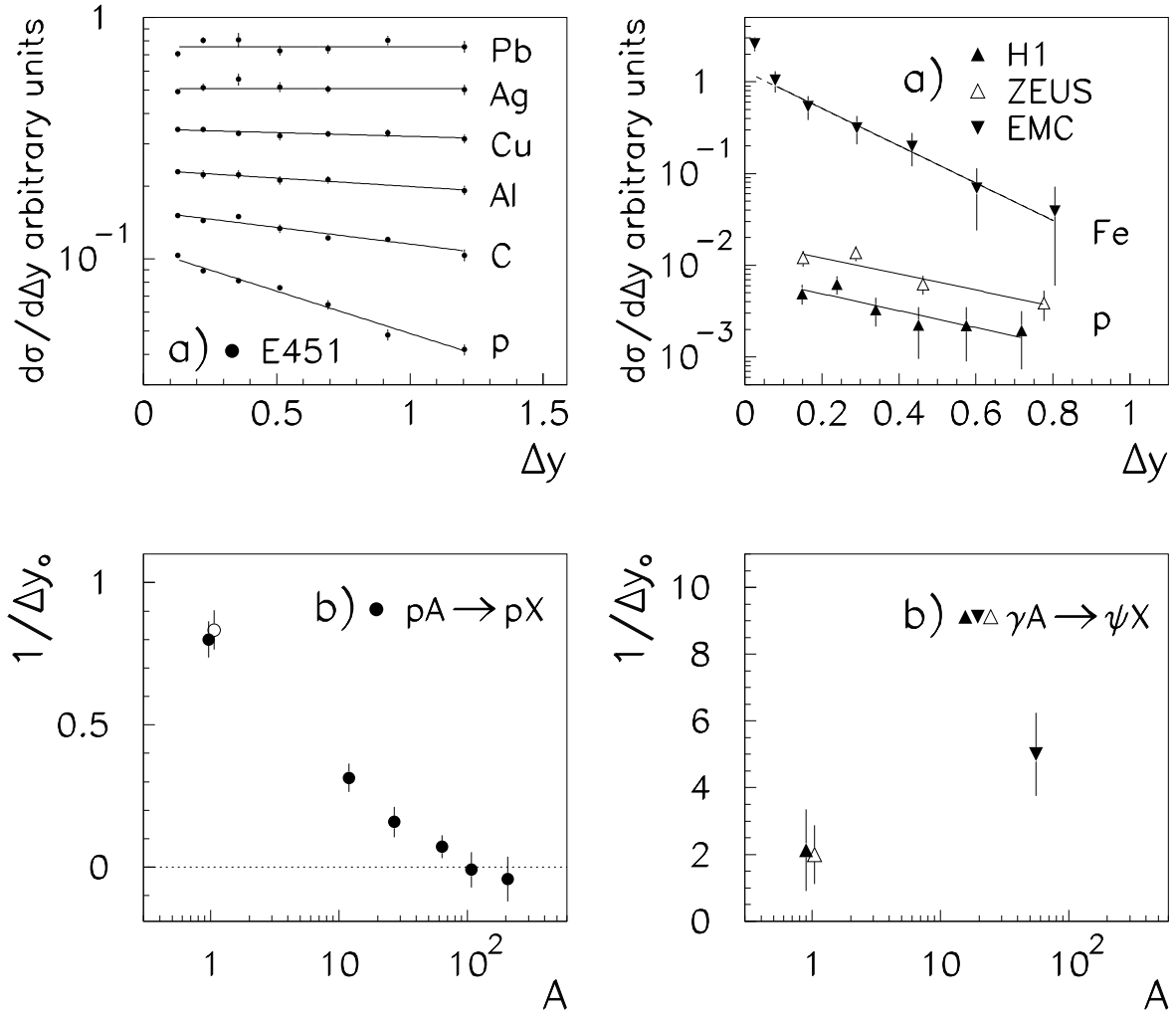


Figure 62: Left figures: a) shape of the rapidity change of beam protons in proton–nucleus interactions. The curves represent exponential fits to the data. b) The slopes $1/\Delta y_0$ of the fits in a) are shown as a function of the target mass A . Right figures: a) shape of the rapidity difference between the initial-state photon and the ψ meson observed in lepton–proton (triangle symbols pointing up) and lepton–iron interactions (triangle symbols pointing down). The curves represent exponential fits to the data. b) The slopes $1/\Delta y_0$ of the fits in c) are shown as a function of the target mass A .

At sufficiently large scales, the spatial extension of the quark–anti-quark states appears to be small. Photoproduction of J/ψ mesons indicates that the $c\bar{c}$ state penetrates a nuclear environment essentially undisturbed.

Overall, diffractive physics is a very active field of research and is developing away from a soft interaction language to the understanding of a fundamental process of strong interactions within the framework of QCD.

Acknowledgements

It is a pleasure to thank Alan Astbury and co-organisers for an excellent conference.

T.D. expresses many thanks to Halina Abramowicz, Arie Bodek, Antje Brull, Allen Caldwell, Abe Deshpande, John Dainton, Robin Devenish, Martin Erdmann, Laurent Favart, Thomas Gehrmann, Tim Greenshaw, Beate Heinemann, Peppe Iacobucci, Robert Klanner, Max Klein, Masahiro Kuze, Ludger Lindemann, Alan Martin, Gavin McCance, Jan Okrasinski, Jen-Chieh Peng, Alex Prinias, Robert Waugh, Arnulf Quadt, David Saxon, Stefan Schlenstedt, Mike Vetterli, Manuella Vincter, Bryan Webber, Jim Whitmore, Un-Ki Yang, Rik Yoshida, Jaehoon Yu and all the speakers in the structure functions parallel session for their help, inspiration and advice.

M.E. wishes to thank for kind help in preparing the talk H. Abramowicz, M. Albrow, V. Andreev, K. Borras, A. Brandt, J. Dainton, T. Doyle, K. Freudenreich, C. Glasman, B. Heinemann, M. Kienzle, P. Newman, R. Nisius, G. Snow, and S. Söldner-Rembold. For careful reading of the manuscript and comments I wish to thank H. Abramowicz, M. Albrow, J. Dainton, M. Kienzle, P. Newman, G. Snow, and S. Söldner-Rembold.

We are grateful for financial support (T.D.) to the Alexander von Humboldt Foundation, DESY and PPARC, and (M.E.) to the Deutsche Forschungsgemeinschaft for the Heisenberg Fellowship.

References

- [1] V. Fadin and L. Lipatov, hep-ph/9802290.
- [2] J.R. Forshaw, G.P. Salam and R.S. Thorne, hep-ph/9812304.
- [3] L.V. Gribov, E.M. Levin and M.G. Ryskin, *Phys. Rep.* **100** (1) 1983;
E.M. Levin and M.G. Ryskin, *Nucl. Phys.* **B 18C** (92) 1990.
- [4] J. Huston, Proc. 29th Intern. Conf. on High-Energy Physics, Vancouver, Canada (1998).
- [5] Y. Dokshitzer, Proc. 29th Intern. Conf. on High-Energy Physics, Vancouver, Canada (1998).
- [6] A.D. Martin, R.G. Roberts, W.J. Stirling and R.S. Thorne, hep-ph/9803445.
- [7] M. Glück, E. Reya and A. Vogt, hep-p/9806404.
- [8] CTEQ Collab., H.L. Lai et al., *Phys. Rev.* **D 55** (1280) 1997.
- [9] S.A. Larin and J.A.M. Vermaseren, *Phys. Lett.* **B 259** (345) 1991.
- [10] A.L. Kataev and V.V. Starshenko, *Mod. Phys. Lett. A* **10** (235) 1991.
- [11] J.H. Kim, D.A. Harris et al., hep-ex/9808015, submitted to *Phys. Rev. Lett.*

- [12] S.A. Kulagin, hep-ph/9809219.
- [13] A.L. Kataev, G. Parente and A.V. Sidorov, hep-ph/9809500.
- [14] CCFR Collab., W. Seligman et al., hep-ph/9701017.
- [15] M. Virchaux and A.M. Milsztajn, *Phys. Lett.* **B 274** (221) 1992.
- [16] C. Caso et al., *Eur. Phys. J. C* **3** (1) 1998.
- [17] F. Eisele, Physics in Collision proceedings, hep-ph/9807028.
- [18] U. Yang and A. Bodek, Proc. 29th Intern. Conf. on High-Energy Physics, Vancouver, Canada (1998), hep-ph/9809480.
- [19] L. Frankfurt and M. Strikman, *Phys. Rep.* **160** (235) 1988.
- [20] M. Dasgupta and B.R. Webber, *Phys. Lett.* **B 382** (273) 1996.
- [21] CCFR Collab., U.K. Yang et al., DIS98 proceedings, hep-ex/9806023;
J. Yu, Proc. 29th Intern. Conf. on High-Energy Physics, Vancouver, Canada (1998).
- [22] CDF Collaboration, F. Abe et al., hep-ex/9809001, submitted to *Phys. Rev. Lett.*;
W. Sakumoto, Proc. 29th Intern. Conf. on High-Energy Physics, Vancouver, Canada (1998).
- [23] NMC Collab., M. Arneodo et al., *Phys. Rev.* **D 50** (1) 1994.
- [24] S. Kumano and K. Umekawa, hep-ph/9803359.
- [25] E866 Collab., E.A. Hawker et al., *Phys. Rev. Lett.* **80** (3715) 1998.
- [26] E866 Collab., J.C. Peng et al., hep-ex 9804288, submitted to *Phys. Rev.* **D**.
- [27] HERMES Collab., K. Ackerstaff et al., hep-ex/9807013;
M. Vinciter, Proc. 29th Intern. Conf. on High-Energy Physics, Vancouver, Canada (1998).
- [28] C. Boros, J. Londergan and A. Thomas, hep-ph/9804410. C. Boros, Proc. 29th Intern. Conf. on High-Energy Physics, Vancouver, Canada (1998).
- [29] CCFR Collab., A. Bazarko et al., *Z. Phys.* **C 65** (189) 1995.
- [30] D. Karlen, Proc. 29th Intern. Conf. on High-Energy Physics, Vancouver, Canada (1998).
- [31] SMC Collab., B. Adeva et al., CERN-EP/98-86, submitted to *Phys. Rev.* **D**;
A. Deshpande, Proc. 29th Intern. Conf. on High-Energy Physics, Vancouver, Canada (1998).
- [32] G. Altarelli, R.D. Ball, S. Forte and G. Ridolfi, *Nucl. Phys.* **B 496** (337) 1997.
- [33] L. Sorrell, Proc. 29th Intern. Conf. on High-Energy Physics, Vancouver, Canada (1998).
- [34] E. Rondio, Proc. 29th Intern. Conf. on High-Energy Physics, Vancouver, Canada (1998).

- [35] F.E. Close and R.G. Roberts, *Phys. Lett.* **B 336** (1257) 1994.
- [36] J. Ellis, DIS98 proceedings (World Scientific) in press;
J. Ellis and M. Karliner, *Phys. Lett.* **B 341** (397) 1995.
- [37] B. Lampe and E. Reya, hep-ph/9810270.
- [38] SMC Collab., D. Adeva et al., hep-ex/9711008, submitted to *Phys. Lett.* **B**.
- [39] C.A. Miller, Proc. 29th Intern. Conf. on High-Energy Physics, Vancouver, Canada (1998).
- [40] ZEUS Collab., J. Breitweg et al., DESY 98-121, submitted to *Eur. Phys. J. C*;
A. Quadt, Proc. 29th Intern. Conf. on High-Energy Physics, Vancouver, Canada (1998).
- [41] H1 Collab., C. Adloff et al., ICHEP98 contributed papers 534 and 535;
M. Klein, Proc. 29th Intern. Conf. on High-Energy Physics, Vancouver, Canada (1998).
- [42] A.H. Mueller, DIS98 proceedings (World Scientific) in press.
- [43] M. Botje, DIS97 proceedings, *AIP Conf. Proc.* **407** (393) 1997.
- [44] H1 Collab., C. Adloff et al., ICHEP98 contributed papers 538 and 540;
E. Tzamariudaki, Proc. 29th Intern. Conf. on High-Energy Physics, Vancouver, Canada (1998).
- [45] ZEUS Collab., J. Breitweg et al., ICHEP98 contributed papers 768 and 772;
W. Verkerke, Proc. 29th Intern. Conf. on High-Energy Physics, Vancouver, Canada (1998).
- [46] B.W. Harris and J. Smith, *Nucl. Phys.* **B 452** (109) 1995;
B.W. Harris and J. Smith, *Phys. Lett.* **B 353** (535) 1995;
B.W. Harris and J. Smith, hep-ph/9706334.
- [47] OPAL Collab., K. Ackerstaff et al., *Eur. Phys. J. C* **1** (439) 1998.
- [48] H1 Collab., S. Aid et al., *Phys. Lett.* **B 393** (452) 1997.
- [49] H1 Collab., C. Adloff et al., *Z. Phys.* **C 74** (191) 1997.
- [50] ZEUS Collab., J. Breitweg et al., *Z. Phys.* **C 74** (207) 1997.
- [51] H1 Collab., C. Adloff et al., ICHEP98 contributed paper 533;
M. Fleischer, Proc. 29th Intern. Conf. on High-Energy Physics, Vancouver, Canada (1998).
- [52] ZEUS Collab., J. Breitweg et al., ICHEP98 contributed papers 751 and 752;
J. Grosse-Knetter, Proc. 29th Intern. Conf. on High-Energy Physics, Vancouver, Canada (1998).
- [53] M. Erdmann, *The Partonic Structure of the Photon*, Springer Tracts in Modern Physics, Heidelberg, Vol. 138 (1997)

- [54] L3 Collab., *Study of the Photon Structure Function F_2^γ at LEP*, paper 525 of the 29th Intern. Conf. on High-Energy Physics, Vancouver, Canada (1998)
- [55] R. Engel, *Z. Phys. C* **66** (203) 1995,
R. Engel and J. Ranft, *Phys. Rev. D* **54** (4244) 1996,
R. Engel et al., *Phys. Rev. D* **46** (5192) 1992
- [56] TWOGAM 1.71, S. Nova et al., DELPHI note 90-35 (1990)
- [57] OPAL Collab., K. Ackerstaff, et al., *Phys. Lett. B* **412** (225) 1997
- [58] H. Abramowicz, K. Charchula and A. Levy, *Phys. Lett. B* **269** (458) 1991
- [59] M. Glück, E. Reya and A. Vogt, *Phys. Rev. D* **46** (1973) 1992
- [60] G. A. Schuler and T. Sjöstrand, *Z. Phys. C* **68** (607) 1995
- [61] Compilation by R. Nisius (1998)
- [62] H1 Collab., C. Adloff, et al., *Eur. Phys. J. C* **1** (97) 1998
- [63] B.L. Combridge and C.J. Maxwell, *Nucl. Phys. B* **239** (429) 1984
- [64] ZEUS Collab., *High-Mass Di-Jet Cross Sections in Photoproduction at HERA*, paper 805 of the 29th Intern. Conf. on High-Energy Physics, Vancouver, Canada (1998)
- [65] M. Klasen, T. Kleinwort and G. Kramer, *Inclusive Jet Production in γp and $\gamma\gamma$ Processes: Direct and Resolved Photon Cross-Sections in Next-to-Leading Order QCD*, DESY-97-234 (1997), hep-ph - 9712256
- [66] L. E. Gordon and J. K. Storrow, ANL-HEP-PR-96-33, hep-ph-9607370 (1996)
- [67] L3 Collab., *Measurement of the Inclusive Charm Production in $\gamma\gamma$ Collisions at LEP with the L3 Detector*, paper 517 of the 29th Intern. Conf. on High-Energy Physics, Vancouver, Canada (1998)
- [68] M. Drees, M. Kramer, J. Zunft and P.M. Zerwas, *Phys. Lett. B* **306** (371) 1993
- [69] V. Andreev, private communications
- [70] H1 Collab., *Di-Jet Cross Sections in Photoproduction and Determination of the Gluon Density in the Photon*, paper 549 of the 29th Intern. Conf. on High-Energy Physics, Vancouver, Canada (1998)
- [71] OPAL Collab., G. Abbiendi, et al., *Di-Jet Production in Photon-Photon Collisions at $\sqrt{s_{ee}} = 161$ GeV and 172 GeV*, CERN-EP-98-113, subm. to *Eur. Phys. J. C* (1998)
- [72] T. Kleinwort and G. Kramer, *Nucl. Phys. B* **477** (3) 1996,
T. Kleinwort and G. Kramer, *Phys. Lett. B* **370** (141) 1996
- [73] T. Sjöstrand, CERN-TH-6488 (1992), *Comp. Phys. Commun.* **82** (74) 1994

- [74] H1 Collab., *Measurement of Di-jet Cross-Sections in Low Q^2 Deep-Inelastic Scattering Processes at HERA and the Extraction of an Effective Parton Density of the Virtual Photon*, paper 544 of the 29th Intern. Conf. on High-Energy Physics, Vancouver, Canada (1998)
- [75] H. Jung, *Comp. Phys. Commun.* **86** (147) 1995
- [76] H1 Collab., *Elastic Electroproduction of rho Mesons for $1 < Q^2 < 60 \text{ GeV}^2$ at HERA*, paper 564 of the 29th Intern. Conf. on High-Energy Physics, Vancouver, Canada (1998)
- [77] G. A. Schuler and T. Sjöstrand, *Phys. Lett.* **B 376** (193) 1996
- [78] L3 Collab., *Cross section of hadron production in $\gamma\gamma$ collisions at LEP*, paper 519 of the 29th Intern. Conf. on High-Energy Physics, Vancouver, Canada (1998)
- [79] S. Söldner-Rembold, Proc. of the 29th Intern. Conf. on High-Energy Physics, Vancouver, Canada (1998), hep-ex 9810011
- [80] OPAL Collab., *Total Hadronic Cross-Section for Photon-Photon Interactions at LEP*, paper 199 of the 29th Intern. Conf. on High-Energy Physics, Vancouver, Canada (1998)
- [81] J.R. Cudell, K. Kang and S.K. Kim, *Phys. Lett.* **B 395** (311) 1997, Review of Particle Physics, *Eur. Phys. J.* **C 3** (1) 1998
- [82] H1 Collab., *Measurement of Leading Baryon Production at HERA and its Interpretation in terms of Colour Singlet Exchange*, paper 569 of the 29th Intern. Conf. on High-Energy Physics, Vancouver, Canada (1998)
- [83] B. Kopeliovich, B. Povh and I. Potashnikova, *Z. Phys.* **C 73** (125) 1996
- [84] ZEUS Collab., *Leading Baryon Production in ep Scattering at HERA*, paper 789 of the 29th Intern. Conf. on High-Energy Physics, Vancouver, Canada (1998)
- [85] ZEUS Collab., J.Breitweg et al., *Eur. Phys. J.* **C 1** (81) 1998
- [86] ZEUS Collab., J.Breitweg et al., *Measurement of the Diffractive Cross Section in Deep Inelastic Scattering using ZEUS 1994 Data*, DESY 98-084 (1998), acc. by *Eur. Phys. J.* **C**
- [87] H1 Collab., C. Adloff, et al., *Z. Phys.* **C 76** (613) 1997
- [88] H1 Collab., *Measurement and Interpretation of the Diffractive Structure Function $F_2^{D(3)}$ at HERA*, paper 571 of the 29th Intern. Conf. on High-Energy Physics, Vancouver, Canada (1998)
- [89] H1 Collab., *Measurement of Inclusive Cross Sections for Neutral and Charged Current Interactions at High- Q^2* paper 533 of the 29th Intern. Conf. on High-Energy Physics, Vancouver, Canada (1998)
- [90] ZEUS Collab., J.Breitweg et al., *Diffractive Di-Jet Cross Sections in Photoproduction at HERA*, DESY 98-045, (1998) acc. by *Eur. Phys. J.* **C**

- [91] H1 Collab., C. Adloff et al., *Eur. Phys. J. C* **1** (495) 1998
- [92] ZEUS Collab., *Properties of hadronic final states in diffractive deep inelastic ep scattering at HERA*, paper 787 of the 29th Intern. Conf. on High-Energy Physics, Vancouver, Canada (1998)
- [93] H1 Collab., C. Adloff et al., subm. to *Eur. Phys. J. C*
- [94] H1 Collab., C. Adloff et al., *PLB* **428** (206) 1998
- [95] H1 Collab., C. Adloff et al., subm. to *Eur. Phys. J. C*
- [96] H1 Collab., *Production of $D^{*\pm}$ Mesons in Diffractive Interactions at HERA*, paper 558 of the 29th Intern. Conf. on High-Energy Physics, Vancouver, Canada (1998)
- [97] ZEUS Collab., *Open Charm Production in Diffractive Deep Inelastic Scattering at HERA*, paper 785 of the 29th Intern. Conf. on High-Energy Physics, Vancouver, Canada (1998)
- [98] D. de Florian and R. Sassot, *Fracture Functions for Diffractive and Leading Proton Deep Inelastic Scattering*, paper 986 of the 29th Intern. Conf. on High-Energy Physics, Vancouver, Canada (1998)
- [99] H. Abramowicz, J. Bartels, L. Frankfurt and H. Jung, *Diffractive Hard Scattering*, Proc. of the Workshop 'Future physics at HERA', eds. G. Ingelman, A. DeRoeck and R. Klanner, Vol.2, 635 (1996)
- [100] H. Jung, *Monte Carlo Implementations of Diffraction at HERA*, DESY-98-131, hep-ph - 9809374 (1998)
- [101] CDF Collab., *Diffractive Physics at CDF*, paper 928 of the 29th Intern. Conf. on High-Energy Physics, Vancouver, Canada (1998)
- [102] D0 Collab., *Hard Diffraction in $\bar{p}p$ Collisions at center-of-mass energies of 630 and 1800 GeV*, paper 469 of the 29th Intern. Conf. on High-Energy Physics, Vancouver, Canada (1998)
- [103] D0 Collab., *Probing Hard Color Singlet Exchange in $\bar{p}p$ Collision and 1800 GeV*, paper 467 of the 29th Intern. Conf. on High-Energy Physics, Vancouver, Canada (1998)
- [104] HERWIG 5.9 implementation of A.H. Mueller and W.K. Tang *Phys. Lett.* **B 284** (123) 1992,
V. Del Duca and W.K. Tang *Phys. Lett.* **B 312** (225) 1993
- [105] O.J.P. Eboli, E.M. Gregres and F. Halzen, MAD/PH-96-965 (1997)
- [106] CDF Collab., *Phys. Rev. Lett.* **78** (14) 1997
- [107] L. Alvero, J.C. Collins, J. Terron and J.J. Whitmore, *Diffractive Production of Jets and Weak Bosons, and Tests of Hard Scattering Factorization*, CTEQ-701-REV (1998), hep-ph - 9805268

- [108] E. Gotsman, E. Levin and U. Maor, *Energy Dependence of the Survival Probability of Large Rapidity Gaps*, hep-ph - 9804404 (1998)
- [109] K. Goulianos, *Pomeron Flux Renormalization: a Scaling Law in Diffraction*, hep-ph - 9806363 (1998)
- [110] S. Erhan and P.E. Schlein, *Phys. Lett.* **B 427** (389) 1998
- [111] P. Bruni and G. Ingelman, *Diffraction Hard Scattering at ep and $\bar{p}p$ Colliders*, DESY-93-187 (1993), Proc. of the Europhysics Conference on High Energy Physics, Marseille, France, 595 (1993)
- [112] J.A. Crittenden, *Exclusive Production of Neutral Vector Mesons at the ep Collider HERA* Springer Tracts in Modern Physics, Heidelberg, Vol. 140 (1997)
- [113] ZEUS Collab., J.Breitweg et al., *Measurement of Elastic Υ Photoproduction at HERA*, DESY 98-089 (1998), acc. by *Phys. Lett. B*
- [114] H1 Collab., *Photoproduction of Υ Mesons at HERA*, paper 574 of the 29th Intern. Conf. on High-Energy Physics, Vancouver, Canada (1998)
- [115] ZEUS Collab., *Exclusive Electroproduction of ρ and J/ψ Mesons at HERA*, paper 792 of the 29th Intern. Conf. on High-Energy Physics, Vancouver, Canada (1998)
- [116] ZEUS Collab., *Exclusive Electroproduction of φ Mesons at HERA* paper 793 of the 29th Intern. Conf. on High-Energy Physics, Vancouver, Canada (1998)
- [117] H1 Collab., *Diffraction Charmonium Production in Deep Inelastic Scattering at HERA* paper 572 of the 29th Intern. Conf. on High-Energy Physics, Vancouver, Canada (1998)
- [118] A.D. Martin, M.G. Ryskin and T. Teubner, *Phys. Rev.* **D 55** (4329) 1997
- [119] L. Frankfurt, W. Koepf and M. Strikman, *Phys. Rev.* **D 57** (512) 1998
- [120] H1 Collab., *Precision Measurement of the Inclusive Deep Inelastic ep Scattering Cross Section at Low Q^2 at HERA*, paper 534 of the 29th Intern. Conf. on High-Energy Physics, Vancouver, Canada (1998)
- [121] M. Erdmann and A. Meyer, *Rapidity Change of p and J/ψ in Nuclear Environment*, paper 1072 of the 29th Intern. Conf. on High-Energy Physics, Vancouver, Canada (1998)
- [122] D.S. Barton et al., *Phys. Rev.* **D 27** (2580) 1983
- [123] EMC Collaboration, J.J. Aubert et al., *Nucl. Phys.* **B 213** (1) 1983
- [124] H1 Collaboration, S. Aid et al., *Nucl. Phys.* **B 472** (3) 1996
- [125] ZEUS Collaboration, J. Breitweg et al., *Z. Phys.* **C 76** (599) 1997
- [126] L.L. Frankfurt, G.A. Miller and M. Strikman, *Ann. Rev. Nucl. Part. Sci.* **45**, 501 (1994)